UC Berkeley
UC Berkeley Electronic Theses and Dissertations

Title
Frequency Tunable MEMS-Based Timing Oscillators and Narrowband Filters

Permalink
https://escholarship.org/uc/item/3mq7068h

Author
Barrow, Henry Galahad

Publication Date
2015

Peer reviewed|Thesis/dissertation

eScholarship.org Powered by the California Digital Library
University of California

Frequency Tunable MEMS-Based Timing Oscillators and Narrowband Filters

By

Henry Galahad Barrow

A dissertation submitted in partial satisfaction of the

requirements for the degree of

Doctor of Philosophy

in

Engineering - Electrical Engineering and Computer Sciences

in the

Graduate Division

of the

University of California, Berkeley

Committee in charge:

Professor Clark T.-C. Nguyen, Chair
Professor Kristofer Pister
Professor Liwei Lin

Fall 2015

© Copyright 2015
Henry Galahad Barrow
All rights reserved

Abstract

Frequency Tunable MEMS-Based Timing Oscillators and Narrowband Filters

By

Henry Galahad Barrow

Doctor of Philosophy in Electrical Engineering and Computer Sciences

University of California, Berkeley

Professor Clark T.-C. Nguyen, Chair

There is little question that the commercial success of smartphones has substantially increased the volume of products utilizing Micro Electro Mechanical Systems (MEMS) technology, especially accelerometers, gyroscopes, bandpass filters, and microphones. The Internet of Things (IoT), a more recent driver for small, low power microsystems, seems poised to provide an even bigger market for these and other potential products based on MEMS. Given that the IoT will likely depend heavily on massive sensor networks using nodes for which battery replacement might not be practical, cost and power consumption become even more important. As already known for existing sensor networks, sleep/wake cycles will likely be instrumental to maintaining low sensor node power consumption in the IoT, and if so, then the clocks that must continuously run to synchronize sleep/wake events often become the bottlenecks to ultimate power consumption. On the communications side, narrowband RF channel-selecting front-end filters stand to greatly reduce receive power consumption by relaxing transistor circuit dynamic ranges.

Both the accuracy of the clocks and ability of filters to achieve bandwidths small enough to select individual channels depend heavily on the accuracy and precision to which the frequency-setting devices they rely on are constructed. Inevitably, fabrication tolerances are finite, which means the ability to attain the highest performance relies on trimming or tuning. This dissertation focuses on methods by which voltage-controlled frequency tuning of capacitively-transduced micromechanical resonators make possible 1) an ultra-compact, low-power 32.768-kHz micromechanical clock oscillator; and 2) a high-order, small percent bandwidth coupled-resonator filter with minimal passband distortion.

Currently, quartz crystal-based oscillators at 32.768 kHz dominate the market because they offer the best combination of cost and performance. However, the physical dimensions of these oscillators are presently too large for future small form-factor electronic applications, such as ones that fit within credit cards. While there have been attempts to shrink quartz resonating elements, the increasingly difficult fabrication steps required to produce such devices raises manufacturing costs, thereby preventing widespread adoption (so far). In addition, quartz crystal motional resistance values typically increase as resonator dimensions shrink, which in many oscillator configurations raises power consumption.

Unlike common quartz resonators, properly designed MEMS resonators benefit greatly from scaling in that reductions in lateral dimensions lead to a rapid decrease in motional resistance by a square law. The work described herein harnesses these scaling advantages to realize an oscillator much smaller than quartz-based oscillators with potential for much less power consumption. Specifically, this work uses aggressive lithography to achieve a capacitive-comb transduced micromechanical resonator occupying only 0.0154 mm^2 of die area. Wire bonding this resonator to a custom sustaining amplifier and a supply voltage of only 1.65V then realizes a 32.768-kHz real-time clock oscillator more than 100× smaller by area than miniaturized quartz crystal implementations and at least 4× smaller than other MEMS-based approaches. The use of voltage-controlled tuning Oscillations sustains with only 2.1 μW of power consumption.

On the filter front, whether realized using quartz, FBAR, or capacitive-gap transduced MEMS resonator, mechanical filter responses are only as flat as the accuracy of their constituent resonator center frequencies. While narrowband micromechanical filters comprised of up to three mechanically coupled resonators have been demonstrated in the past, there exists a demand for bandpass filters with even sharper roll-offs and larger stopband rejections, and this requires higher order filters utilizing more than three coupled resonators.

The work herein demonstrates filters comprised of four coupled resonators with bandwidths narrow enough to select individual channels. Before correction, filter passbands fresh out of the fab look nothing like their intended responses. Application of the automated passband correction protocol of this work, based on voltage-controlled frequency tuning, permits measurement of a 4-resonator micromechanical filter with a 0.1% bandwidth commensurate with the needs of channel-selection (albeit at a low frequency) and an impressive 20-dB shape factor of 1.59, all with less than 3dB of additional passband ripple (beyond the design ripple).

To my parents

ACKNOWLEDGEMENTS

First, I owe a debt of gratitude to my research advisor, Professor Clark T.-C. Nguyen, for his extensive technical guidance and generous financial support. His unparalleled knowledge in the field of Micro Electro Mechanical Systems, passion for academic research, and disciplined attention to detail will always be remembered.

I would also like to thank professors Kris Pister, Liwei Lin, and Ali Javey for their interest in my research and for taking the time to serve as my qualifying exam committee. Their guidance and critiques helped shape and improve my dissertation. In addition, the financial support provided by the DARPA CSSA program is gratefully acknowledged.

I thank the BSAC co-directors, John Huggins, Richard Lossing, Kim Ly, and the rest of the BSAC staff for providing invaluable exposure to industrial members and for upholding an environment of excellence. The weekly seminars helped broaden my knowledge base, and the semi-annual IAB meetings served as great sources for networking and professional development.

The privilege of working in the Marvell Nanofabribraction Laboratory has been an exceptional learning experience. I thank the talented staff, especially Bill Flounders, Bob Hamilton, Kim Chan, and Marilyn Kushner, for taking on the difficult task of maintaining such complicated equipment while simultaneously providing personalized assistance and advice.

I feel very fortunate to have been surrounded by the exceptional researchers comprising the Nguyen group. I will forever be grateful for the outstanding mentorship provided by our group's post-doctoral researchers Bongsang Kim, Tommi Riekkinen, and Tristan Rocheleau. Their commitment and guidance never wavered. Current and past graduate students, Bobby Schneider, Li-Wen Hung, Mehmet Akgul, Yang Lin, WeiChang Li, Thura Lin Nang, Brian Pepin, Lingqi Wu, Turker Beyazoglu, Ilya Gurin, Jalal Naghsh Nilchi, Ruonan Liu, Alper Ozgurluk, and Divya Kashyap, have provided diverse technical expertise, insightful conversation, and lasting friendship. I also appreciate the fabrication training and assistance provided by Zeying Ren and Victor Yeh.

My formative years at the University of Arizona opened my eyes to the exciting field of electrical engineering. I owe a special thanks to professors William Ryan, Robin Strickland, Hal Tharp, Hao Xin, and Ivan Djordjevic for instilling a passion for learning and for inspiring me continue on to graduate school.

Outside of the Nguyen group, I am grateful for the technical and casual interactions I have had from the world-class researchers throughout the EECS department. I thank Steven Callender, Mike Lorek, Michael Eggleston, Will Biederman, Dan Yeager, Katerina Papadopoulou, Fabien, Chraim, Milos Jorgovanovic, Nils Kwak, Richie Pryzbyla, Mathew Spencer, Albert Puggelli, Peng Zheng, Robin Zhang, and countless others for expanding my mind and for keeping me grounded.

Finally, I thank my wonderful friends and family. To my friends, thank you for helping to keep me balanced and for standing by my side through all the ups and downs of graduate student life. To my parents, thank you bringing me up in such a loving and supportive environment and for providing me with opportunities to explore my passions. This dissertation would not be possible without you!

CONTENTS

1. INTRODUCTION 1
1.1 MICROMECHANICAL CLOCK OSCILLATORS 3
1.1.1 Frequency Control 4
1.2 MICROMECHANICAL FILTERS 5
1.2.1 Tuning Considerations 7
1.3 OVERVIEW 7
2. THE CAPACITIVE-COMB TRANSDUCED FOLDED-BEAM RESONATOR 8
2.1 MICROMECHANICAL RESONATORS 8
2.2 CAPACITIVE TRANSDUCTION 11
2.2.1 Fixed Overlap Area Capacitive Transduction 13
2.2.2 Capacitive-Comb Transduction 16
2.3 FREQUENCY TUNABLE MICROMECHANICAL RESONATOR DESIGN TOPOLOGY 17
2.3.1 Lumped Mechanical Parameters 18
2.3.2 Equivalent Two-Port Circuit Neglecting Voltage-Tuning 19
2.3.3 Equivalent Two-Port Circuit with Voltage-Tuning 21
2.4 TYPICAL RESONATOR DESIGN VALUES 22
2.5 RESONATOR FABRICATION 23
3. A MEMS-BASED REAL-TIME CLOCK 27
3.1 RESONATOR DESIGN 27
3.1.1 Benefits of Scaling 28
3.1.2 Voltage-Controlled Frequency Tuning 31
3.1.3 Resonator Design Constraints and Considerations 32
3.1.4 Resonator Design Parameters and Layout 33
3.1.5 Resonator FEM Simulation 35
3.2 CMOS SUSTAINING AMPLIFIER 37
3.2.1 Low Power Design 39
3.3 EXPERIMENTAL RESULTS 49
3.4 CONCLUSIONS 54
4. HIGH-ORDER MICROMECHANICAL FILTERS 55
4.1 FILTER PERFORMANCE METRICS 56
4.2 COUPLED RESONATOR FILTER OPERATION 57
4.2.1 Simplified Design Procedure 58
4.2.2 Ratioed Folded-Beams 60
4.2.3 Resonator Asymmetry 61
4.2.4 Fourth Order Filter Layout 62
4.3 FILTER PASSBAND CORRECTION 63
4.3.1 Tuning Protocol 64
4.3.2 Rationale Behind the Protocol 65
4.3.3 Simulated Passband Correction 68
4.4 EXPERIMENTAL CONFIRMATION 69
4.5 CONCLUSIONS 73
5. CONCLUSION 74
5.1 MEMS-BASED REAL-TIME CLOCK OSCILLATOR 74
5.2 HIGH ORDER MICROMECHANICAL FILTERS 75
5.3 FUTURE RESEARCH DIRECTIONS 75

5.4 CONCLUDING REMARKS 76
REFERENCES 77

List of Tables

Table 1.1: MEMS sensors found in the iPhone 6s [4] 1
Table 2.1: Resonator Amplitude, Frequency, and Q of the Mechanical Resonator Modelled in the Mechanical and Electrical Domains [25] 10
Table 2.2: Equivalent Lumped Circuit Elements and their Corresponding Lumped Mechanical Parameters 19
Table 2.3: Typical Capacitive-Comb Transduced Resonator Design Values 23
Table 3.1: Capacitive-Comb Transduced Resonator Design Values 35
Table 3.2: 32 kHz Capacitive-Comb Transduced Resonator Design Values 40
Table 3.3: Sustaining Amplifier Design Parameters 40
Table 3.4: Oscillator Bias and Results Summary 53
Table 3.5: Oscillator Comparison 53

LIST OF FIGURES

FIGURE 1.1: PHOTOGRAPHIC OVERVIEW OF VARIOUS CAPACITIVE AND PIEZOELECTRIC MEMS RESONATORS [11][13][14][15][16][17] 3
FIGURE 1.2: SIZE, COST, AND MOTIONAL IMPEDANCE COMPARISON OF THREE COMMERCIALLY AVAILABLE 32.768-KHZ QUARTZ CRYSTALS [18][19][20] 4
FIGURE 1.3: SIMPLIFIED BLOCK LEVEL DIAGRAM WITH EMPHASIS PAID TO THE EFFECTS ASSOCIATED WITH MODIFICATION OF THE BANDPASS FILTER'S BANDWIDTH 6
FIGURE 2.1: THE MECHANICAL MASS-SPRING-DAMPER SYSTEM USED TO MODEL A UNIDIRECTIONAL RESONATOR 9
FIGURE 2.2: AN ELECTRICAL DOMAIN REPRESENTATION OF THE MASS-SPRING-DAMPER OF FIGURE 2.1 9
FIGURE 2.3: PERSPECTIVE-VIEW SCHEMATIC OF A PARALLEL-PLATE CAPACITIVE TRANSDUCER 11
FIGURE 2.4: PERSPECTIVE-VIEW SCHEMATIC HIGHLIGHTING THE FIXED OVERLAP AREA CAPACITIVE TRANSDUCTION CONFIGURATION. 13
FIGURE 2.5 PERSPECTIVE-VIEW SCHEMATIC DESCRIBING THE MECHANISM BEHIND ELECTRICAL STIFFNESS GENERATED BY THE PARALLEL PLATE TUNING ELECTRODES 15
FIGURE 2.6: PERSPECTIVE-VIEW SCHEMATIC OF THE CAPACITIVE-COMB TRANSDUCTION CONFIGURATION 16
FIGURE 2.7: PERSPECTIVE-VIEW SCHEMATIC OF A FREQUENCY TUNABLE CAPACITIVE-COMB TRANSDUCED FOLDED-BEAM MICROMECHANICAL RESONATOR 18
FIGURE 2.8: EQUIVALENT TWO-PORT TRANSFORMER MODEL FOR THE RESONATOR TOPOLOGY OF FIGURE 2.7, NEGLECTING VOLTAGE-TUNING EFFECTS 20
FIGURE 2.9: SIMPLIFIED LCR MODEL FOR THE RESONATOR TOPOLOGY OF FIGURE 2.7, NEGLECTING VOLTAGE-TUNING EFFECTS 21
FIGURE 2.10: TRANSFORMER AND SIMPLIFIED LCR SCHEMATIC REPRESENTATION OF THE VOLTAGE-TUNABLE CAPACITIVE-COMB DRIVEN RESONATOR OF FIGURE 2.7 22
FIGURE 2.11: CROSS-SECTIONS SUCCINCTLY ILLUSTRATING THE FABRICATION PROCESS FLOW USED TO ACHIEVE CAPACITIVE-COMB DRIVEN DEVICES. 24
FIGURE 2.12: SEM OF A FABRICATED 32-KHZ CAPACITIVE-COMB DRIVEN FOLDED-BEAM FREQUENCY TUNABLE MEMS-BASED RESONATOR. 25
FIGURE 2.13: SEM OF A FABRICATED 523-KHZ COUPLED RESONATOR FILTER. 26
FIGURE 3.1: PERSPECTIVE-VIEW SCHEMATIC OF THE TUNABLE CAPACITIVE-COMB DRIVEN FOLDED-BEAM RESONATOR CONNECTED IN A SERIES-RESONANT OSCILLATOR CIRCUIT 28
FIGURE 3.2: PLOT ILLUSTRATING THE SIMULATED BENEFITS OF BOTH MOTIONAL RESISTANCE R_X AND DIE AREA WHEN SCALING DOWN CRITICAL DIMENSIONS W AND G_0 AS LITHOGRAPHIC RESOLUTION IMPROVES 30
FIGURE 3.3: MEASURED PLOT OF RESONANCE FREQUENCY VERSUS TUNING VOLTAGE FOR THE DEVICE OF FIGURE 3.16 32
FIGURE 3.4: LITHOGRAPHIC MASK LAYOUT FOR THE CAPACITIVE-COMB TRANSDUCED RESONATOR OF THIS SECTION 34
FIGURE 3.5: LAYOUT AND PROCESS SPECIFIC COVENTORWARE FEM MODAL ANALYSES FOR THE RESONATOR DESIGN OF FIGURE 3.4 36
FIGURE 3.6: TOP-LEVEL CIRCUIT SCHEMATIC OF THE SERIES RESONANT OSCILLATOR ARCHITECTURE 37
FIGURE 3.7: TRANSISTOR LEVEL SCHEMATIC OF THE CUSTOM-DESIGNED TRANSRESISTANCE

SUSTAINING AMPLIFIER PRESENTED ALONGSIDE THE OP-LEVEL CIRCUIT SCHEMATIC OF THE MICROMECHANICAL RESONATOR CLOCK OSCILLATOR OF THIS CHAPTER. 38
FIGURE 3.8: SIMULATED FREQUENCY RESPONSE OF THE SUSTAINING AMPLIFIER OF FIGURE 3.7 WITH R_F HELD TO 5MΩ AND BOND PAD CAPACITANCES OF 0.75 PF..................................42
FIGURE 3.9: BANDWIDTH PLOTTED AGAINST R_F FOR THE SUSTAINING AMPLIFIER OF FIGURE 3.7 WITH BOND PAD CAPACITANCES OF 0.75PF 43
FIGURE 3.10: SIMULATED GAIN AND PHASE SHIFT AT AN OPERATING FREQUENCY OF 32 KHZ PLOTTED AGAINST R_F FOR THE SUSTAINING AMPLIFIER OF FIGURE 3.7 WITH BOND PAD CAPACITANCES OF 0.75PF 44
FIGURE 3.11: CLOSED LOOP FREQUENCY RESPONSE FOR VARIOUS AMPLIFIER DRAIN CURRENTS ASSUMING THE RESONATOR AND SUSTAINING AMPLIFIER CONDITIONS OUTLINED IN TABLE 3.2 AND TABLE 3.3 RESPECTIVELY...46
FIGURE 3.12: CLOSED LOOP FREQUENCY RESPONSE WITH THE MINIMUM DRAIN CURRENT REQUIRED FOR SUSTAINED OSCILLATION 47
FIGURE 3.13: MINIMUM SUSTAINING AMPLIFIER POWER CONSUMPTION PLOTTED AGAINST RESONATOR MOTIONAL RESISTANCE UNDER VARIOUS PARASITIC CAPACITANCE CONDITIONS 48
FIGURE 3.14: MINIMUM SUSTAINING AMPLIFIER POWER CONSUMPTION REQUIRED TO SUSTAIN OSCILLATION PLOTTED AGAINST COMB FINGER GAP SPACING FOR VARIOUS PARASITIC CAPACITANCE CONDITIONS 49
FIGURE 3.15: MEASURED FREQUENCY CHARACTERISTIC FOR THE FIGURE 2.12 DEVICE UNDER 10 MTORR VACUUM. 50
FIGURE 3.16: PHOTO OF THE CUSTOM VACUUM BOX TEST APPARATUS, WITH A BLOW UP OF A MOCK OSCILLATOR SCHEMATIC COMBINING THE SEM OF THE MICROMECHANICAL RESONATOR WITH A DIE PHOTO OF THE CUSTOM-DESIGNED ASIC AMPLIFIER..................51
FIGURE 3.17: MEASURED OSCILLATOR OUTPUT SPECTRUM AND TIME-DOMAIN WAVEFORM.....52
FIGURE 3.18: SIZE COMPARISON OF THE RESONATING ELEMENT OF THIS WORK AGAINST PREVIOUSLY DEMONSTRATED MINIATURE CLOCK RESONATORS [18][19][20][13]............54
FIGURE 4.1: TOP-VIEW SCHEMATIC OF THE 8-POLE MICROMECHANICAL FILTER IN A SINGLE-ENDED DRIVE AND SENSE CONFIGURATION AND EQUIPPED WITH FREQUENCY TUNING ELECTRODES TO ALLOW FOR PASSBAND CORRECTION USING AN AUTOMATED TUNING PROTOCOL...55
FIGURE 4.2: SAMPLE BANDPASS FILTER SPECTRUM WITH IMPORTANT PERFORMANCE METRICS HIGHLIGHTED. 56
FIGURE 4.3: FILTER SPECTRUM ILLUSTRATION HIGHLIGHTING THE IMPROVEMENT IN SHAPE FACTOR AS THE NUMBER OF COUPLED RESONATOR FILTERS IS INCREASED. 57
FIGURE 4.4: PERSPECTIVE-VIEW ILLUSTRATION SHOWING DETAILS OF THE CAPACITIVE COMB-DRIVEN FOLDED-BEAM RESONATOR USED IN THE MULTI-RESONATOR FILTER. 58
FIGURE 4.5: PERSPECTIVE-VIEW AND EQUIVALENT CIRCUIT OF A SECTION OF THREE COUPLED RESONATORS IN A MICROMECHANICAL FILTER CONFIGURATION. 58
FIGURE 4.6: SIMULATED TERMINATED AND UNTERMINATED FOUR-RESONATOR FILTER PASSBAND ALONGSIDE THE SYSTEM'S VIBRATIONAL MODE SHAPES. 59
FIGURE 4.7: PERSPECTIVE-VIEW OF A SINGLE RESONATOR HIGHLIGHTING ITS RATIOED FOLDED-BEAMS..61
FIGURE 4.8: MASK LAYOUT OF A SINGLE COUPLED RESONATOR. THE LOWER TRUSS IS DESIGNED TO MORE MASS TO COMPENSATE FOR THE NECESSARY ASYMMETRIC RATIOED FOLDED BEAMS..62
FIGURE 4.9: MASK LAYOUT OF A MICROMECHANICAL FILTER COMPRISED OF FOUR COUPLED

RESONATORS 63
FIGURE 4.10: SIMULATIONS ILLUSTRATING THE EFFECTS OF MISMATCHING OF A SINGLE RESONATOR IN A 4-RESONATOR FILTER WITH PERCENT-BANDWIDTHS OF (A) 3% AND (B) 0.1%. HERE, THE PASSBAND DISTORTING EFFECT OF FREQUENCY MISMATCH IS MUCH LARGER FOR SMALLER PERCENT-BANDWIDTH. 64
FIGURE 4.11: BLOCK DIAGRAM OF THE PROPOSED TUNING PROTOCOL 65
FIGURE 4.12: EQUIVALENT LUMPED ELEMENT MODEL FOR AN *N*-TH ORDER COUPLED RESONATOR FILTER INDICATING THE MESHES THAT MUST RESONATE AT THE GEOMETRIC CENTER FREQUENCY. 66
FIGURE 4.13: SIMULATED EFFECTS OF PASSBAND DISTORTION DUE TO FREQUENCY VARIATION OF A SINGLE COUPLED RESONATOR 67
FIGURE 4.14: SIMULATED 4-RESONATOR FILTER OUTPUT ENERGY PLOTTED AGAINST THE FREQUENCY OFFSET OF A SINGLE ONE OF ITS CONSTITUENT RESONATORS, ASSUMING ALL OTHER RESONATORS ARE SPOT ON. 68
FIGURE 4.15: SIMULATION DEMONSTRATING THE METHOD AND EFFICACY OF THE ENERGY MAXIMIZING TUNING PROTOCOL. 69
FIGURE 4.16: SEM IMAGES OF A MICROMECHANICAL FILTER COMPRISED OF 4 COUPLED RESONATORS ALONGSIDE AN ENLARGED VIEW OF ONE OF ITS CONSTITUENT CAPACITIVE COMB-TRANSDUCED RESONATORS. 70
FIGURE 4.17: CUSTOM-MADE GLASS VACUUM CHAMBER USED TO TEST THE FILTER TUNING PROTOCOL OF THIS WORK 71
FIGURE 4.18: MEASURED 4-RESONATOR FILTER CHARACTERISTIC WITH (A) NO TUNING APPLIED, I.E., STRAIGHT OUT OF THE FAB, (B) TUNING VOLTAGES GOVERNED BY ONE PROCEDURAL ITERATION (THROUGH ONE OF THE CONSTITUENT RESONATORS), AND (C) THE FINAL TUNED RESPONSE AFTER TWO ITERATIONS. 72
FIGURE 4.19: MEASURED TRANSCONDUCTANCE SPECTRA FOR A SINGLE CAPACITIVE COMB-TRANSDUCED RESONATOR 73

1. INTRODUCTION

For more than three decades, Micro Electro Mechanical Systems (MEMS) have steadily transitioned out of research labs and into production forming a more than $10 billion market [1]. MEMS devices such as accelerometers, pressure sensors and microphones, to name a few, have seen immense utilization, particularly in the consumer electronics market, because of their compact sizes and minute power consumptions. In addition, these devices benefit from batch fabrication, which has enabled year-over-year reductions in cost [2]. In recent years, Apple's iPhone and similar smartphones have been the driving force behind the success of MEMS companies, spurring continued revenue growth as more and more MEMS sensors are incorporated into each successive product generation [3]. As summarized in Table 1.1, Apple's 2015 model, the iPhone 6s, incorporates seven discrete MEMS sensors [4], exactly seven more MEMS sensors than the most popular cellular phone of 2005, the Nokia 1100 [5].

Table 1.1: MEMS sensors found in the iPhone 6s [4]

Name	Device Type	Quantity
Knowles KSM2	Microphone	3
Bosch Sensortec BMA280	3-axis Accelerometer	1
Bosch Sensortec BMP280	Barometric Pressure Sensor	1
Goertek GWM1	Microphone	1
InvenSense MP67B	6-axis Gyroscope and Accelerometer Combo	1

While the arrival of the smartphone has ushered in an unprecedented increase in MEMS utilization, perhaps this wave of commercial success is merely the beginning of a much greater undertaking. The Internet of Things (IoT), a more recent driver for small, low power microsystems, seems poised to provide an even bigger market for MEMS sensors and other potential products based on MEMS [6]. Given that the IoT will likely depend heavily on massive sensor networks using nodes for which battery replacement might not be practical, cost and power consumption become even more important [7]. As already known for existing sensor networks, sleep/wake cycles will likely be instrumental to maintaining low sensor node power consumption in the IoT, and if so, then the clocks that must continuously run to synchronize sleep/wake events often become the bottlenecks to ultimate power consumption. On the communications side, narrowband RF channel-selecting front-end filters stand to

greatly reduce receive power consumption by relaxing transistor circuit dynamic ranges.

In this dissertation, two distinct MEMS-based system components will be considered that have the potential for reducing the overall footprint and power consumption of IoT sensor nodes in the future. First, a low power real-time clock oscillator will be discussed that utilizes a frequency-tunable, capacitively transduced polysilicon resonator rather than a traditional quartz crystal. As will be shown, one of main advantages of employing a MEMS-based resonator for this application is that unlike quartz crystals, reductions in lateral resonator dimensions via lithographic scaling enables considerable reductions in oscillator power consumption. Next, focus will be shifted toward mechanically coupling MEMS resonators of the same topology to realize high-order, narrowband filters. The small percent-bandwidths afforded by these MEMS-based filters have the potential to simplify radio receiver front-end circuits and enable drastic reductions in power consumption.

In order to achieve the goal of developing MEMS-based oscillators and filters for IoT applications, a suitable resonator topology must first be established. As emphasized in Figure 1.1, researchers have successfully demonstrated a myriad of vibrating MEMS resonator designs that exhibit high Qs over a broad range of resonance frequencies. In this dissertation, the search for a unified resonator topology is restricted to those leveraging capacitive transduction because of the relative fabrication ease, linearity, and scaling benefits associated with this transduction method [9][10]. In the case of the micromechanical clock oscillator, it is preferable to employ a resonator with a natural frequency equal to the desired reference frequency of 32.768 kHz to avoid the additional power draw associated with frequency division. Therefore, the resonator topology chosen for the micromechanical clock oscillator to be presented essentially mimics the folded-beam, capacitive comb-driven designs of [9] and [11] because these designs afford resonance frequencies in the kHz range while maintaining a small device area. Fortunately, the folded-beam, comb-driven resonator topology has also proven to be quite useful when implemented to realize high-order, medium frequency, narrowband micromechanical filters [12].

During the development of MEMS-based oscillators and filters, careful consideration should be payed to the mitigation of fabrication defects, especially as resonator dimensions are scaled and filter order is increased. To that end, the resonator topology must incorporate some form of frequency trimming, preferably voltage controlled, to correct for these imperfections. For the oscillator application, frequency trimming serves to alleviate center frequency variations exacerbated by aggressive scaling. With respect to the coupled resonator filter application, frequency trimming allows for the application of post-fabrication passband correction, and with a suitable tuning protocol, the number of coupled resonator can be increased. Chapter 2 will detail the frequency-tunable capacitive comb-transduced folded-beam resonator topology leveraged in this dissertation to realize both a tiny micromechanical clock oscillator and a high-order, narrowband coupled resonator filter.

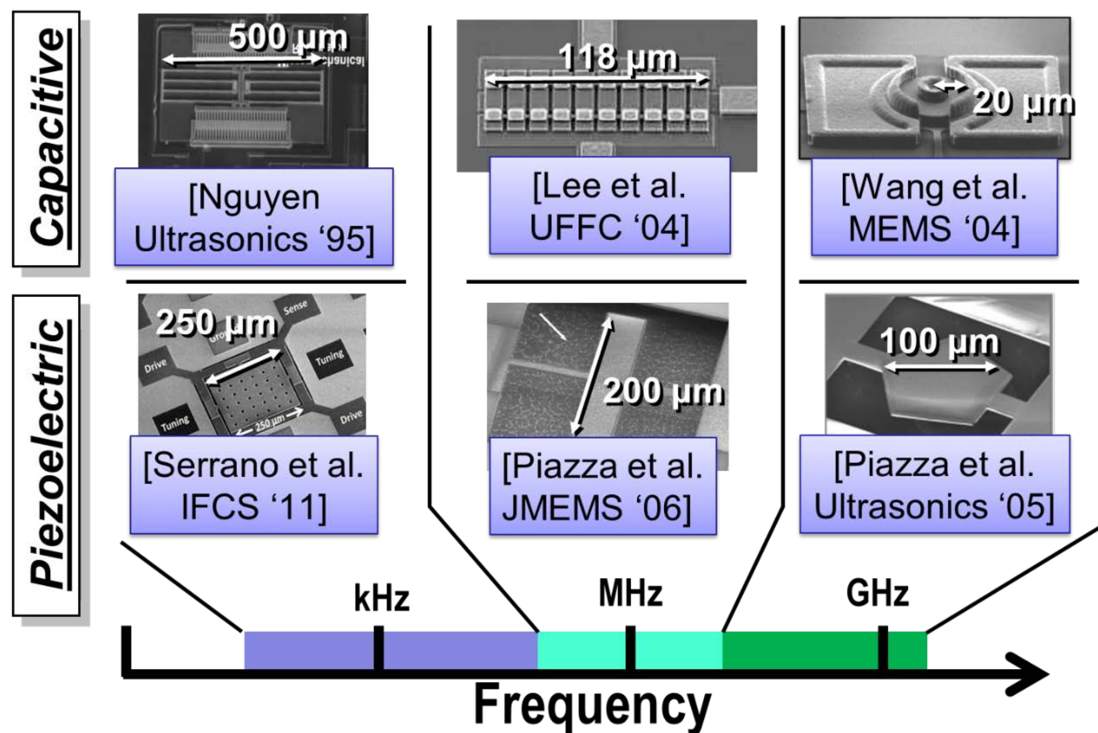

Figure 1.1: Photographic overview of various capacitive and piezoelectric MEMS resonators [11][13][14][15][16][17]

1.1 Micromechanical Clock Oscillators

32.768-kHz real-time clock oscillators encompass a significant share of the multi-billion dollar oscillator market. Currently, quartz crystal-based oscillators at this frequency dominate the market because they offer the best combination of cost and performance. However, the physical dimensions of these oscillators are presently too large for future small form-factor electronic applications, such as ones that fit within credit cards. As illustrated in Figure 1.2, attempts have been made to shrink quartz resonators at this frequency [18][19][20]. Unfortunately, the increasingly difficult fabrication steps required to produce such devices raises manufacturing costs, thereby preventing widespread adoption (so far). In addition, quartz crystal motional resistance values typically increase as resonator dimensions shrink, which in many oscillator configurations raises power consumption [21].

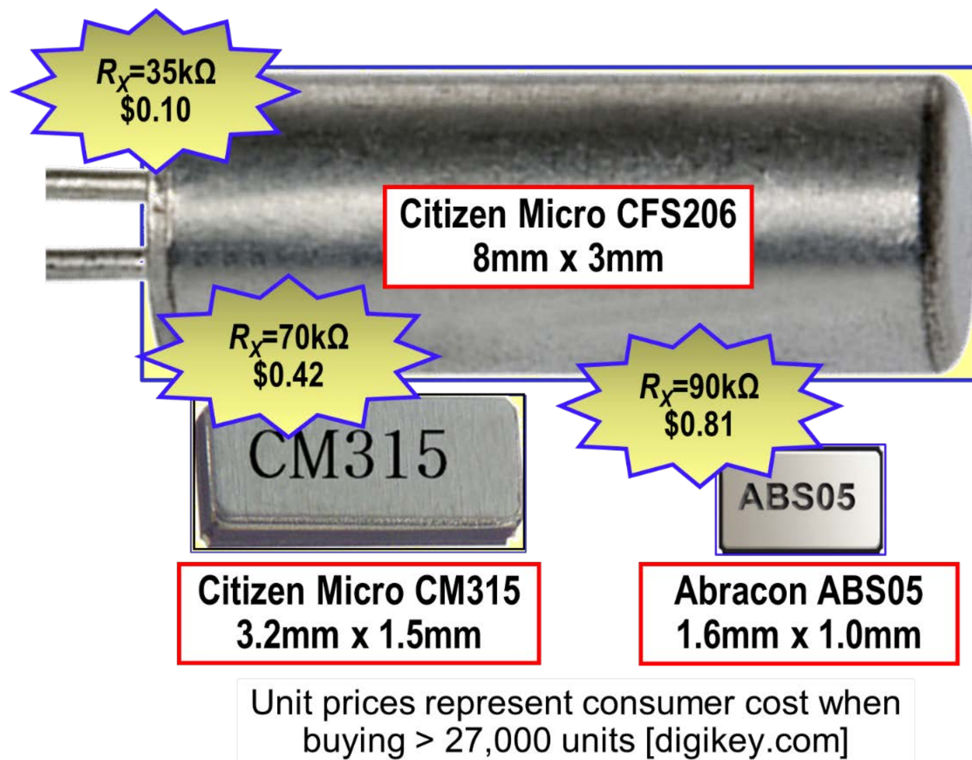

Figure 1.2: Size, cost, and motional impedance comparison of three commercially available 32.768-kHz quartz crystals [18][19][20]

Recent advancements in MEMS technology for frequency control now offer a vision whereby batch-fabricated MEMS-based oscillators might provide a suitable solution for systems requiring ultra-small components at low cost. Indeed, MEMS-based oscillator companies such as Micrel and SiTime have demonstrated commercial success with products that exhibit adequate drift stability and jitter performance acting as low cost drop-in crystal oscillator replacements [22][23]. While 32.768-kHz MEMS-based resonators have recently been released that are 10× smaller than quartz counterparts [23], the potential for even smaller devices remains.

Unfortunately, MEMS resonators are by no means immune to fabrication process imperfections, especially as feature sizes shrink to lithographic limits. Because the resonance frequency of a mechanical resonator is governed by device geometry, process variation will, in turn, result in device-to-device and wafer-to-wafer resonance frequency deviations that must be accounted for and corrected by means of post-fabrication frequency tuning.

1.1.1 Frequency Control

The purpose of a real-time clock oscillator is to provide an accurate measure of the passing of time. For example, in a wristwatch application, the clock oscillator dictates when the second hand is incremented. The output frequency of a real-time clock oscillator is often constrained to 32.768 kHz, exactly 2^{15} cycles per seconds, because at this frequency the

oscillator can be combined with an inexpensive, low-power, 16-bit counter to provide digital time-keeping information [24]. It therefore follows that in order for a real-time clock oscillator to be of any practical value it must possess a relatively high degree of frequency accuracy. For example, if the oscillator were to oscillate at a frequency of 32.769 kHz, just 1 Hz (30 ppm) higher than intended, the clock would be gain an additional minute each month.

In order to achieve acceptable frequency accuracy, quartz crystal manufacturers rely on techniques such as mechanical grinding, surface polishing, plasma etching, and metal depositions [25]. Unfortunately, because of the relatively small sizes of MEMS resonators compared to their quartz counterparts, these frequency-trimming methods have proven impractical.

One method for correcting the resonance frequency of MEMS resonators that has seen success is laser ablation. Initially, this method was able to trim resonators to within 21 ppm [26], and with additional development in an industrial setting, laser trimming of packaged MEMS devices has proven capable of trimming resonance frequencies from an initial deviation of 4% to just 2.6 ppm [27]. Although this method has seen commercial viability [28], it demands expensive transparent packages. Moreover, the laser induced stresses may lead to unpredictable changes in resonator Q [29]. Rather than relying on a permanent mechanical post-fabrication trim, the resonator of Chapter 2 is designed with electrical stiffness-based voltage controlled resonance frequency tuning electrodes [30] capable of providing up to 50,000 ppm of frequency tuning over a 3.3 V applied tuning voltage range.

Chapter 3 presents the combination of the tunable capacitive-comb driven, folded-beam resonator of Chapter 2 with a custom designed application-specific integrated circuit (ASIC) to realize an ultra-compact MEMS-based 32.768-kHz clock oscillator. While the presented device exhibits excellent performance with respect to power consumption and die footprint, the extensive scaling potential of the underlying resonator topology should lead to continued performance improvements with future lithographic advancements.

1.2 Micromechanical Filters

As interest in ultra-low power radios for sensor networks increases, so does a similar interest in small percent bandwidth frequency filters capable of selecting individual RF channels while rejecting all other channels, even those traditionally considered in-band [8]. To illustrate the demand for a small percent bandwidth filter, Figure 1.3 presents a simplified receiver front end with careful attention paid to the bandpass filter that directly succeeds the antenna. Here the signal channel of interest is colored green and all unwanted signals are colored red. When the bandpass filter possess a relatively large bandwidth, labelled here as "band-select," the low-noise amplifier (LNA) following the filter is presented with a significant amount of unwanted signal power at frequencies outside the desired signal channel. On the other hand, when the bandpass filter possesses a smaller bandwidth, labelled in Figure 1.3 as "channel-select," the LNA is not significantly perturbed by unwanted interfering signals. Indeed, if such narrowband filters were feasible, radio receiver front-end circuits could dispense with the overdesign often needed to insure sufficient dynamic range against strong interfering signals that would otherwise desensitize them. The result would be a substantial

reduction in the power consumed by such circuits.

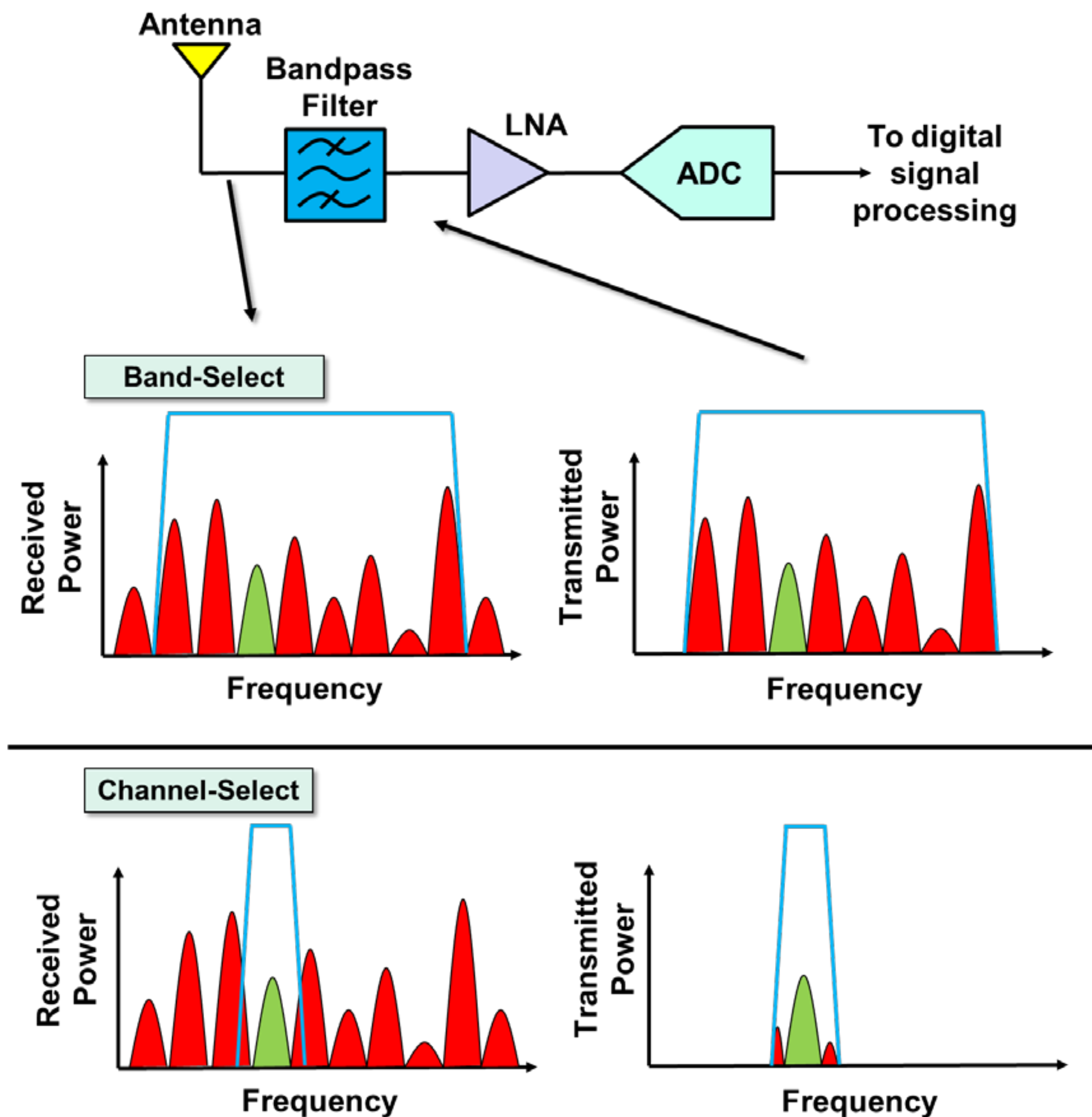

Figure 1.3: Simplified block level diagram with emphasis paid to the effects associated with modification of the bandpass filter's bandwidth

To date, no high volume (inexpensive) filter technology can yet achieve the described RF channel-selection with adequate performance, although some might be on the verge of this. In particular, filters employing high Q capacitive-gap transduced vibrating resonators, such as that of [31], have actually achieved adequately low insertion loss when passing the needed 0.1% bandwidth. However, they unfortunately require improvements in electromechanical coupling to attain the needed >50dB stopband rejection. They are also in need of some way to improve yield, which becomes ever more difficult when percent bandwidths are only 0.1%.

1.2.1 Tuning Considerations

A 0.1%-bandwidth 455-kHz 0.5dB-ripple 4-resonator Chebyshev filter employing quarter-wave couplers between (ideally) identical resonators requires that the resonators be matched to no worse than 137ppm to avoid additional passband ripple (over the design value) of more than 0.5dB [32]. Given that resonators from [33] fabricated using a university nanofabrication facility post device-to-device frequency standard deviations on the order of 315ppm, it seems unlikely that RF channel-selecting filters with adequately small passband ripple can be manufactured with sufficient yield for high volume production. Indeed, unless industrial microfabrication facilities can do substantially better than their university counterparts, some form of frequency tuning or trimming will be needed. Inevitably, it is likely not a question of whether or not trimming or tuning is needed, but rather what protocol can most efficiently correct the passband response.

Towards answering this question, the coupled resonator filter highlighted in Chapter 4 employs electrical stiffness-based voltage-control of capacitive-gap transduced resonator frequency [30] to explore an automated tuning protocol bent on maximizing the integrated energy in the filter response spectrum. The method lends itself well to iterative convergence, where the change in integrated energy induced by a small tune in one direction immediately confirms or rejects that direction, hence, governs the direction needed for the next tune increment. Use of this tuning protocol yields a 4-resonator micromechanical filter with a 0.1% bandwidth commensurate with the needs of channel-selection (albeit at a low frequency) and an impressive 20-dB shape factor of 1.59, all with less than 3 dB of additional passband ripple (beyond the design ripple).

1.3 Overview

This dissertation focuses on employing a unified frequency-tunable resonator topology to realize an ultra-compact, low-power micromechanical clock oscillator and a high-order, small percent bandwidth coupled-resonator filter. Chapter 2 presents an overview of the frequency-tunable capacitive-comb transduced folded-beam resonator. In this chapter, design equations and equivalent circuit models are established. Following this discussion, Chapter 3 presents a resonator designed and fabricated following the topology outlined in Chapter 2 in combination with a custom-designed ASIC to yield a 32.768-kHz clock oscillator. Here the resonator scaling benefits, and design considerations with respect to the resonating element and the sustaining amplifier are outlined in detail. Next, Chapter 4 discusses the mechanical coupling of several resonators of the Chapter 2 topology to realize a high-order micromechanical filter. In this chapter, special attention is payed to the effects of resonator-to-resonator frequency mismatch and a tuning protocol capable of providing autonomous filter passband correction. Finally, Chapter 5 concludes this dissertation.

2. THE CAPACITIVE-COMB TRANSDUCED FOLDED-BEAM RESONATOR

As emphasized in Chapter 1, this dissertation focusses on leveraging MEMS resonators to yield micromechanical clock oscillators and narrowband filters. This chapter serves to establish the resonator topology harnessed in both applications and present the relevant design equations, circuit models, and fabrication details.

2.1 Micromechanical Resonators

Frequency selective electronics such as oscillators and bandpass filters typically rely on mechanical resonators to generate precise frequencies. This is because unlike on-chip LC tanks with Q values rarely surpassing 50 [34][35], mechanical resonators have Q values in excess of 1,000 [36]–[38]. A micromechanical resonator is essentially a mechanical system that is driven into resonance at a specific frequency or set of frequencies. In its simplest form, a unidirectional mechanical resonator can be modelled as a mass-spring-damper system. As seen in Figure 2.1, the resonator has a mass m, a spring k, and a damper c. The resonator is driven into vibration by applying a sinusoidal force F with a frequency ω. In this simplistic model motion is restricted to a single axis, therefore the system possess one degree of freedom. With the application of Newton's second law the force can be expressed as a function of velocity

$$\boldsymbol{F = j\omega m\dot{x} + \frac{k}{j\omega}\dot{x} + c\dot{x}} \tag{2.1}$$

and the mass-spring-damper's resonance frequency ω_0 is expressed as

$$\boldsymbol{\omega_0 = \sqrt{\frac{k}{m}}} \tag{2.2}$$

While (2.1) and (2.2) serve as good starting points for designing micromechanical resonator geometries, owing to their small stature, these devices are overwhelmingly embedded in electrical systems and it is therefore particularly useful to model these mechanical devices

with analogous electrical components. In addition, when designing filters comprised of coupled resonators it is beneficial to work in the electrical domain to take advantage of well-established filter synthesis techniques [25][39].

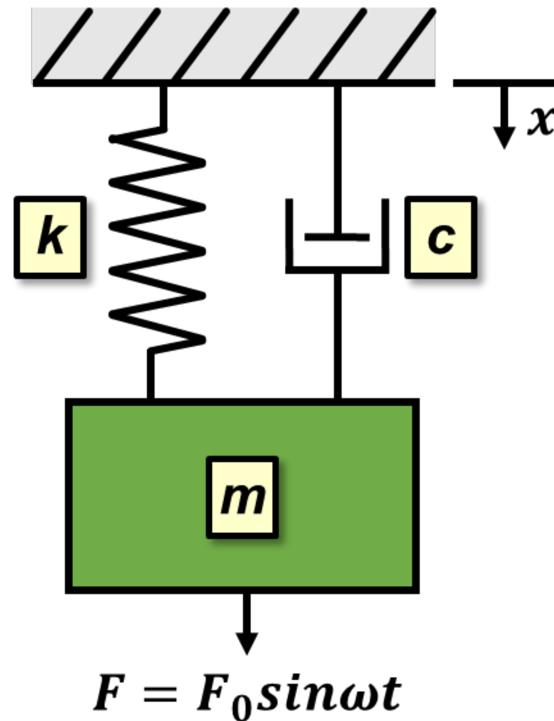

Figure 2.1: The mechanical mass-spring-damper system used to model a unidirectional resonator

In the electrical domain, the mass-spring damper of Figure 2.1 can be modelled, assuming an appropriate electromechanical transducer, as the series inductor-capacitor-resistor (LCR) network shown in Figure 2.2 [40].

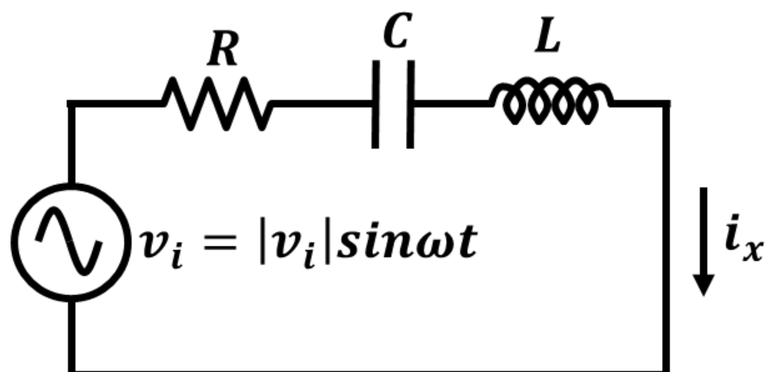

Figure 2.2: An electrical domain representation of the mass-spring-damper of Figure 2.1

To further bridge the mechanical and electrical domains, expressions for the

normalized amplitude, natural frequency, and Q are summarized in Table 2.1. These expressions coupled with the models of Figure 2.1 and Figure 2.2 provide essential resonator design and operational insights, however a method for driving the micromechanical resonators into motion must still be established.

Table 2.1: Resonator Amplitude, Frequency, and Q of the Mechanical Resonator Modelled in the Mechanical and Electrical Domains [25]

Domain	Normalized Amplitude	Frequency	Q
Mechanical	$\frac{Xk}{F_0} = \frac{1}{\sqrt{\left[1-\left(\frac{\omega}{\omega_0}\right)^2\right]^2 + \left(\frac{\omega}{Q\omega_0}\right)^2}}$	$\omega_0 = \sqrt{\frac{k}{m}}$	$Q = \frac{k}{c\omega_0}$
Electrical	$\frac{I_x}{V_i(\omega C_x)} = \frac{1}{\sqrt{\left[1-\left(\frac{\omega}{\omega_0}\right)^2\right]^2 + \left(\frac{\omega}{Q\omega_0}\right)^2}}$	$\omega_0 = \frac{1}{\sqrt{L_x C_x}}$	$Q = \frac{\omega_0 L_x}{R_x}$

2.2 Capacitive Transduction

Due to its relative fabrication ease and linearity, capacitive transduction remains one of the most widely utilized transduction methods for driving micromachined micromechanical resonators into motion. In particular, capacitive transduction is desirable because both the resonator and transducer can be patterned from the same material layer. This greatly simplifies the fabrication process, even allowing for the creation of fully functioning resonators defined by a single lithographic mask [9][41][42].

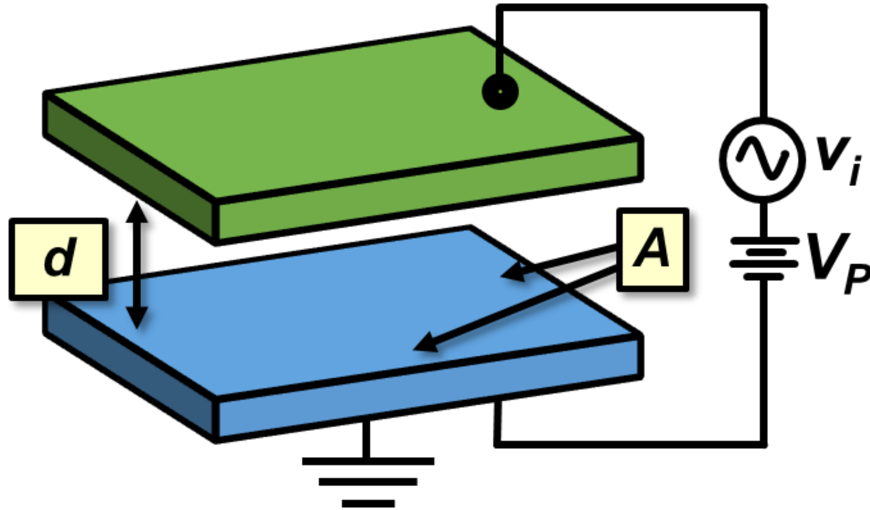

Figure 2.3: Perspective-view schematic of a parallel-plate capacitive transducer

Figure 2.3 presents the perspective-view schematic of a parallel-plate capacitive transducer with a dc-bias voltage V_P and an ac (sinusoidal) excitation signal v_i. Neglecting fringing fields, the capacitance C of a parallel plate can be expressed as

$$C_i = \frac{\varepsilon A}{d} \tag{2.3}$$

where ε is the dielectric permittivity; A is the plate overlap area and d is the plate separation. The electric potential energy U and the electrostatic force F of the capacitor can be written as

$$U_i = \frac{1}{2} C_i (V_p - v_i)^2 \tag{2.4}$$

and

$$F_i = \frac{\partial U_i}{\partial x} = \frac{1}{2} (V_p - v_i)^2 \frac{\partial C_i}{\partial x} \tag{2.5}$$

$$= \frac{1}{2}\left(V_p - |v_i|\cos(\omega t)\right)^2 \frac{\partial C_i}{\partial x}$$

$$= \frac{1}{2}\left(V_P^2 + \frac{|v_i|}{2} - 2V_P|v_i|\cos(\omega t) + \frac{|v_i|^2}{2}\cos(2\omega t)\right)\frac{\partial C_i}{\partial x}$$

The resultant driven force of (2.5) contains a dc component and ac components at the excitation frequency ω and at twice the excitation frequency 2ω. If the excitation signal v_i has a frequency matching the resonance frequency of the resonator, the force component at ω is amplified by the resonator's quality factor Q, while the force components at dc and 2ω remain unchanged and in the high-Q case, these off-resonance force components may be neglected for simplicity. It should be noted that if the dc-bias establishes a built in ON/OFF switch because when the bias voltage is shorted (V_P = 0 V), the on-resonance frequency component of the excitation force reduces to zero, impeding resonance vibration.

As shown in (2.5), the capacitive transducer can change an electrical excitation into a mechanical force. Conversely, the capacitive transducer can also convert a mechanical motion into an electrical current. To establish this relationship it is instructive to consider the charge p on a capacitor given by

$$p = C_i(V_p - v_i) \tag{2.6}$$

A current is produced when the charge varies with time

$$\begin{aligned} i_i = \frac{dp}{dt} &= \left(V_p - v_i\right)\frac{\partial C_i}{\partial t} - C_i\frac{\partial v_i}{\partial t} \\ &= \left(V_p - v_i\right)\frac{\partial x}{\partial t}\left(\frac{\partial C_i}{\partial x}\right) - C_i\frac{\partial v_i}{\partial t} \end{aligned} \tag{2.7}$$

The first term in (2.7) arises from the time time-varying capacitance due to motion and the second term is a result of electrical capacitance feedthrough. In the case where the capacitive transducer is used to sense motion (no ac voltage is applied), the current becomes

$$i_o = \left(V_p\right)\frac{\partial x}{\partial t}\left(\frac{\partial C_i}{\partial x}\right) \tag{2.8}$$

From (2.8) it becomes readily apparent that mechanical motion resulting in a capacitance change does indeed result in an electrical current.

As seen in (2.3), the parallel plate capacitance is a function of both overlap area A and plate separation d. Capacitive transducers are typically designed in a fashion such that one of these geometries (either A or d) is fixed while the other is modulated in the presence of mechanical motion. These distinct configurations result in unique transduction properties and

both configurations are employed in this dissertation. Therefore, it is beneficial to take a closer at both configurations.

2.2.1 Fixed Overlap Area Capacitive Transduction

In the fixed overlap area capacitive transduction configuration, illustrated in Figure 2.4, electrode plates move in a direction perpendicular to each other thereby modulating the capacitive plate separation d. Assuming operation in free space and neglecting fringing fields, the parallel-plate transducer capacitance as a function of displacement is written as

$$C_{FA}(x) = \frac{\varepsilon_0 A_{os}}{(d_0 + x)} = C_{os}\left(1 + \frac{x}{d_0}\right)^{-1} \approx C_{os}\left(1 - \frac{x}{d_0}\right) \tag{2.9}$$

where A_{os} is the fixed parallel plate overlap area, and C_{os} is parallel plate capacitance with a static plate displacement of d_0.

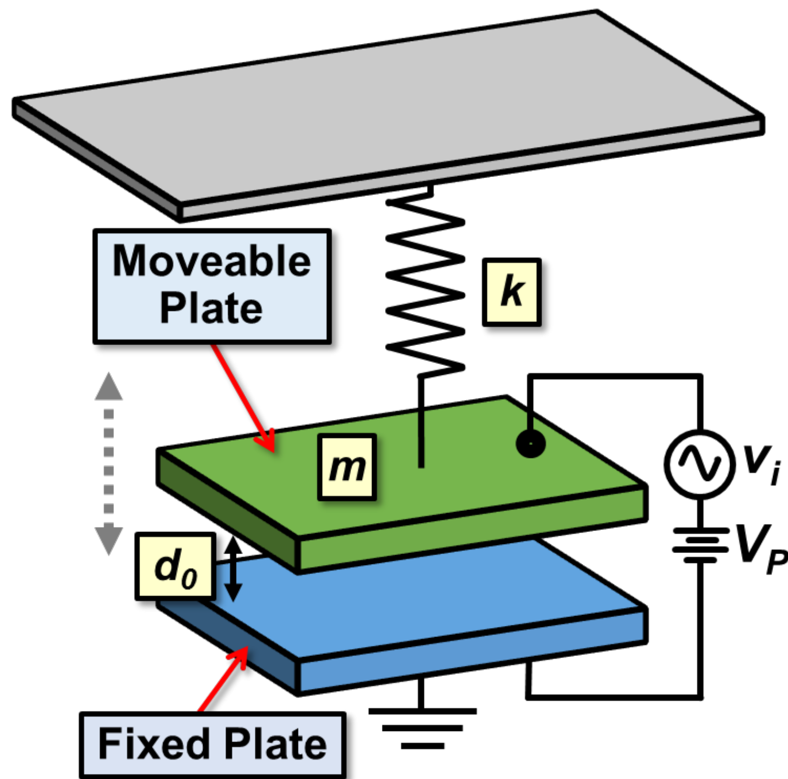

Figure 2.4: Perspective-view schematic highlighting the fixed overlap area capacitive transduction configuration.

Assuming the moveable plate displaces a small fraction of the static gap d_0, the fixed overlap area capacitance as a function of displacement $C_{FA}(x)$ becomes

$$C_{FA}(x) \approx C_{os}\left(1 - \frac{x}{d_0}\right) \tag{2.10}$$

Differentiating (2.9) and approximating for small displacements using a first order Taylor expansion yields

$$\frac{\partial C_{FA}}{\partial x} = -\frac{C_{os}}{d_0}\left(1 + \frac{x}{d_0}\right)^{-2} \approx -\frac{C_{os}}{d_0}\left(1 - \frac{2x}{d_0}\right) \tag{2.11}$$

Combining (2.5) and (2.11) yields the electrostatic force for the fixed overlap area parallel plate transducer F_{FA}

$$\begin{aligned} F_{FA} &= -\frac{1}{2}(V_{FA} - v_i)^2 \frac{C_{os}}{d_0}\left(1 + \frac{x}{d_0}\right)^{-2} \\ &\approx -\frac{1}{2}(V_{FA} - v_i)^2 \frac{C_{os}}{d_0}\left(1 - \frac{2x}{d_0}\right) \end{aligned} \tag{2.12}$$

Assuming $V_p \gg |v_i|$, the electrostatic force can be approximated as

$$\begin{aligned} F_{FA} &\approx \left(V_{FA}^2 - 2V_{FA}|v_i|cos(\omega t)\right)\frac{C_{os}}{d_0}\left(1 - \frac{2x}{d_0}\right) \\ &\approx -\frac{1}{2}\frac{C_{os}}{d_0}\left(V_{FA}^2 - \frac{2V_{FA}^2 x}{d_0} - 2V_{FA}|v_i|cos(\omega t) + \frac{4xV_{FA}|v_i|cos(\omega t)}{d_0}\right) \end{aligned} \tag{2.13}$$

The parallel plate transduction capacitance of (2.9) is a nonlinear function of displacement. As a result, when used to drive and sense micromechanical resonators, fixed overlap area capacitive transduction generally results in unfavorable performance characteristics such as frequency response distortion and harmonic distortion in the resonator output current [10]. Because these effects significantly hamper both oscillator and filter performance, fixed overlap area capacitive transduction is not well suited to drive and sense resonators in these applications. However, the nonlinearity of (2.9) does give rise to a frequency-pulling effect that is especially useful when leveraged to yield voltage controlled frequency tuning electrodes.

2.2.1.1 Frequency Pulling

As seen in (2.13), there exists a component of the electrostatic force that is proportional to the moveable plate's displacement. The proportionality between displacement and the component of force is known as the electrical stiffness k_e and is given by

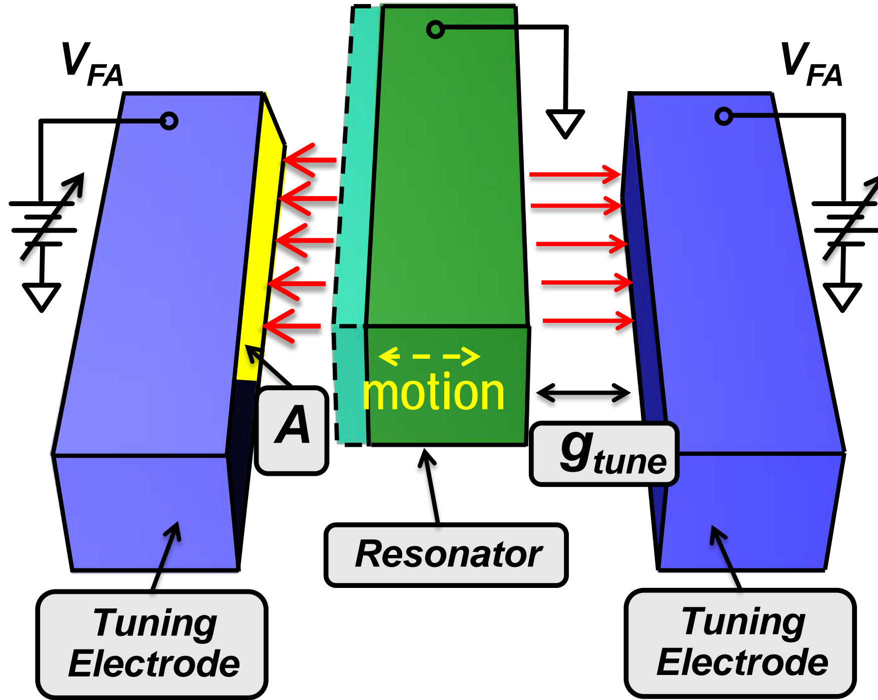

Figure 2.5 Perspective-view schematic describing the mechanism behind electrical stiffness generated by the parallel plate tuning electrodes

$$k_e = \frac{V_{FA}^2 C_{os}}{d_0^2} \tag{2.14}$$

As illustrated in Figure 2.5, this electrical stiffness arises when the plate displacement grows and shrinks. For example, a shrinking gap enhances the electric field generated between the parallel plates due to the potential difference V_{FA}. This varying electric field in turn generates an attractive force between the parallel plates. Because the generated attractive force varies linearly in phase with the moveable plate's displacement, the plate can be viewed as possessing a negative stiffness that counteracts the mechanical stiffness k_m associated with the movable plate. If the movable plate is considered a resonator with a mass m, its resonance frequency f_0 is given by

$$f_0{}' = \frac{1}{2\pi}\sqrt{\frac{(k_m - k_e)}{m}} = f_0\sqrt{1 - \frac{V_{FA}^2 C_{os}}{k_m d_0^2}} \tag{2.15}$$

Because the electrical stiffness of (2.14) is a function of the dc voltage held across the parallel plates, the resonance frequency of the resonator shown in Figure 2.7 can be adjusted negatively by applying a larger voltage across the plates.

2.2.2 Capacitive-Comb Transduction

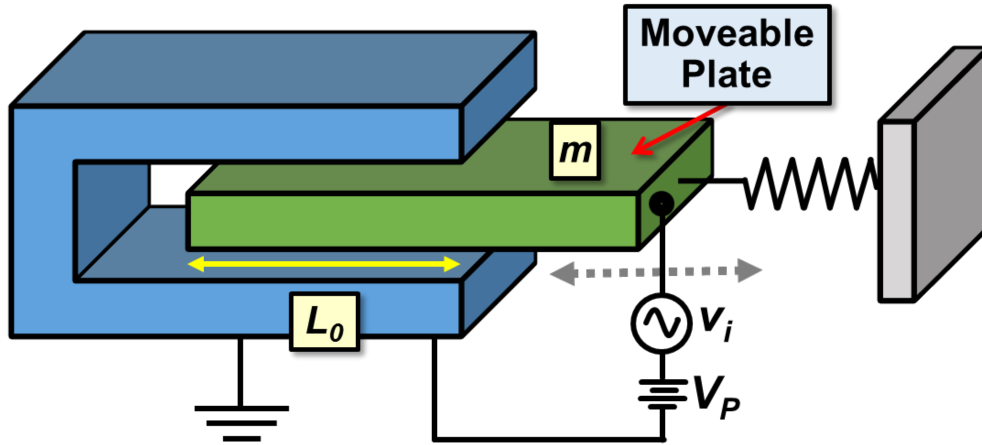

Figure 2.6: Perspective-view schematic of the capacitive-comb transduction configuration

When designing a resonator to be utilized in a frequency-selective application such as a clock oscillator or bandpass filter, frequency stability is of utmost concern. As previously mentioned, a drive capacitance that varies nonlinearly with displacement directly leads to resonance frequency instability. With stability in mind, the electrode-to-resonator capacitance should be designed to vary linearly with displacement. This can be achieved by employing capacitive-comb (fixed gap) transduction.

In the capacitive-comb transduction configuration, illustrated in Figure 2.6, the moveable electrode is free to move in a direction parallel to the fixed electrode, resulting in a modulation of the parallel-plate capacitor's overlap area *A*. Neglecting fringing fields, the parallel-plate capacitance can be approximated as

$$C_{fg}(x) = \frac{\varepsilon_0 h}{d_0}(L_0 + x) \tag{2.16}$$

where h is the plate thickness and L_0 is the initial overlap length. Differentiating (3.8) yields a constant change in capacitance per displacement given by

$$\frac{\partial C_{fg}}{\partial x} = \frac{\varepsilon_0 h}{d_0} \tag{2.17}$$

The capacitive-comb transduction force is derived by combining (2.5) and (2.17) to yield

$$F_{fg} = \frac{1}{2}\left(V_P^2 + \frac{|v_i|}{2} - 2V_P|v_i|\cos(\omega t) + \frac{|v_i|^2}{2}\cos(2\omega t)\right)\frac{\varepsilon_0 h}{d_0} \tag{2.18}$$

As previously mentioned, when the excitation signal v_i has a frequency matching the resonance frequency of the resonator and the resonator's Q is large ($\gg 10$), the component at ω will dominate and all other terms can be neglected. This effect results in the simplified expression for capacitive-comb transduction force

$$\boldsymbol{F_{fg} = -V_p \frac{\varepsilon_0 h}{d_0} v_i} \tag{2.19}$$

Because (2.19) does not depend on displacement, this transduction configuration does not result in an electrical stiffness. Therefore, a capacitive-comb transduced resonator's frequency should ideally be independent of the dc-bias voltage V_P.

2.3 Frequency Tunable Micromechanical Resonator Design Topology

Figure 2.7 presents a perspective view of a capacitive-comb transduced folded-beam micromechanical resonator. This design essentially mimics the classic design of [43], except that it utilizes interdigitated capacitive-comb finger transducers for not only drive and sense, but also for frequency tuning. In particular, the drive and sense electrodes represent the capacitive-comb transducers of Section 2.2.2, which in turn realizes the a linear displacement-to-capacitance transfer function that alleviates frequency instability [10] and (ideally) eliminates frequency dependence on applied voltages [44]. On the other hand, the fingers of the tuning electrodes represent the fixed-overlap-area capacitive transducers of Section 2.2.1. These transducers generate a nonlinear displacement-to-capacitance transfer function that realizes a voltage-controlled electrical stiffness suitable for post-fabrication frequency tuning [12].

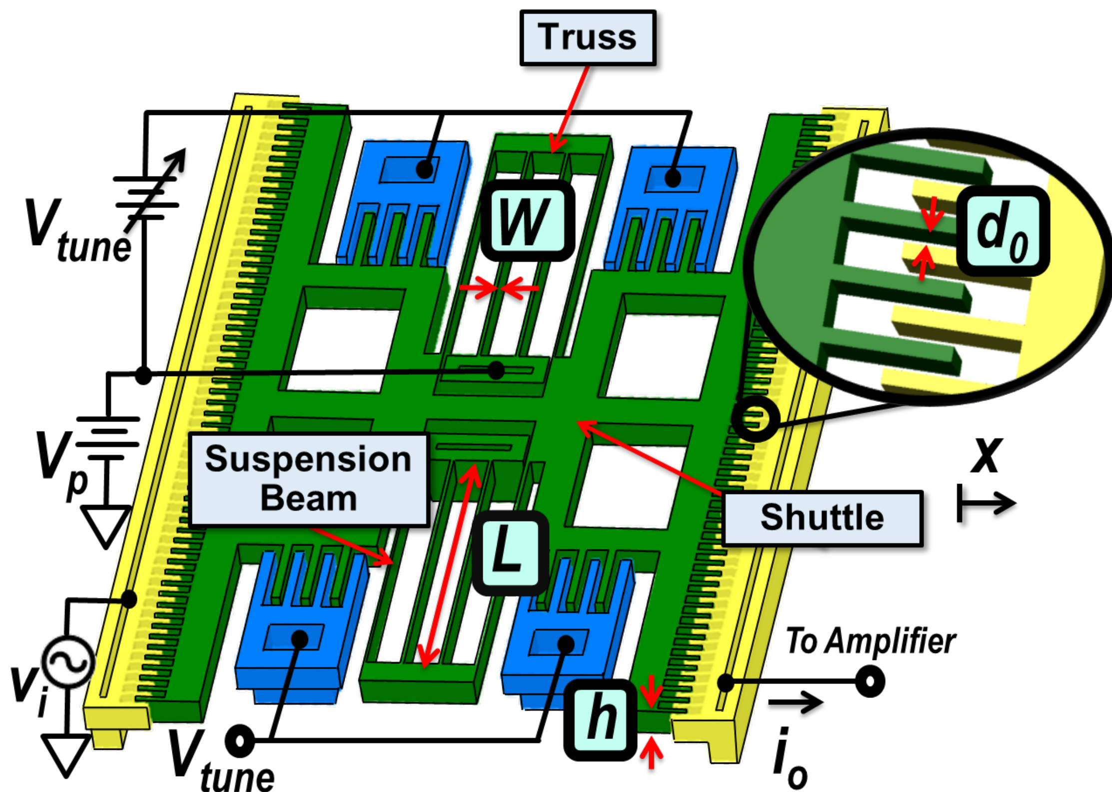

Figure 2.7: Perspective-view schematic of a frequency tunable capacitive-comb transduced folded-beam micromechanical resonator

To excite the resonator into vibration, a dc voltage V_P applied to the resonator shuttle creates an electric field between the shuttle and electrode fingers. An ac (sinusoidal) signal at the device's resonance frequency applied to the input capacitive-comb electrode modulates the electric field across the electrode-to-resonator gap, thereby producing a force that drives the resonator into resonance vibrational motion. This motion, in turn, modulates the dc-biased capacitance between the vibrating resonator and output electrode fingers, generating an electric current that serves as the device's output.

2.3.1 Lumped Mechanical Parameters

As previously, mentioned, mechanical resonators typically behave like the lumped parameter mass-spring-damper system of Figure 2.1. When considering resonator motion confined to the *x*-direction, the lumped mechanical parameters of Figure 2.7 are well established [9] and can be expressed as

$$\boldsymbol{k_r = 2Eh\left(\frac{W}{L}\right)^3} \tag{2.20}$$

$$\boldsymbol{m_r = M_P + \frac{1}{4}M_t + \frac{12}{35}M_b}$$

$$\boldsymbol{c_r = \frac{\sqrt{k_r m_r}}{Q}}$$

where E is Young's modulus; h is the resonator's thickness; W and L represent the folded-beam widths and lengths respectively; M_P, M_t, and M_b correspondingly represent the total mass of the resonator's shuttle, the sum of the two horizontal trusses, and the sum of the eight parallel beams.

While the mass-spring-damper model depicted in Figure 2.1 is useful in conceptualizing the device's mechanical operation, is it perhaps more useful to represent the mechanical lumped parameters as equivalent lumped circuit elements that obey Kirchoff's circuit laws [40]. These equivalent circuit values are summarized in Table 2.2.

Table 2.2: Equivalent Lumped Circuit Elements and their Corresponding Lumped Mechanical Parameters

Circuit Component	Value
Capacitor	$1/k_r$
Inductor	m_r
Resistor	c_r

2.3.2 Equivalent Two-Port Circuit Neglecting Voltage-Tuning

In order to design electrical systems that incorporate the design topology of Figure 2.7 it is useful to determine the transduced resonator's equivalent lumped circuit parameters (LCR values) to apply the electrical domain expressions of Table 2.1 and utilize an equivalent schematic similar to Figure 2.2. This section will apply the results of well documented equivalent lumped parameter derivations [40][10][45] to yield an overall equivalent circuit model for the capacitive-comb transduced folded-beam resonator used throughout this dissertation. Initially, voltage controlled-tuning effects are ignored ($V_{Tune} = 0$), however these effects are incorporated into the equivalent circuit model in the following section.

The electromechanical coupling factor, a coefficient that relates electrical current to mechanical velocity, serves as the bridging link between domains and is schematically represented as the turns ratio of an electrical transformer. In general, η is expressed as

$$\boldsymbol{\eta = V_P \left(\frac{\partial C}{\partial x}\right)} \qquad (2.21)$$

Because the drive and sense transducers are equivalent to 2N capacitive-comb transducers in

parallel, where N is the number of comb fingers per side, equations (2.17) and (2.21) can be combined to yield the capacitive-comb electromechanical coupling factor:

$$\boldsymbol{\eta = V_P \frac{2N\varepsilon_0 h}{d_0}} \tag{2.22}$$

Noting that the resonator topology of Figure 2.7 has symmetric drive and sense transducers and neglecting voltage-tuning effects, equation (2.22) combined with the equivalent lumped circuit elements summarized in Table 2.2 allows for the equivalent circuit model depicted in Figure 2.8.

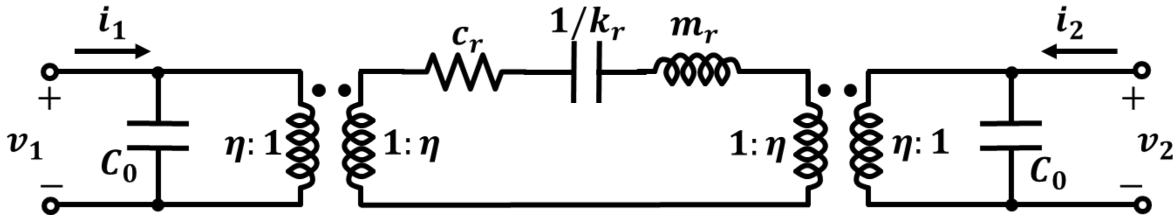

Figure 2.8: Equivalent two-port transformer model for the resonator topology of Figure 2.7, neglecting voltage-tuning effects

While the circuit of Figure 2.8 is certainly useful and can be directly imported into popular circuit analysis tools such as SPICE and Keysight ADS, because the design topology utilizes symmetric drive and sense electrodes, the circuit can be further simplified by "folding" the electromechanical coupling factor into the resonator's lumped mechanical parameters. This simplification results in the transformer-less series LCR circuit model of Figure 2.9 with elements given by:

$$\boldsymbol{C_x = \frac{\left[V_P\left(\frac{\partial C}{\partial x}\right)\right]^2}{k_r} = \frac{\left[V_P\frac{N\varepsilon_0 h}{d_0}\right]^2}{k_r} = \frac{\eta^2}{k}} \tag{2.23}$$

$$L_x = \frac{k_r}{\omega_0^2\left[V_P\left(\frac{\partial C}{\partial x}\right)\right]^2} = \frac{k_r}{\omega_0^2\left[V_P\frac{N\varepsilon_0 h}{d_0}\right]^2} = \frac{m_r}{\eta^2} \tag{2.24}$$

$$R_x = \frac{k_r}{\omega_0 Q\left[V_P\left(\frac{\partial C}{\partial x}\right)\right]^2} = \frac{k_r}{\omega_0 Q\left[V_P\frac{N\varepsilon_0 h}{d_0}\right]^2} = \frac{\sqrt{k_r m_r}}{Q\eta^2} \tag{2.25}$$

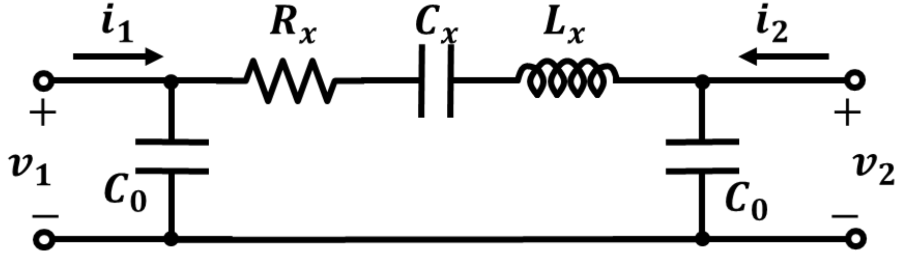

Figure 2.9: Simplified LCR model for the resonator topology of Figure 2.7, neglecting voltage-tuning effects

Equations (2.23) through (2.25) indicate that the equivalent LCR circuit parameters for a capacitive-comb transduced folded-flexure are strong functions of the resonator's dc-bias V_P and the transduction capacitance per displacement ratio $\partial C/\partial x$.

For both oscillator and filter applications, it is often desirable to maximize the current seen exiting the output transducer when an ac-sinusoidal signal with a frequency equal to the resonator's natural frequency ω_0 is applied to the resonator's input transducer. Because capacitor and inductor impedances cancel at resonance, output current is increased in designs with lower R_x values. This suggests design efforts should focus on maximizing resonator Q, minimizing the $k_r m_r$product, and maximizing the electromechanical coupling factor η.

2.3.3 Equivalent Two-Port Circuit with Voltage-Tuning

The equivalent circuit of Figure 2.9 is particularly useful when formulating the initial resonator design because it provides a simple and intuitive insight into the device's operation. However, this schematic must be modified to account for the voltage-controlled tuning provided by the fixed overlap area transducers shown in Figure 2.7.

As emphasized in Section 2.2.1.1, a static dc potential, V_{tune} in this case, held across the fixed-overlap-area transducer gives rise to an electrostatic force that is proportional to the moveable plate's displacement. The proportionality constant between this electrostatic force and the plate's displacement is known as the electrical stiffness k_e given by

$$k_e = \frac{N_{tune} V_{tune}^2 C_{os}}{d_{tune}^2} \tag{2.26}$$

Where N_{tune} is the total number of fixed-overlap-tuning electrodes, C_{OS} is the static overlap capacitance across a single tuning transducer, and d_{tune} is the initial gap spacing between the parallel plates.

Because the electrical stiffness term arises from an attractive force that counteracts the mechanical stiffness of the resonator k_r, the overall stiffness of the system must be equal to $k_r - k_e$. Mechanically, this is equivalent to two springs acting in parallel, with the electrical stiffness having an opposite sign from the mechanical stiffness. Since, mechanical springs are

schematically modelled as capacitors with values equal to the inverse of their stiffness, the electrical stiffness term can be readily incorporated into the resonator schematic of Figure 2.8 by placing the electrical stiffness voltage-dependant capacitor in series with the mechanical stiffness capacitor. The new overall two-port transformer model schematic including voltage-controlled tuning transducers is depicted in Figure 2.10.

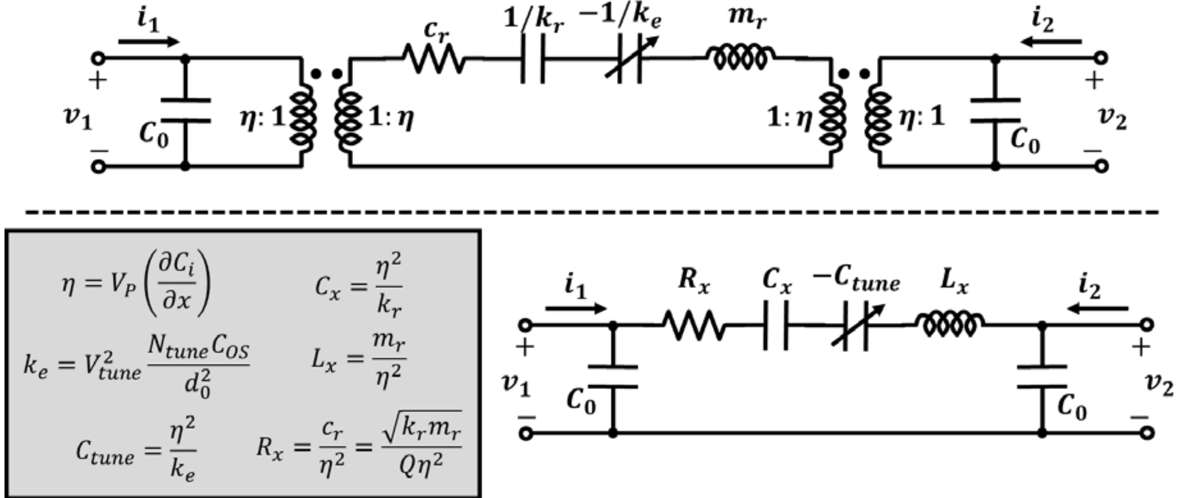

Figure 2.10: Transformer and simplified LCR schematic representation of the voltage-tunable capacitive-comb driven resonator of Figure 2.7

Utilizing the analysis techniques demonstrated in the previous section, the model can once again be reduced to a simple LCR circuit because the input and output transducers are symmetric. Again, the electromechanical coupling factor is folded into the circuit, yielding a series LCR tank with component values given by equations (2.3) through (2.5). In addition, the LCR tank is placed in series with a negative variable capacitor with a value given by

$$C_{tune} = \frac{\eta^2}{k_e} = \frac{\eta^2}{V_{tune}^2} \frac{d_0^2}{N_{tune} C_{OS}} \tag{2.27}$$

As a confirmation of the model, when V_{tune} is set to 0V, C_{tune} becomes a capacitor with infinite capacitance and can be considered a short circuit. In this case, the equivalent tuning capacitor can be neglected, resulting in the equivalent circuit of Figure 2.9.

2.4 Typical Resonator Design Values

In order to gain a better intuition for the equivalent circuit models of Figure 2.9 and Figure 2.10, it is instructive to consider typical resonator design values. Table 2.3 presents resonator design values and equivalent circuit values for a 34-kHz polysilicon resonator with an expected Q of 50,000. This design employs 57 comb fingers on a side and an intended dc-bias voltage of 1.65 V. When considering the equivalent circuit values, careful attention should be payed to the series motional resistance R_x. This parameter is specifically important to

oscillator [46] and filter design [47].

Table 2.3: Typical Capacitive-Comb Transduced Resonator Design Values

Parameter	Value	Units
E	150	GPa
W	0.5	µm
L	45	µm
h	2	µm
d	0.6	µm
N	57	comb-fingers/side
M_p	1.73×10^{-11}	kg
M_t	7.21×10^{-13}	kg
M_b	8.28×10^{-13}	kg
m_r	1.79×10^{-11}	kg
k_r	0.82	N/m
f_0	34.0	kHz
Q	50000	–
V_P	1.65	V
H	2.77	nF/m
R_x	2.48	MΩ
C_x	37.4	aF
L_x	581	kH
C_o	8.41	fF

2.5 Resonator Fabrication

Resonators were fabricated using a conventional 3-mask process flow [43][47] following the cross-sections shown in Figure 2.11. Here, the fabrication steps largely mimic that of previously demonstrated comb-driven resonators, but differ in the use of an ASML300 Deep-UV Stepper for lithography, capable of achieving 0.25µm resolution when operating under ideal conditions [48]. This stepper permits critical features substantially smaller in size than any other published resonator of this type.

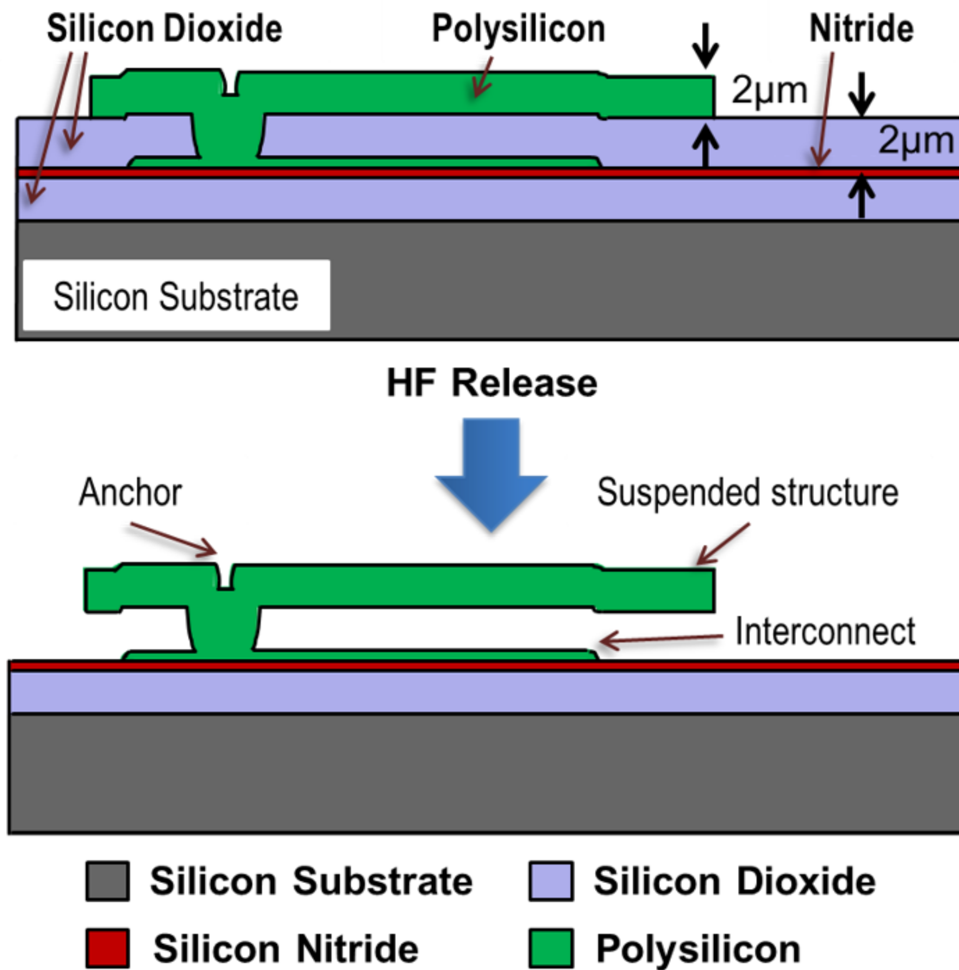

Figure 2.11: Cross-sections succinctly illustrating the fabrication process flow used to achieve capacitive-comb driven devices.

Figure 2.12 presents a scanning electron micrograph (SEM) of a fabricated 32-kHz capacitive-comb driven resonator with 600 nm suspension beam widths and 550 nm capacitive-comb finger gaps. These diminutive features combine to deliver a compact device footprint measuring just 110 μm × 140 μm, or 0.0154mm^2. This compact area is more than 100× smaller than the smallest packaged commercial quartz clock-resonator [20] and at least 4× smaller than the smallest previously demonstrated MEMS-based research resonator [13]. The design and characterization of this resonator will be outlined in the Chapter 3.

The SEM of a 523-kHz coupled resonator filter is presented in Figure 2.13. This device is comprised of four mechanically coupled resonators and in total occupies an area of 146 μm × 872 μm. Here each coupled resonator possesses independent tuning electrodes that allow for the application of an automated passband correction protocol. The design and characterization of this device is detailed in Chapter 4.

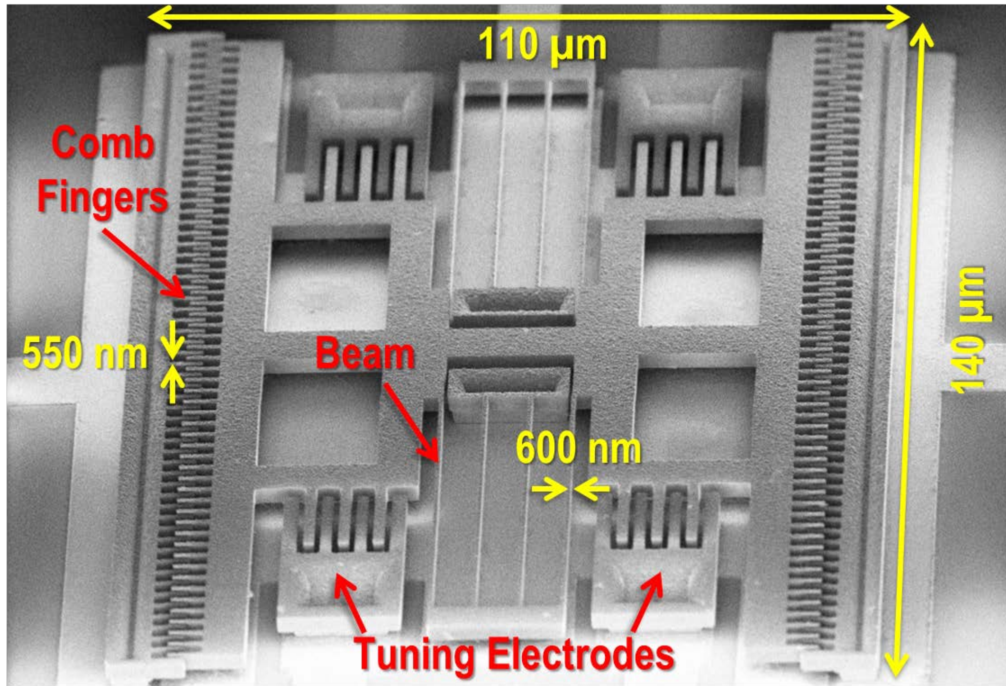

Figure 2.12: SEM of a fabricated 32-kHz capacitive-comb driven folded-beam frequency tunable MEMS-based resonator.

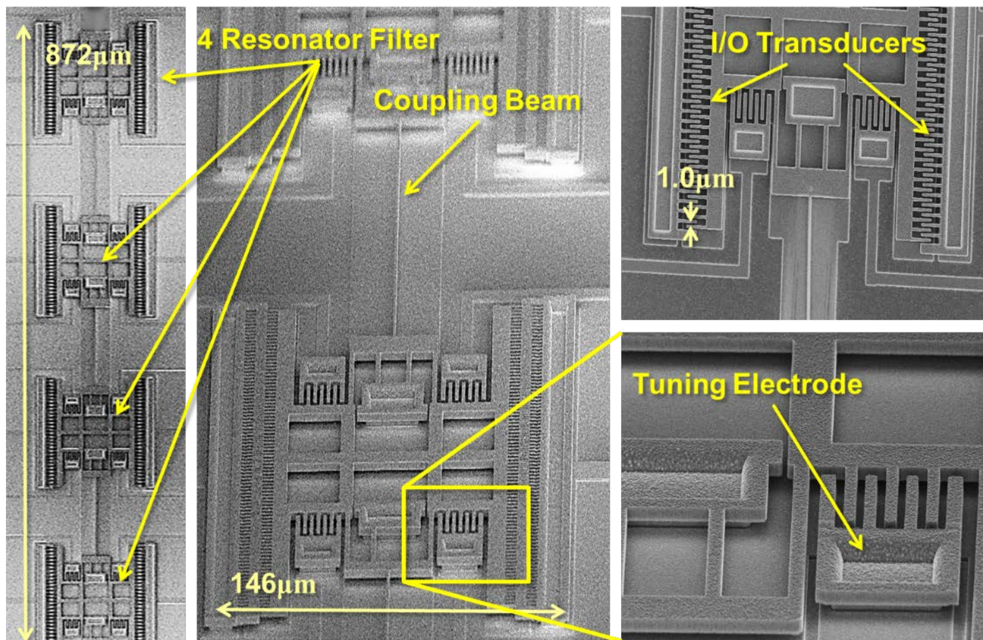

Figure 2.13: SEM of a fabricated 523-kHz coupled resonator filter.

3. A MEMS-BASED REAL-TIME CLOCK

In this chapter, the resonator topology outlined in Section 2.3 is combined with a custom designed ASIC, yielding a compact, ultra-low power 32.768-kHz clock oscillator. First, a discussion of the resonator's design is overviewed with special emphasis paid to its immense scaling benefits. Next, focus shifts the design and implementation of a CMOS sustaining amplifier designed with low power in mind. Finally, experimental results are presented and comparisons are made to previously demonstrated works.

3.1 Resonator Design

Figure 3.1 presents a schematic of the overall 32.768-kHz oscillator that embeds the capacitive-comb transduced folded-beam micromechanical resonator highlighted in the previous section in a positive feedback loop with a CMOS sustaining amplifier (to be described in more detail, later). The resonator device consists of a 2 μm thick n-doped polysilicon movable shuttle suspended 2 μm above an n-doped polysilicon ground plane and connected to its central anchor points via folded beam suspension springs. As previously outlined, the overall design essentially mimics the classic design of [43], except that it utilizes interdigitated capacitive-comb finger transducers for not only drive and sense, but also for frequency tuning. In particular, the drive and sense electrodes employ interdigitated fingers that slide relative to one another in a motion that maintains constant gap spacings, which in turn realizes a linear displacement-to-capacitance transfer function that (ideally) eliminates frequency dependence on applied voltages. On the other hand, the fingers of the tuning electrodes move towards or away from one another, in parallel-plate fashion, where their gap spacings mimic shuttle displacements. This generates a nonlinear displacement-to-capacitance transfer function that realizes a voltage-controlled electrical stiffness suitable for frequency tuning [12].

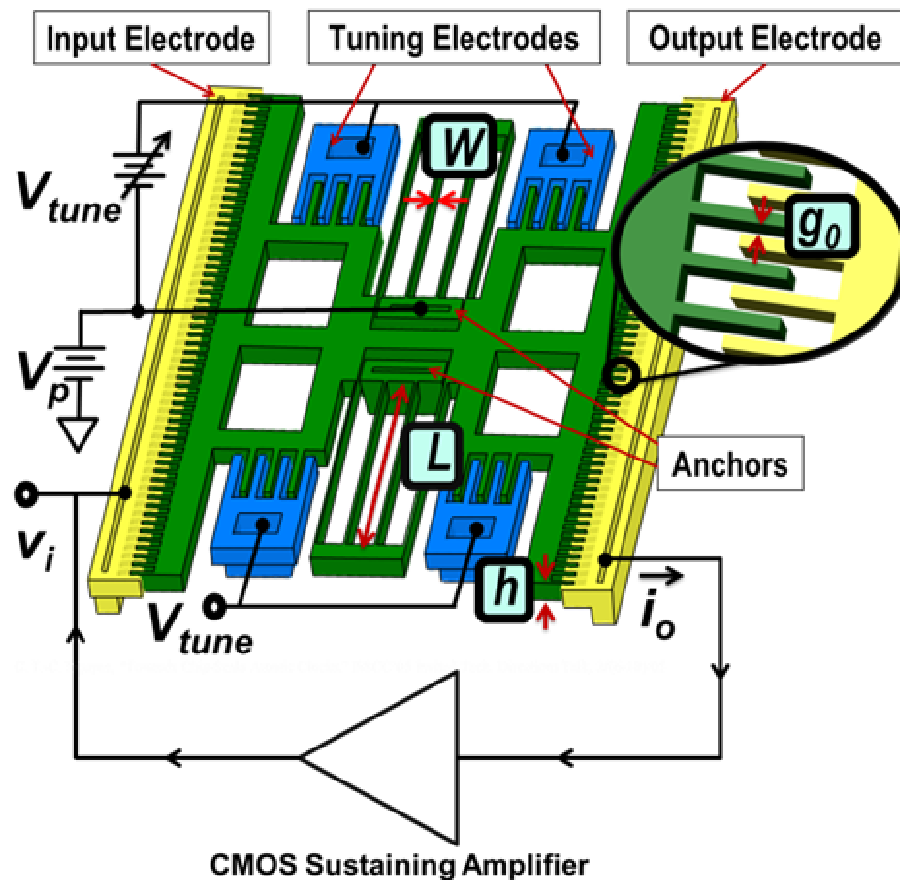

Figure 3.1: Perspective-view schematic of the tunable capacitive-comb driven folded-beam resonator connected in a series-resonant oscillator circuit

3.1.1 Benefits of Scaling

As previously mentioned in Section 2.3, the electrostatic-comb driven resonator first established by William Tang [49] represents an excellent low frequency surface micromachined resonator design topology because the drive and sense electrodes employ interdigitated fingers that maintain constant gap spacings, which in turn realizes a linear displacement-to-capacitance transfer function. While this design is already rich in benefits, from the stress-relief afforded by its folded beams, to the frequency stability provided by sliding interdigitated comb-fingers, perhaps its most important benefit is the rate at which reductions in its lateral dimensions decrease its areal footprint and motional resistance.

The resonance frequency of the capacitive-comb transduced folded-beam resonator of this work is given by [50]

$$f_0 = \frac{1}{2\pi}\sqrt{\frac{2Eh\left(\frac{W}{L}\right)^3}{M_e}} \tag{3.1}$$

where E is Young's modulus; h is thickness; W and L are widths and lengths, respectively, of the beams used in the folded-beam suspension. M_e represents dynamic mass of the resonator which is evaluated using Rayleigh's energy method as [9]

$$M_e = M_p + \frac{1}{4}M_t + \frac{12}{35}M_b \tag{3.2}$$

where M_P, M_t, and M_b represent the total mass of the resonator's shuttle, the sum of the two horizontal trusses, and the sum of the eight parallel beam. While Young's E and thickness h are dictated by the fabrication process, the design is still open ended, particularly regarding the folded-beam dimensions. As indicated in (3.1), when lateral dimensions W and L are scaled by the same factor, their ratio W/L remains fixed, which means the resonance frequency stays the same, so long as $M_P >> M_b$.

One of the most important factors determining oscillator performance is resonator motional resistance R_x. For many oscillator configurations, minimizing R_x not only reduces power consumption, it also raises the power handling ability of the resonator, which, in turn, can contribute to improved noise performance. For the resonant structure of this work, the motional resistance is given by [50]

$$R_x = \frac{1}{\pi}\frac{E}{f_0 Q}\left(\frac{W}{L}\right)^3\frac{1}{h}\left(\frac{g_0}{2N\varepsilon_0 V_P}\right)^2 \tag{3.3}$$

where Q is the resonator quality factor; N is the total number of input/output (I/O) comb-fingers on the resonator shuttle; and g_0 is the spacing between them, assumed equal for all finger pairings. As seen in Figure 3.8, like resonance frequency, R_x remains constant with constant W/L scaling. However, if one reduces the gap spacing g_0 in addition to structure lateral dimensions, the motional resistance shrinks very quickly, by a square law.

Of course, device footprint also scales with lateral dimensions. For the resonator design of this work, the die area consumed can be approximated according to

$$Die\ Area \approx \alpha L^2 \tag{3.4}$$

where α is a design-specific scale factor equal to 7.5 for the device of this work. From (3.3) and (3.4), when all lateral dimensions (i.e., W, L, and g_0) shrink by scale factor S, both die area and R_x decrease dramatically by S^2. Figure 3.2 illustrates this point by plotting both die area

and R_x against lithographic resolution (assumed to set the minimum W and g_0). As shown, the smallest lithographically defined features in this work are 550 nm, yielding a motional resistance of 2 MΩ (for a dc-bias V_P=1.65 V) and a die area of 0.015 mm^2 (≈0.12 mm×0.12 mm). The ASML300 Deep-UV stepper employed to achieve these small features actually boasts the capability of attaining features as small as 0.25 μm in a production environment [48], and if gaps and features this size were possible, they would yield a significantly smaller die area of 0.0027 mm^2 (≈0.05 mm×0.05 mm) and an R_x value of only 400 kΩ at the same dc-bias voltage. Ultimately, with the use of 20 nm CMOS-grade lithography and patterning techniques already available in industry [51], and with a (big) assumption that gaps and features this size can be attained in 2 μm-thick structural material, this design is theoretically capable of scaling to an extremely small die area of only 0.000002 mm^2 (≈1.4 μm×1.4 μm), while achieving an R_x of just 3 kΩ with V_P=1.65 V.

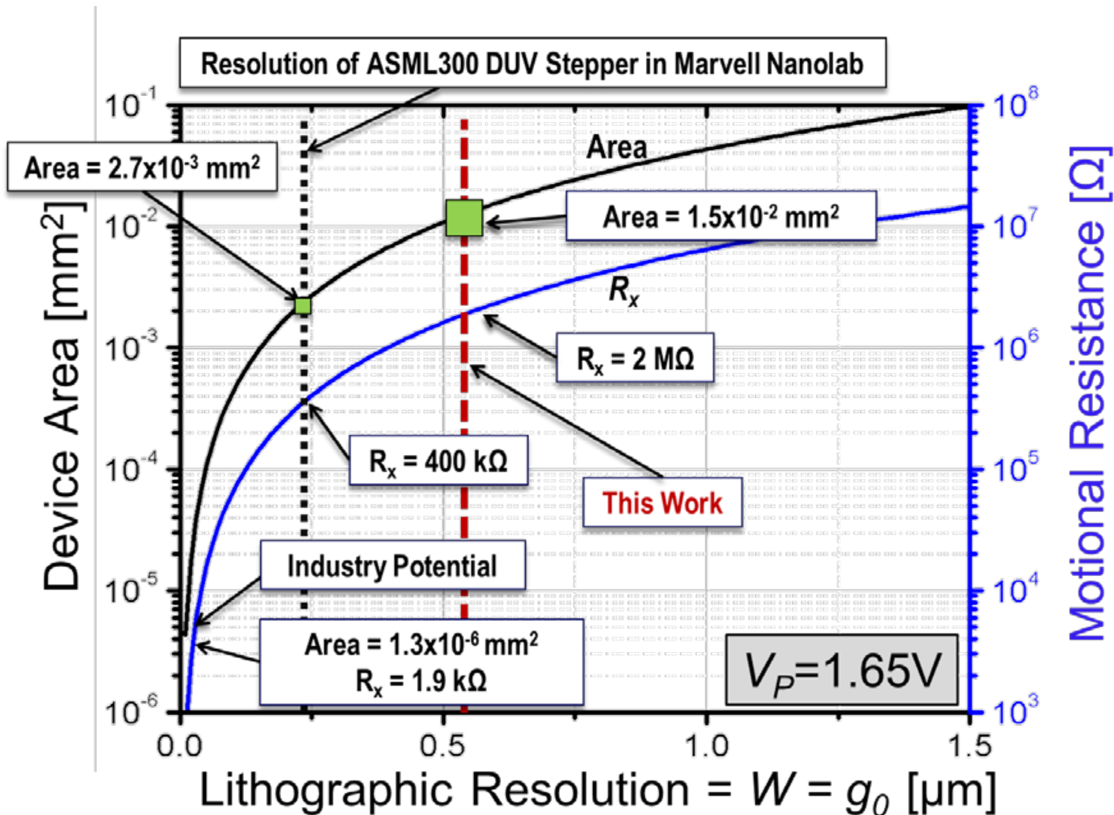

Figure 3.2: Plot illustrating the simulated benefits of both motional resistance R_x and die area when scaling down critical dimensions W and g_0 as lithographic resolution improves

When comparing resonator performance it is often beneficial to consider electromechanical coupling efficiency. Another benefit of lateral dimensional scaling is an enhancement of the resonator's electromechanical coupling efficiency as feature sizes are reduced. The electromechanical coupling efficiency of a given resonator is commonly gauged by its motional-to-static transducer capacitance ratio C_x/C_0. For the capacitive-comb transduced resonator of this work the static capacitance C_0 is written as

$$C_0 = \frac{N\varepsilon_0 h L_0}{g_0} \tag{3.5}$$

where L_0 is the static comb-finger overlap length. The motional transducer capacitance C_x is written as

$$C_x = \frac{\eta^2}{k_m} = \frac{V_p^2 \left(\frac{N\varepsilon_0 h}{g_0}\right)^2}{2Eh\left(\frac{W}{L}\right)^3} \tag{3.6}$$

With equations (3.5) and (3.6) handy, the motional-to static transducer ratio C_x/C_0 is simplified to

$$\frac{C_x}{C_0} = \frac{NV_p^2\varepsilon_0}{2g_0\left(\frac{W}{L}\right)^3} \tag{3.7}$$

Again, like resonance frequency and R_x, this ratio remains fixed with constant W/L scaling. However, the coupling efficiency improves dramatically if the resonator to electrode gap spacing is scaled as well. With a V_P of 1.65 V and the gap spacing of 550 nm achieved in this work, C_x/C_0 is calculated to be 0.52%. While this efficiency already represents a significant improvement over existing technologies including quartz tuning forks (C_x/C_0 = 0.22%) [52], if the gap spacing of 250 nm could be achieved, the coupling efficiency will balloon to 1.1%

3.1.2 Voltage-Controlled Frequency Tuning

Although the above orders of magnitude improvements in both die area and R_x as lithographic feature sizes shrink are impressive, concerns naturally arise regarding center frequency variance from device-to-device, especially as features aggressively scale down. To circumvent this problem, the Figure 3.1 design employs voltage-controlled frequency tuning, made possible by electrical stiffnesses generated by the parallel-plate transducers previously mentioned in Section 2.2.1.1.

As illustrated in Figure 2.5, this electrical stiffness k_e arises when the gap g_{tune} between a resonator finger and a tuning-electrode finger grows and shrinks. For example, a shrinking gap enhances the electric field generated by the tuning electrode-to-resonator potential difference V_{tune}. This varying electric field, in turn, generates an attractive force that varies in phase with and is proportional to the shuttle displacement—attributes that fit the definition of a negative stiffness. As emphasized in equation (2.5), the electrical stiffness k_e, being negative, counteracts the mechanical stiffness k_m, resulting in a downward shift in frequency.

Note that because the dc-bias voltage V_P does not appear in (2.14) or (3.1), it does not

influence the electrical stiffness, so the resonance frequency of the resonator remains unaffected by fluctuations in V_P. This, in turn, means that the resonator's motional resistance (given by (3.3)) and resonance frequency (given by (3.1)) can be set independently of one another, with the former set by V_P, and the latter by V_{tune}. In other words, the frequency of this device can be adjusted without affecting its motional resistance—a very important characteristic for any resonator used in a tunable oscillator.

As observed in equation (2.14), in addition to the applied tuning voltage V_{tune}, k_e depends on the lithographically designable features A_{tune} and g_{tune}, meaning the resonator and tuning-electrode designs dictate the overall tuning range. The tuning-electrodes of this work feature 1 μm gaps that allow for a 50,000 ppm frequency tune over a 3.3 V tuning voltage range, as shown by the measured curve of Figure 3.3.

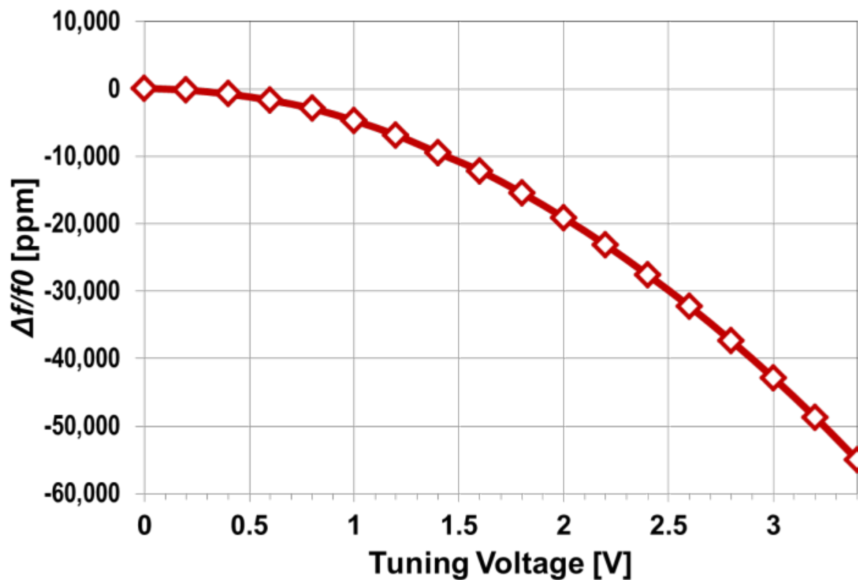

Figure 3.3: Measured plot of resonance frequency versus tuning voltage for the device of Figure 3.16.

3.1.3 Resonator Design Constraints and Considerations

When designing a micromechanical resonator, careful attention must be payed to its specific geometries and materiel properties. The resonator design of this section is constrained by three important parameters: 1) resonance frequency, 2) motional resistance, and 3) die area. When incorporated as the frequency selective component of a real-time clock oscillator, each of these parameters greatly affects the oscillator's performance with respect to power consumption and manufacturing cost.

As previously discussed, the resonator design of Figure 3.1 maintains a relatively constant resonance frequency as folded-beam dimensions W and L are laterally scaled. Therefore, from an area perspective, it is beneficial to set W to the minimum resolvable feature size. To further constrain the resonator's designable geometries, motional resistance R_x should

be minimized because when combined with a series-resonant sustaining amplifier to form an oscillator, reductions in R_x typically lead to reduced oscillator power consumption. Combining the expression for the motional resistance of the resonator of this section, equation (3.3), and the relationship between stiffness, mass, and resonance frequency detailed in equation (2.2) yields

$$\boldsymbol{R_x} = \frac{\sqrt{2Eh\left(\frac{W}{L}\right)^3 M_e}}{Q\left(\frac{2N\varepsilon_0 V_p}{g_0}\right)^2} \tag{3.8}$$

From equation (3.8) it becomes readily apparent that it is beneficial to minimize the capacitive comb finger gap spacings g_0 and the total dynamic resonator mass M_e while maximizing the total number of transduction fingers N. In other words, for a design constrained by minimal motional impedance, the capacitive-comb finger gap spacings should be set to the minimum resolvable feature size and the resonator's dynamic mass should ideally be limited to the combined mass of a large number of rotor fingers. While it is not physically possible to have the entire dynamic mass comprised solely of comb fingers, heavy emphasis should be placed on maximizing the total number of comb fingers while still maintaining a structurally sound resonator shuttle. After the resonator shuttle has been designed, the dynamic mass can be approximated using (3.2). With this dynamic mass in mind, the folded beam length, L is set to dimension that presents the necessary stiffness to the moveable resonator shuttle that results in a lateral resonance frequency of 32 kHz.

Besides critical geometric dimensions, it is also important to consider fabrication defects during the resonator design. As previously mentioned, the resonator topology of this chapter includes parallel-plate tuning transducers to correct for device-to-device variations in resonance frequency. Because these transducers must occupy additional area and contribute to the resonator's dynamic mass, their presence must be observed when specifying critical features. Another significant fabrication effect to consider is stiction, an effect that becomes more troublesome as dimensions shrink [53]. One way to plan for the possibility of post-release stiction is to "cut" sections from the resonator shuttle to allow a probe to slide under the shuttle and "free" the device.

3.1.4 Resonator Design Parameters and Layout

With a strategy for designing for minimal device area and motional resistance in place, concrete resonator design parameters can be established. Figure 3.4 shows the mask layout and Table 3.1 outlines important design parameters, geometries, and equivalent circuit parameters for the main resonator design of this work. It should be noted that the resonance frequency was actually designed to be 34 kHz instead of 32.768 kHz. The reasoning behind this design choice relates back to the electrostatic tuning transducers outlined in Section 2.2.1.1. From equation (2.15) it can be seen that the resonance frequency can only be pulled downward with the application of a dc tuning voltage, even if a negative voltage is applied. This means the resonator should be designed to have a frequency higher than the desired oscillation frequency

so that fabrication imperfections resulting in both positive and negative frequency shifts can be corrected with an applied tuning voltage.

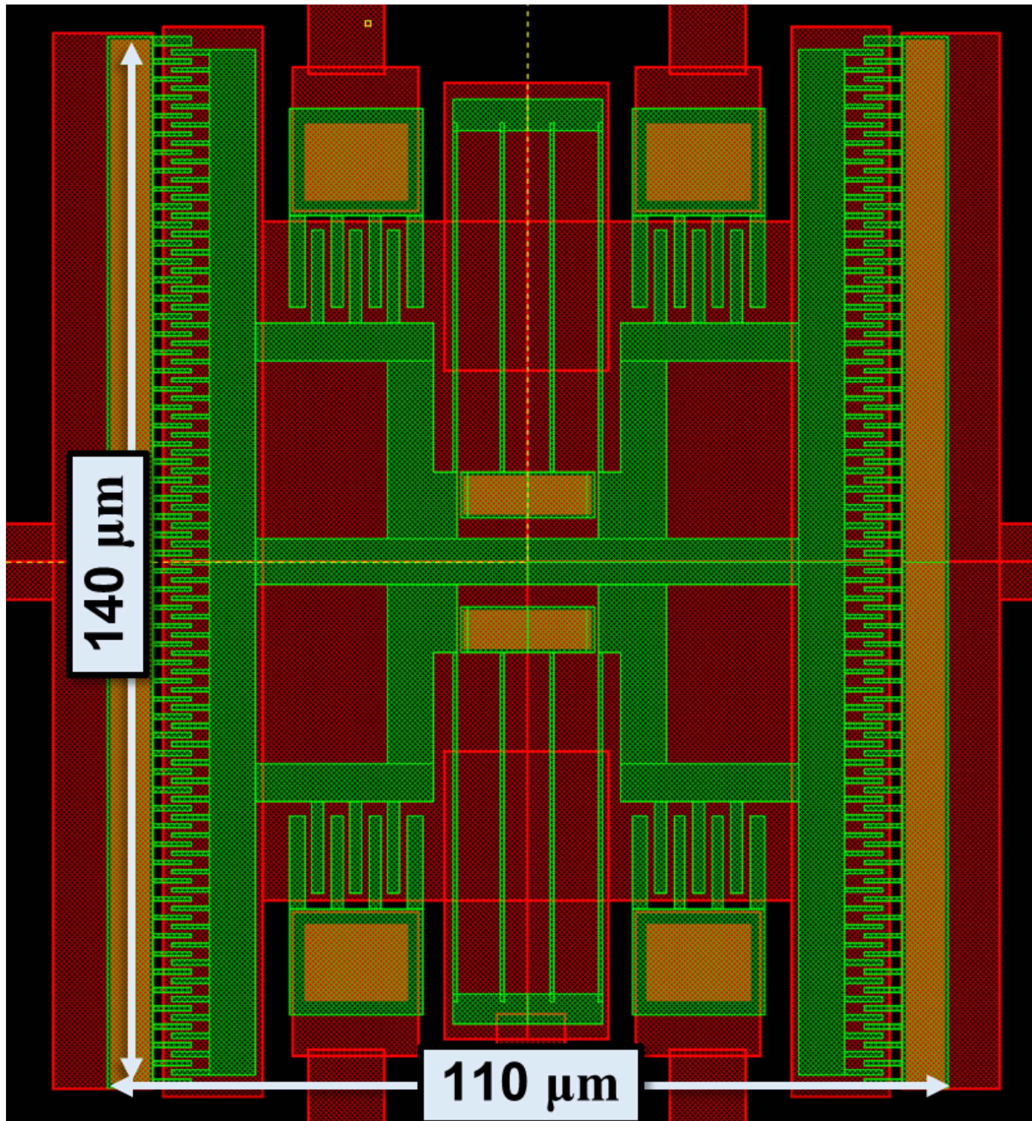

Figure 3.4: Lithographic mask layout for the capacitive-comb transduced resonator of this section

Table 3.1: Capacitive-Comb Transduced Resonator Design Values

Parameter	Value	Units
E	150	GPa
W	0.5	μm
L	45	μm
h	2	μm
d	0.6	μm
N	57	comb-fingers/side
M_p	1.73×10^{-11}	kg
M_t	7.21×10^{-13}	kg
M_b	8.28×10^{-13}	kg
m_r	1.79×10^{-11}	kg
$Area$	0.00154	mm^2
k_r	0.82	N/m
f_0	34.0	kHz
Q	50000	–
V_P	1.65	V
H	2.77	nF/m
R_x	2.48	MΩ
C_x	37.4	aF
L_x	581	kH
C_o	8.41	fF

3.1.5 Resonator FEM Simulation

After resonator geometries have been specified, it is often beneficial and cost-effective to run a finite element method (FEM) modal analysis to yield a more accurate prediction of the post-fabrication resonance frequency. In this dissertation, CoventorWare was employed to provide layout and process specific FEM modal analyses for resonator design iterations. These simulations can also highlight potentially devastating issues that may have been previously overlooked such as electrical shorting resulting from unforeseen shuttle and truss bending.

Figure 3.5 shows the resulting modal simulation of for the design of Figure 3.4. Here the resonance frequency is predicted to be 33.026 kHz, which represents a nearly 30,000 ppm shift from the designed frequency of 34 kHz. In fact, this result was the intentional consequence of several design iterations performed in conjunction with FEM simulations. The predicted frequency lies comfortably above the desired oscillation frequency of 32.768 kHz and well with the designed 3.3-V tuning range of 50,000 ppm.

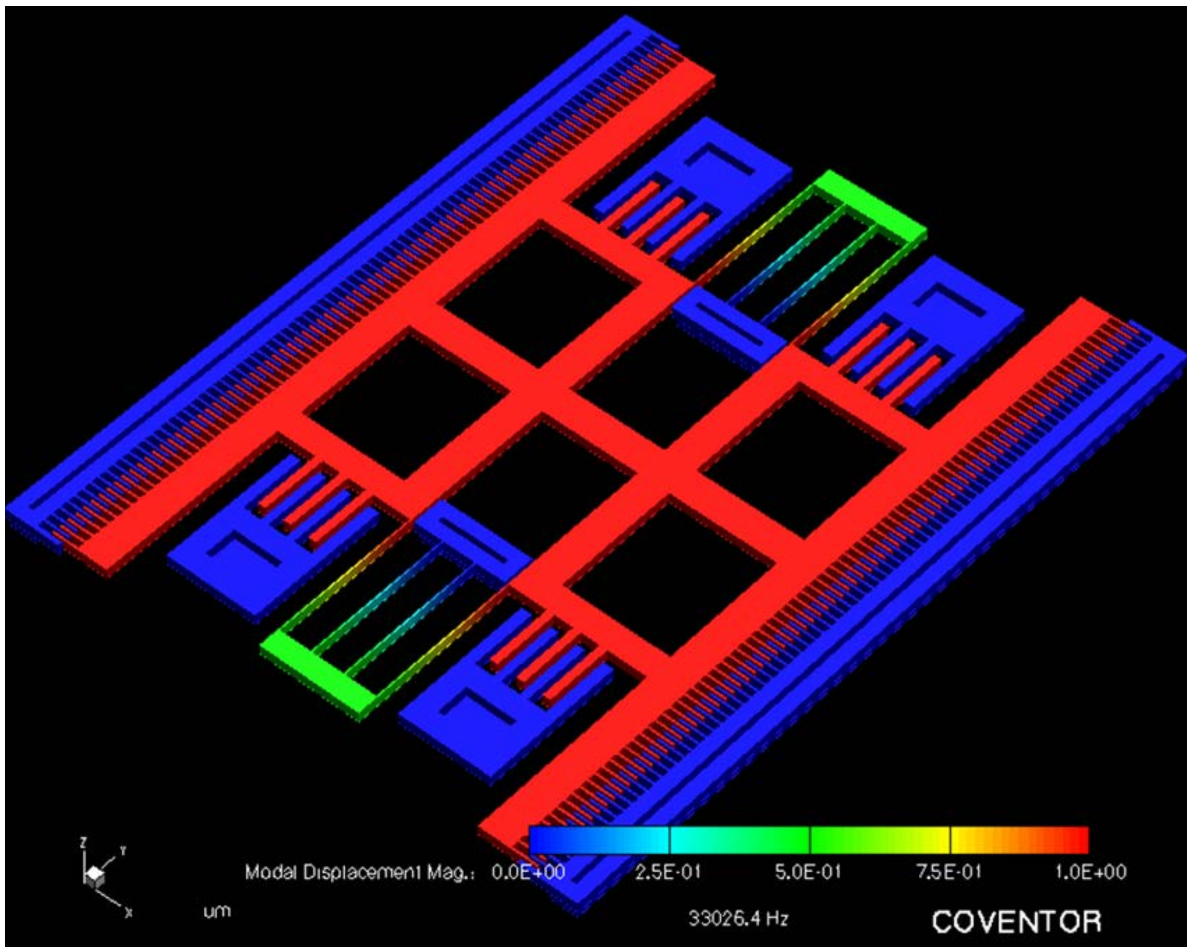

Figure 3.5: Layout and process specific CoventorWare FEM modal analyses for the resonator design of Figure 3.4

3.2 CMOS Sustaining Amplifier

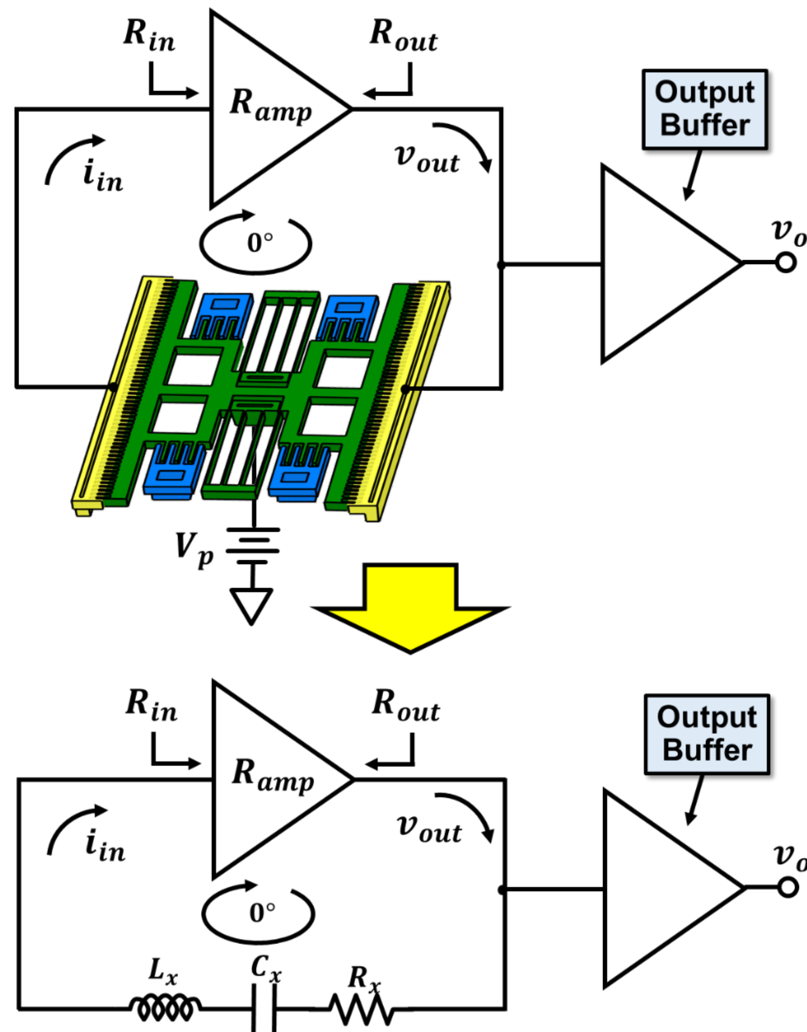

Figure 3.6: Top-level circuit schematic of the series resonant oscillator architecture

To attain the clock oscillator of Figure 3.1, a compatible sustaining amplifier circuit is required. Figure 3.6 presents the oscillator circuit topology used herein. This circuit is comprised of a transresistance amplifier in series with the MEMS resonator, which as previously discussed in Section 2.3.2 can be represented by an *LCR* tank. When the transresistance gain is 2.8 MΩ, this topology yields sufficiently low input and output resistances, on the order of R_i=180 kΩ and R_o=110 kΩ, respectively, to allow a reasonably small transresistance gain R_{amp}, where one necessary condition for sustained oscillation requires

$$\boldsymbol{Ramp} \geq \boldsymbol{R_x} + \boldsymbol{R_i} + \boldsymbol{R_o} \tag{3.9}$$

A second condition for oscillation requires a total 0º phase shift around the oscillator

loop. Since the resonator incurs a 0° phase shift across its input/output (I/O) terminals when operating at series resonance, the amplifier must also provide a 0° phase shift from input-to-output.

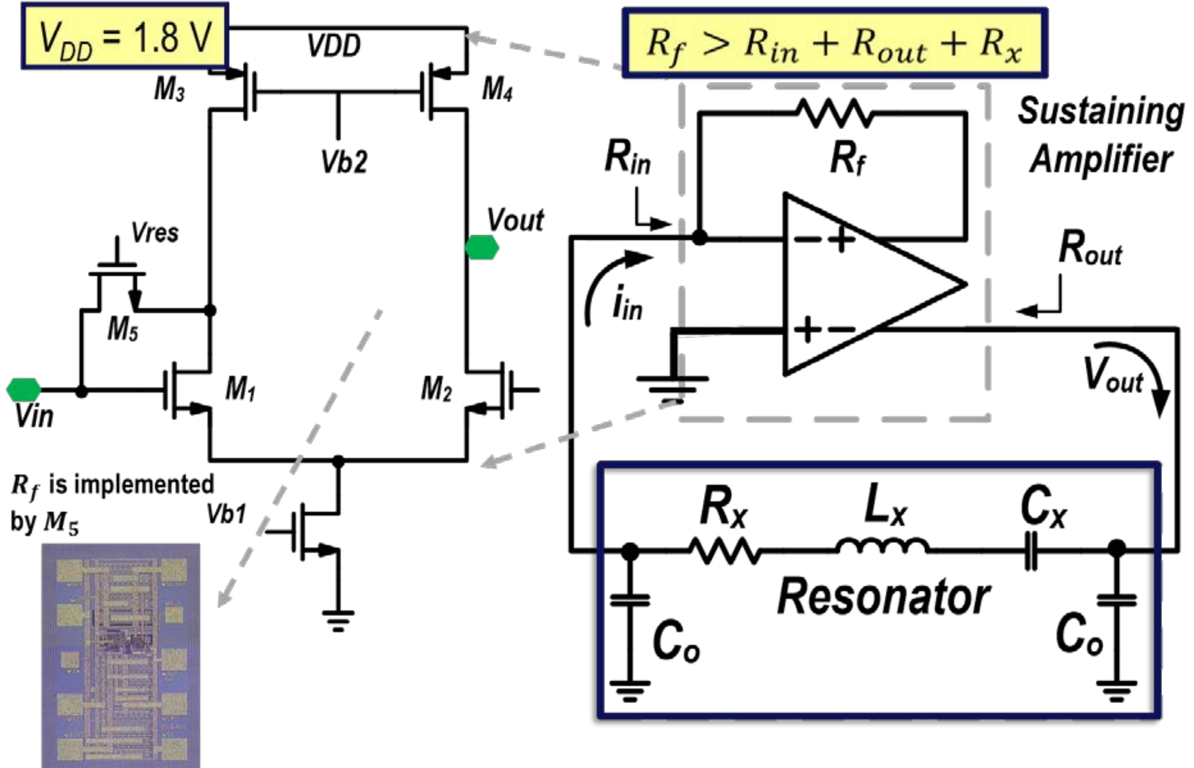

Figure 3.7: Transistor level schematic of the custom-designed transresistance sustaining amplifier presented alongside the op-level circuit schematic of the micromechanical resonator clock oscillator of this chapter.

The circuit of Figure 3.7 satisfies the above criteria for sustained oscillation while utilizing a single gain stage designed to minimize common mode noise [54][55]. The sustaining circuit entails a fully balanced differential CMOS op-amp connected in shunt-shunt feedback on one side, with the output taken from the other side. As detailed in the circuit schematic, the gain stage encompasses transistors M_1-M_4, while transistor M_5 operates as an MOS resistor to set the large transresistance gain needed to satisfy (3.9).

The transresistance gain, input resistance, and output resistance of the sustaining amplifier are expressed as follows:

$$R_{amp} = \frac{\frac{1}{2} g_{m1}(R_f // r_{01} // r_{03}) R_f}{1 + \frac{1}{2} g_{m1}(R_f // r_{01} // r_{03})} \cong \frac{g_{m1} R_f^2}{2 + g_{m1} R_f} \cong R_f \qquad (3.10)$$

$$R_i = \frac{R_f}{1 + \frac{1}{2} g_{m1}(R_f // r_{01} // r_{03})} \cong \frac{2R_f}{2 + g_{m1}R_f} \cong \frac{2}{g_{m1}} \quad (3.11)$$

$$R_o = \frac{R_f // r_{01} // r_{03}}{1 + \frac{1}{2} g_{m1}(R_f // r_{01} // r_{03})} \cong \frac{2R_f}{2 + g_{m1}R_f} \cong \frac{2}{g_{m1}} \quad (3.12)$$

where g_{m1} is the transconductance of M_1, r_{o1} and r_{o3} are the output resistance of M_1 and M_3, respectively. R_f is the MOS resistor value implemented by M_{Rf1} and M_{Rf2}, and is assumed to be much smaller than the circuit's r_os, and the forms on the far rights assume the amplifier's open loop gain $1/2g_{m1}R_f >> 1$.

Expression (3.10) indicates the sustaining amplifier's gain depends primarily on R_f, therefore it might seem reasonable to simply reduce transistor drain currents I_D as much as possible when designing for minimal power consumption. However, the amplifier's input and output resistances, expressed in (3.11) and (3.12) respectively, must also be taken into consideration. To reduce Q loading effects of the oscillator, both R_i and R_o should be kept significantly lower than R_x, and it is therefore beneficial to increase the value of g_{m1}. Employing very large W/L transistors is an attractive method for increasing g_{m1} without increasing power consumption, however any escalation in transistor aspect ratio in turn reduces the 3-dB bandwidth of the amplifier due to the increase in MOS parasitic capacitance. As a rule of thumb, the amplifier's bandwidth should be greater than 10× the oscillation frequency in order to keep the phase shift at this frequency as close to 0° as possible. Fortunately, implementing a design with a lower gain R_f will lead to an increase in the 3-dB bandwidth as outlined in the following section. Because R_f must be greater than R_x to sustain oscillation, shrinking R_x through scaling allows for lower allowable R_f implementations and enables designs with overall reduced power consumptions.

3.2.1 Low Power Design

The essential systemic consideration for nearly all real-time clock applications is power consumption. To that end, it is of upmost importance to unveil which designable parameters can lead to reduced power consumption and to predict a figure for the minimum possible power consumption, given ideal conditions.

3.2.1.1 Sustaining Amplifier Simulation parameters

In order to gain a quantitative feel for the sustaining amplifier circuit of Figure 3.7, it is instructive to simulate various amplifier parameters under specific conditions, assuming typical resonator and transistor values. The typical resonator and transistor values to be utilized in this section are reflected in Table 3.2 and Table 3.3 respectively.

Table 3.2: 32 kHz Capacitive-Comb Transduced Resonator Design Values

Parameter	Value	Units
f_0	32.0	kHz
Q	50000	–
V_P	1.65	V
H	2.77	nF/m
R_x	2.48	MΩ
C_x	39.9	aF
L_x	618	kH
C_o	8.41	fF

Table 3.3: Sustaining Amplifier Design Parameters

Parameter	Value	Units
V_{DD}	1.8	V
V_{ov}	100	mV
λ	0.1	V^{-1}
C_p	0.75	pF
R_F	5	MΩ

3.2.1.2 Design Analysis

The transimpedance amplifier of Figure 3.7 is best specified by its full transfer function

$$Z_{amp}(s) = -\frac{R_f a_v \omega_{in}\omega_{out}}{s^2 + (\omega_{in} + \omega_{out})s + \omega_{in}\omega_{out}(1 + a_v)} \quad (3.13)$$

where

$$\omega_{in} = \frac{1}{R_f C_{in}},\ \omega_{out} = \frac{1}{(R_f // r_{01} // r_{03}) C_{out}}$$
$$a_v = \frac{1}{2} g_{m1}(R_f // r_{01} // r_{03}) \quad (3.14)$$

and where a_v is the dc voltage gain of the base op amp, and C_{in} and C_{out} are the total capacitance at the input and output terminals of the amplifier, respectively. For simplicity, C_{in} and C_{out} can be expressed as

$$C_{in} = C_0 + C_{p,in} \quad (3.15)$$

$$C_{out} = C_0 + C_{p,out}$$

Where $C_{p,in}$ and $C_{p,out}$ represent the total parasitic capacitance at the input and output terminals including MOS parasitic capacitance and pad capacitance, while C_0 represents the resonator's static comb-finger capacitance given by equation (3.5).

Equation (3.13) has the form of a lowpass biquad transfer function. Figure 3.8 illustrates that for a given R_f value, 5 MΩ in this case, the sustaining amplifier's dc gain and 3-dB bandwidth decrease as transistor drain current decreases. This effect is also seen in the expression for dc gain $Z_{amp}(0)=R_{amp}$ given in (3.10), and the expression for effective bandwidth $\omega_{b,eff}$ given by

$$\omega_{b,eff} \cong [\omega_{in}\omega_{out}(1+a_v)]^{\frac{1}{2}} \cong \left[\frac{g_{m1}}{2R_f C_{in} C_{out}}\right]^{\frac{1}{2}} \tag{3.16}$$

As illustrated in Figure 3.8 and (3.13), any increase in R_f directly translates to an increase in the sustaining amplifier's gain. However, because the phase across the sustaining amplifier should be as close to 0° as possible for this topology, especially when combined with high Q resonators, R_f's effect on the amplifier's effective bandwidth must be considered. From (3.16), the bandwidth can be increased by decreasing R_f, C_{in}, and C_{out}. In order to meet Barkhausen's conditions for oscillation, the minimum R_f value is set by equation (3.9) and the bandwidth should be larger than the oscillation frequency and for best stability, the effective bandwidth should be chosen, as a rule of thumb, to be at least 10× greater than the oscillation frequency [56].

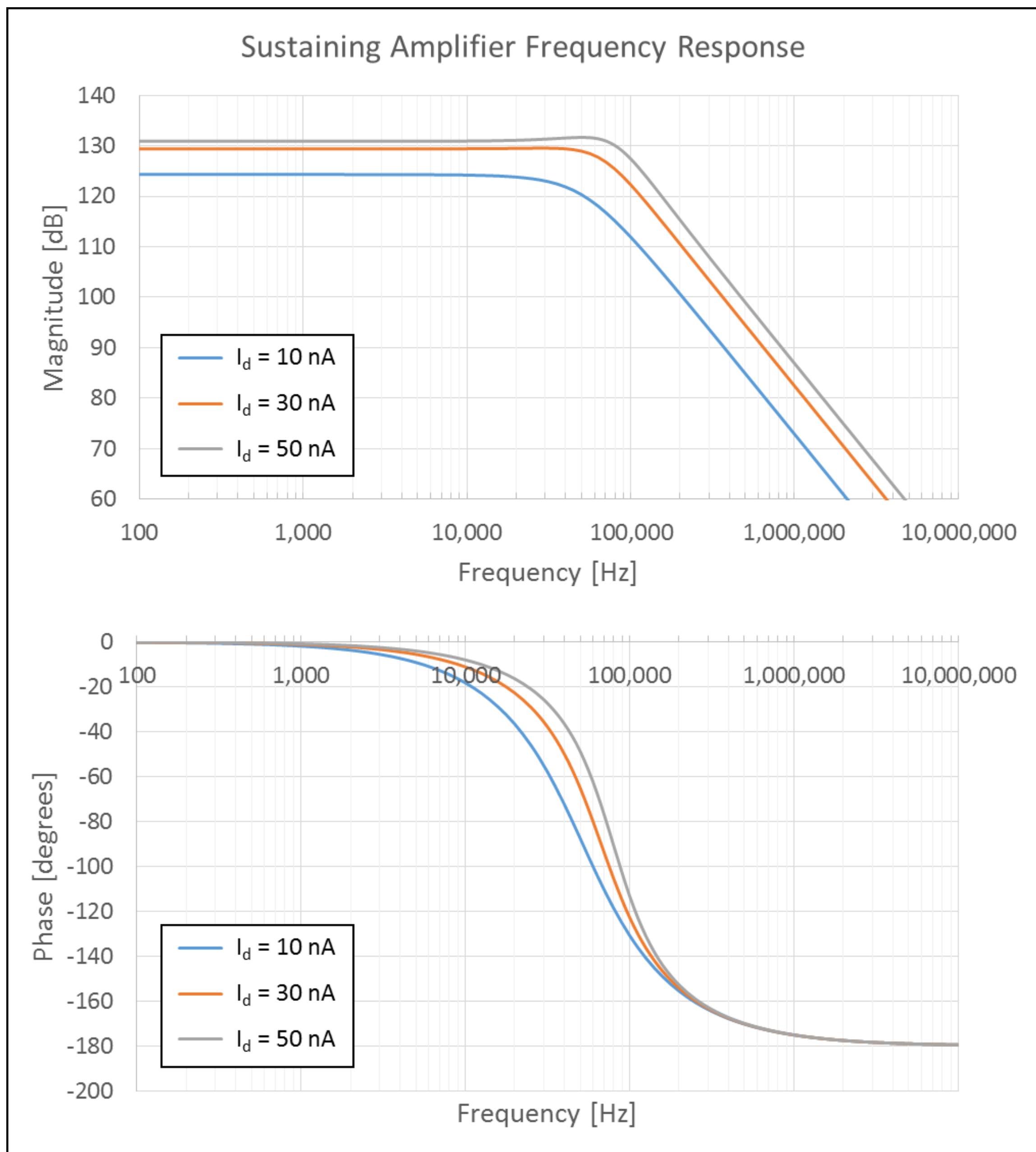

Figure 3.8: Simulated frequency response of the sustaining amplifier of Figure 3.7 with R_f held to 5MΩ and bond pad capacitances of 0.75 pF

Figure 3.9 plots the sustaining amplifier's bandwidth as a function of R_f. As shown, when R_f is increased, the sustaining amplifier's 3-dB bandwidth is diminished. In addition, it can be observed that for a fixed R_f value, the amplifier bandwidth decreases as transistor drain current is reduced. Therefore, if minimum current is desired, R_f should be set to the smallest value that still meets the criteria of equation (3.9).

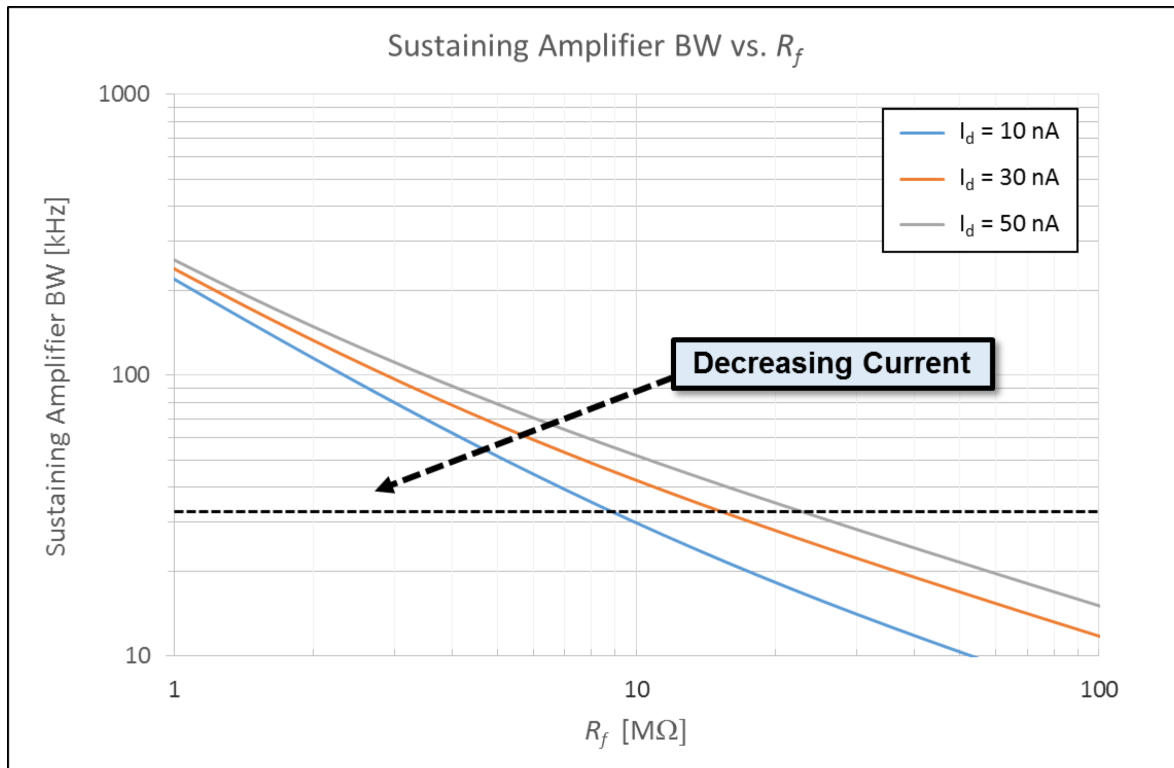

Figure 3.9: Bandwidth plotted against R_f for the sustaining amplifier of Figure 3.7 with bond pad capacitances of 0.75pF

As previously mentioned, the sustaining amplifier's bandwidth is typically set to be at least 10× the oscillation frequency as a rule of thumb. However, if minimal power consumption is of utmost concern, it is necessary to observe cases in which this rule is violated. Figure 3.10 presents a plot of the sustaining amplifier's gain and phase shift, at 32 kHz, as a function of R_f. Once again, it can be seen that as R_f is reduced the gain provided by the amplifier is also lessened. Perhaps more interestingly, reductions in transistor current also lead to reduced gain and increased phase shift across the amplifier. Provided the amplifier's gain is sufficiently large, oscillation is sustained at the frequency at which a 0° phase shift persists around the oscillator loop. This condition for oscillation implies that any phase shift present across the amplifier must be compensated by a corresponding phase shift across the resonator. Although this phase shift can be readily achieved by sustaining oscillation slightly off-resonance, the magnitude of impedance seen across a high-Q resonator rapidly increases as the operation frequency deviates from the resonator's natural frequency. This, in turn, requires additional sustaining amplifier gain to overcome the heightened resonator impedance. Therefore, it becomes unfavorable to sustain oscillation in a configuration requiring significant resonator phase compensation.

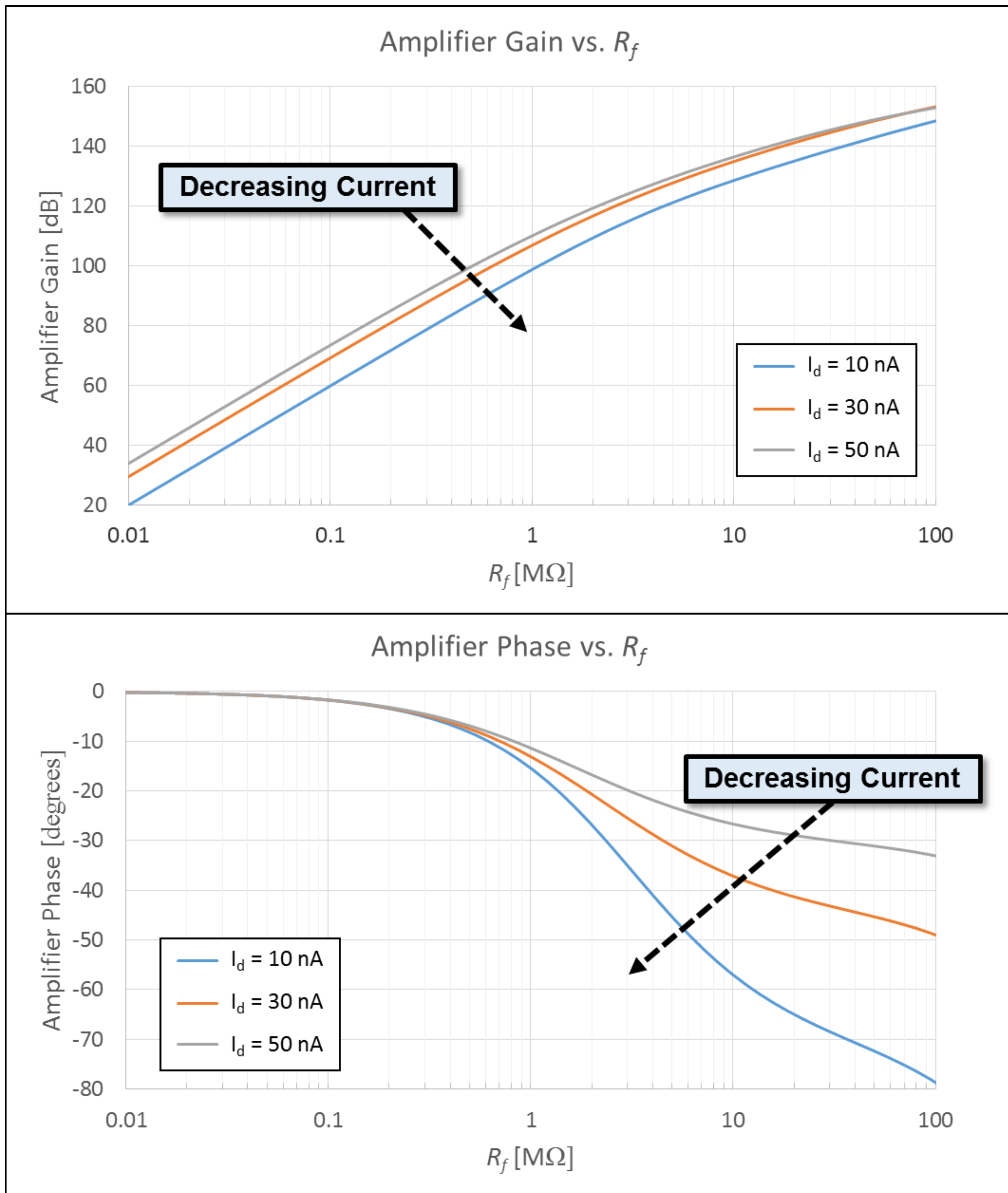

Figure 3.10: Simulated gain and phase shift at an operating frequency of 32 kHz plotted against R_f for the sustaining amplifier of Figure 3.7 with bond pad capacitances of 0.75pF

To determine just how small the value of the feedback resistor can be limited to, and in turn the minimum operating current, it is necessary to examine the full oscillator loop gain

expression incorporating resonator effects. As previously described in Section 2.3.2, the micromechanical resonator can be represented as an LCR tank with a complex impedance given by

$$\boldsymbol{Z_{res}(s) = sL_x + \frac{1}{sC_x} + R_x = s^2\omega_0^2 + sR_xC_x + 1} \tag{3.17}$$

Combining equation (3.13) and (3.17) yields the full transfer function representing the gain around the oscillator loop, which can be expressed as

$$\boldsymbol{H(s) = \frac{Z_{amp}(s)}{Z_{res}(s)}}$$
$$\boldsymbol{H(s) = \left(\frac{R_f a_v \omega_{in}\omega_{out}}{s^2 + (\omega_{in} + \omega_{out})s + \omega_{in}\omega_{out}(1 + a_v)}\right)\left(\frac{1}{s^2\omega_0^2 + sR_xC_x + 1}\right)} \tag{3.18}$$

Assuming the resonator and amplifier design parameters summarized in Table 3.2 and Table 3.3 respectively, the magnitude and phase around the oscillator loop, whose transfer function is summarized in equation (3.18), is plotted in Figure 3.11. Oscillation will be sustained if the closed loop magnitude is greater than 0 dB at the frequency where the phase around the oscillator loop crosses 0º. Here three transistor drain current cases are considered. Under the condition that the amplifier drain current is operated at 10 nA, oscillation is not sustained because the closed loop gain never exceeds 0 dB. On the other hand, oscillation will be sustained under both the 30 nA and 50 nA drain current conditions because at the frequency in which the phase shift is 0º, the magnitude of the loop gain exceeds unity. Therefore it can be surmised that for this particular oscillator design, the minimum transistor current consumption will fall somewhere between 10 nA and 30 nA. Indeed, as depicted in the simulation of Figure 3.12, the minimum drain current required for sustained oscillation is 20.9 nA. This is because at the frequency in which the phase around the loop is equal to 0°, the closed loop magnitude is exactly equal to unity (0 dB).

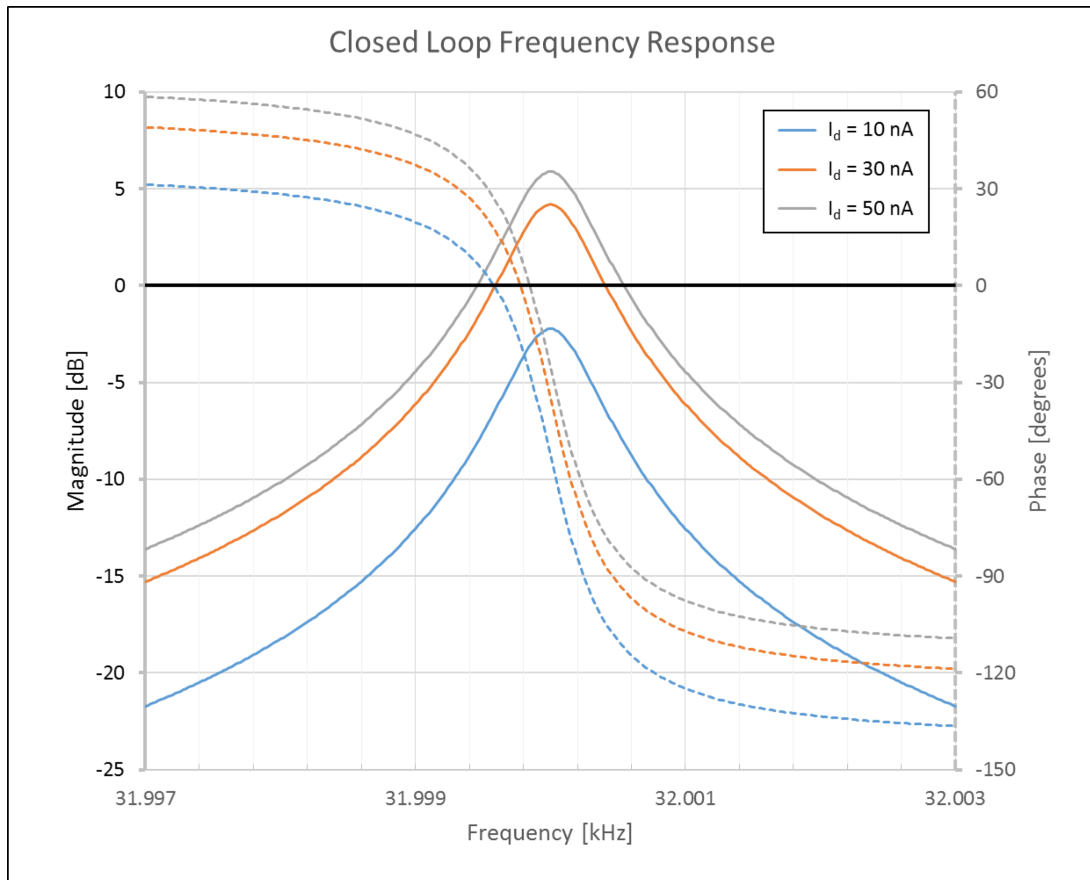

Figure 3.11: Closed loop frequency response for various amplifier drain currents assuming the resonator and sustaining amplifier conditions outlined in Table 3.2 and Table 3.3 respectively

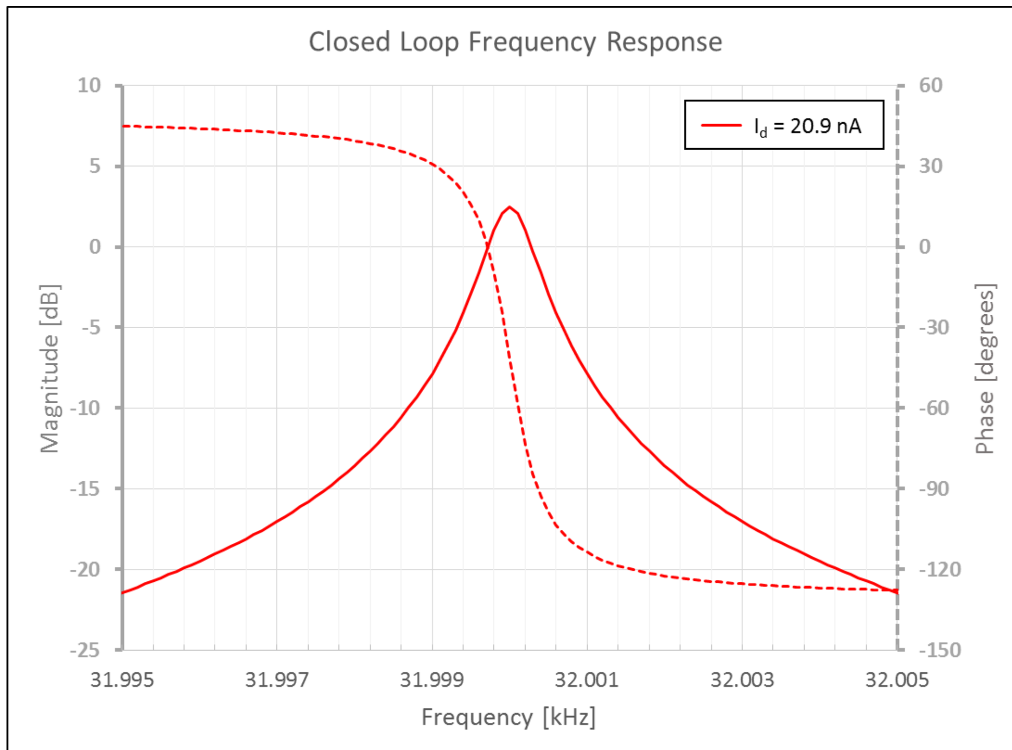

Figure 3.12: Closed loop frequency response with the minimum drain current required for sustained oscillation

Following the same procedure that was used to determine the minimum current consumption required for sustained oscillation in Figure 3.12, the minimum oscillator power consumption is computed under a range of conditions in order to better establish relationships between design parameters and device power. Figure 3.13 presents a plot the minimum sustaining amplifier power consumption as a function of resonator motional impedance R_x. In addition, the total input and output parasitic capacitance C_p is varied. Here, it becomes immediately apparent that if minimal power consumption is desired, attention must be paid toward reducing both motional impedance and unwanted capacitances. As previously discussed in Section 3.1.1, reductions in motional impedance can be achieved by laterally scaling the comb-finger gap. This effect is applied to produce the plot of Figure 3.14. From this plot, it can be observed that lateral gap scaling can indeed result in significant reductions in oscillator power consumption.

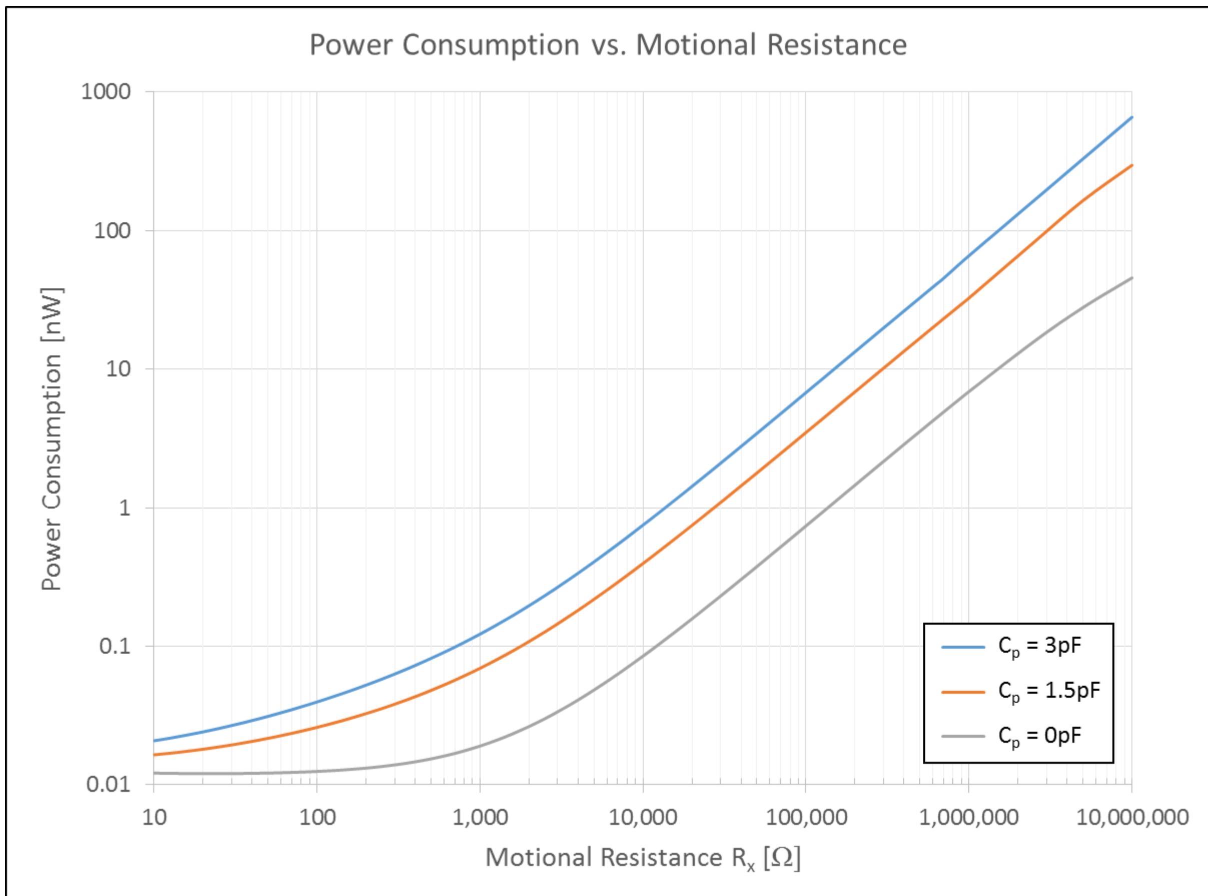

Figure 3.13: Minimum sustaining amplifier power consumption plotted against resonator motional resistance under various parasitic capacitance conditions

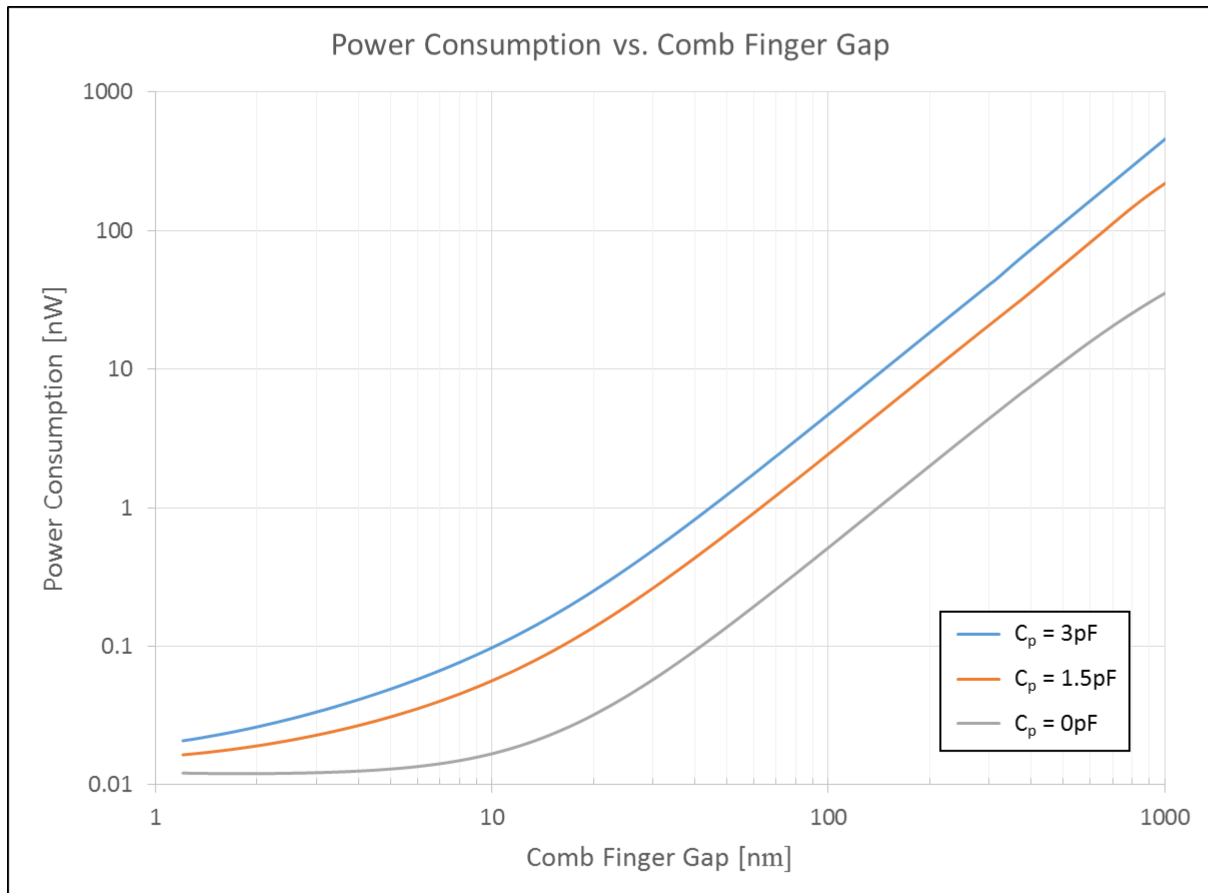

Figure 3.14: Minimum sustaining amplifier power consumption required to sustain oscillation plotted against comb finger gap spacing for various parasitic capacitance conditions

3.3 Experimental Results

In order to confirm the designs of Sections 3.1 and 3.2, resonators were fabricated in the Berkeley Marvell Nanolab following the procedure outlined in Section 2.5. Figure 3.15 presents the frequency characteristic of the device of Figure 2.12 operating under 10 μTorr pressure in a Lakeshore FWPX Vacuum Probe Station and measured utilizing a 1 MΩ op-amp-based transresistance amplifier into an HP8751A network analyzer. With an applied dc-bias voltage of only 1.65V, the resonator exhibited a motional resistance R_x of 1.94 MΩ, well within the range needed to meet the requirements of the CMOS sustaining amplifier. From (3.8), it should be noted that while the resonator's high Q value of 57,000 certainly contributed to the modest R_x value, the resonator's notably small capacitive-comb gaps g_0 of 550 nm were much more responsible for keeping R_x small.

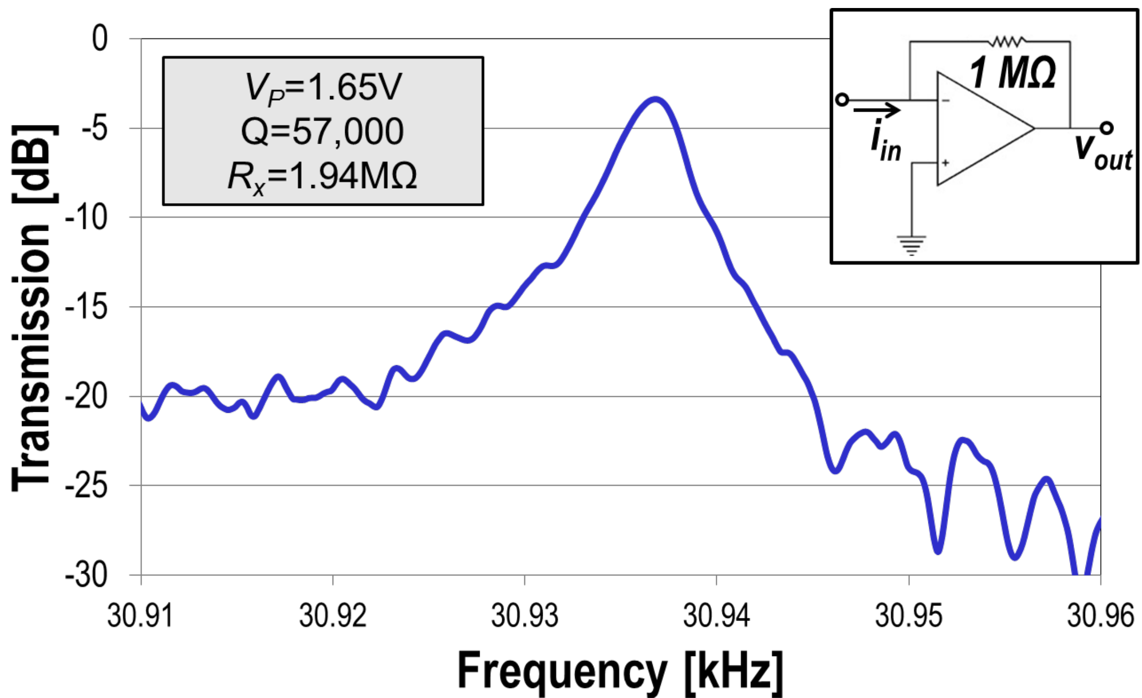

Figure 3.15: Measured frequency characteristic for the Figure 2.12 device under 10 µTorr vacuum.

The custom ASIC CMOS sustaining amplifier of Figure 3.7 was fabricated in a 0.35 µm foundry process. As depicted in Figure 3.16, the oscillator circuit combines the MEMS resonator and sustaining amplifier dies via bond-wires. The oscillator was then placed into a custom-designed vacuum box equipped with feedthroughs for electrical connection to outside measurement instrumentation. Oscillation starts up immediately on application of the necessary voltages outlined in Table 3.4. As seen in Figure 3.17, the oscillator produces a clean sinusoidal time-domain signal with a frequency of precisely 32.768 kHz. Note that this exact frequency did not come about via strict process control in fabrication, but rather from application of 2.95 V to the resonator's tuning-electrodes, which provided the necessary frequency correction. In fact, the measured tuning range of 50,000 ppm over a V_{tune} range of 3.3 V is 5× greater than the measured device-to-device frequency variance of 10,000 ppm, confirming the efficacy of the design described in Section 3.1.2.

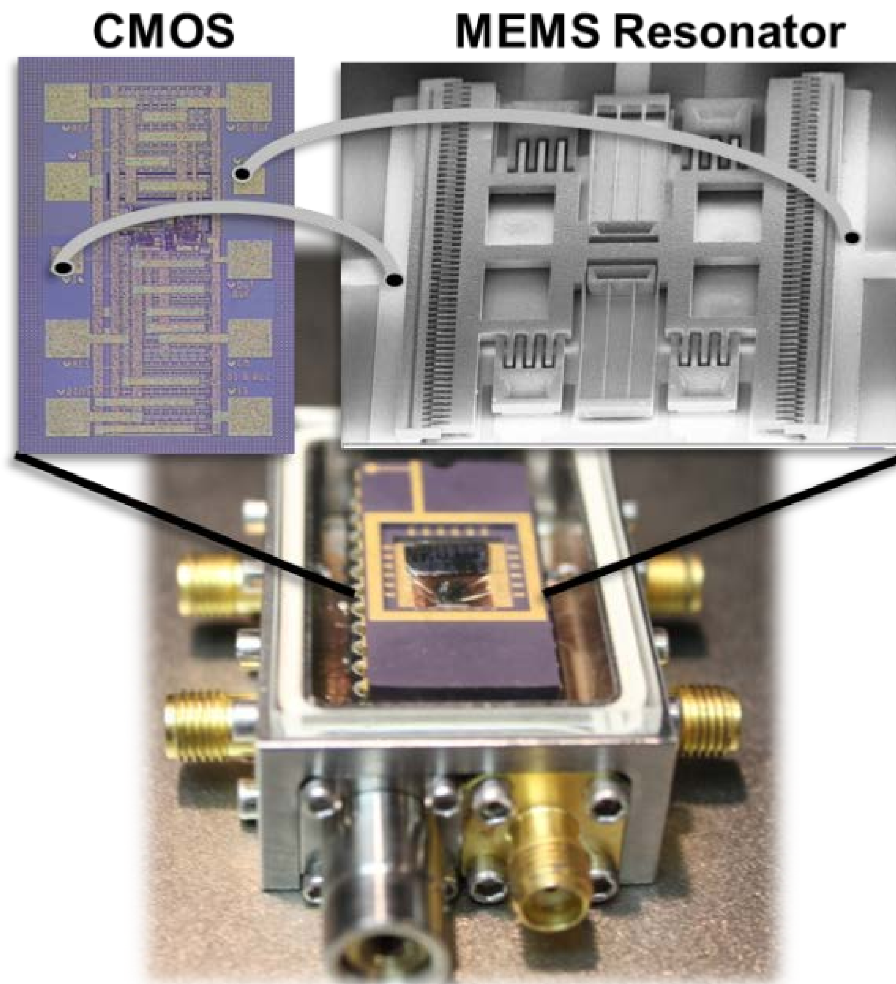

Figure 3.16: Photo of the custom vacuum box test apparatus, with a blow up of a mock oscillator schematic combining the SEM of the micromechanical resonator with a die photo of the custom-designed ASIC amplifier.

As seen in Table 3.4, sustained oscillation did not call for the application of any voltages above the CMOS technology's design rail of 3.3 V. Furthermore, with the transistors forced into weak inversion by lowering the supply-rail to 1.8 V, the oscillator consumed only 2.1 μW of power, which is on par with the power consumptions of nearly all commercially available compact-footprint clock oscillators.

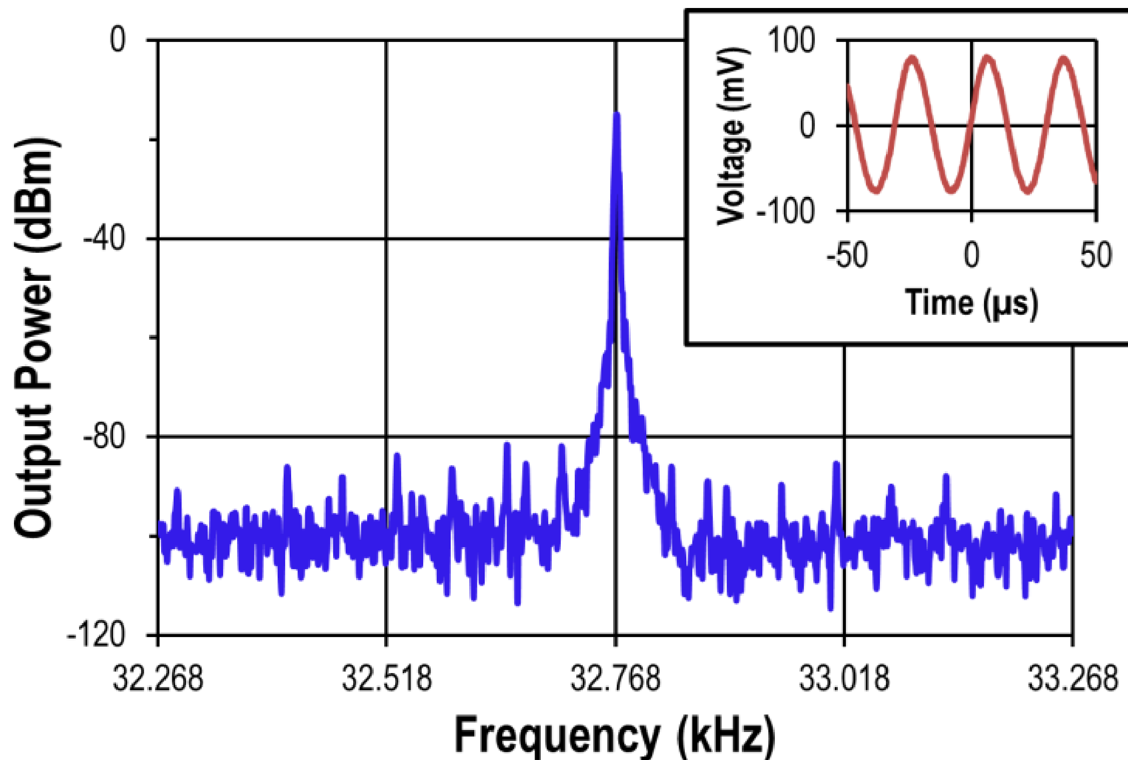

Figure 3.17: Measured oscillator output spectrum and time-domain waveform.

The clock oscillator of this work compares favorably to previously demonstrated clock oscillators in terms of both size and power consumption Table 3.5 and Figure 3.18 compare the oscillator and resonator of this work with previously demonstrated 32-kHz oscillators and resonators, respectively. The size comparison illustrated in Table 3.5 references all MEMS-die footprints to the package size of the smallest commercially available quartz clock oscillator [57], where the larger the scale factor, the smaller the die footprint. From Table 3.5, it can be seen that the oscillator of this work is 311× smaller than its quartz-crystal counterpart and significantly smaller than previously demonstrated MEMS approaches [13], [58]. The device of this work also offers a considerably larger tuning range than the recently demonstrated piezoelectric based approach [13], and consumes less power than the smallest commercially available 32-kHz quartz-based product. Given the favorable scaling attributes for capacitive-transduced resonators, highlighted in Section 3.1.1, even more reductions in size and power consumption should be possible as better lithography becomes available.

Table 3.4: Oscillator Bias and Results Summary

Resonator Bias V_P	**1.65V**
Supply Voltage V_{DD}	1.80V
Tuning Voltage V_{tune}	2.95V
Oscillation Amplitude	87.61mV$_{RMS}$
Power Consumption	2.1 µW

Table 3.5: Oscillator Comparison

Device	**SG-3030CM** [61]	**SiT1552, Asl et. al** [23][62]	**Cioffi & Hsu** [58]	**Serrano et. al** [13]	**This Work**
Type	Quartz	Capacitive MEMS	Capacitive MEMS	Piezoelectric MEMS	Capacitive MEMS
Area	3200 ×1500µm	1500 ×800µm	~500µm ×400µm	250µm ×250µm	140µm ×110µm
Scale Factor	1	4	24	76.8	311
V_P	N/A	3.6	2.5V	N/A	1.65V
Q	N/A	52,000	60,000	5,000	57,000
Tuning Range	N/A	N/A	N/A	6,500 ppm over 6V	50,000 ppm over 3.3V
Power	2.0µW	1.0µW	1.0µW	N/A	2.1µW

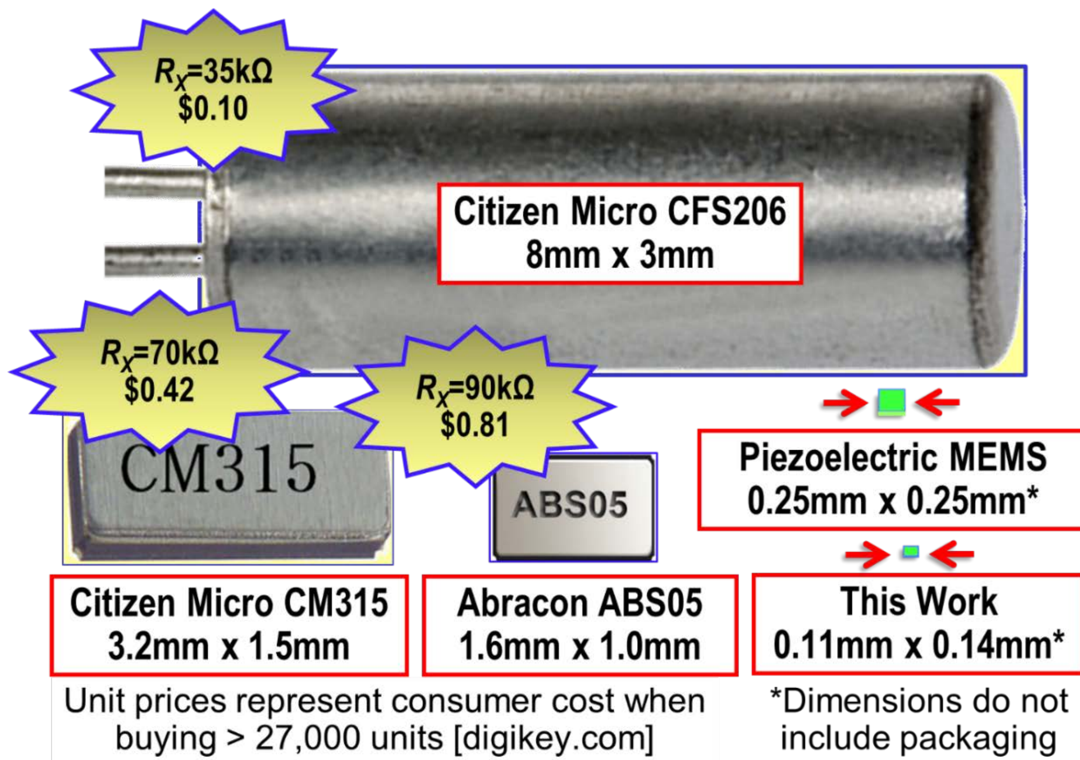

Figure 3.18: Size comparison of the resonating element of this work against previously demonstrated miniature clock resonators [18][19][20][13]

3.4 Conclusions

A 32.768-kHz clock oscillator employing an ultra-compact tunable capacitive-comb transduced MEMS-based resonator as its frequency-setting element has been demonstrated with all applied dc-bias voltages < 3 V while consuming only 2.1 μW of power. The resonator design possesses beneficial scaling properties, whereby scaling-down all lateral dimensions results in square-law reductions in both motional resistance and die footprint.

Because of this extensive scaling potential, capacitive-transduced MEMS resonators seem well positioned to provide the smallest real-time clock oscillators provided that the repeatability issues associated with scaling can be mitigated. While the frequency tuning-electrodes in this work provide an effective solution for alleviating center frequency variations exacerbated by aggressive scaling, there is some concern that the large tuning range can give rise to instability if the variables controlling the tuning are themselves not sufficiently stable. For this reason, design improvements that reduce device-to-device mismatch are always desirable and are the subject of future work.

4. High-Order Micromechanical Filters

This chapter presents the mechanical coupling of several resonators following the topology guidelines laid out in Chapter 2 to realize a high-order, narrowband MEMS-based filter. After a brief discussion detailing relevant filter performance metrics, coupled resonator filter operation and design is explored with special emphasis paid to designs comprising more than three resonators, such as the design show schematically in Figure 4.1. Next, an automated passband correction protocol is presented and applied to the voltage-controlled tuning electrodes of Section 2.2.1.1. The chapter concludes with measurement results highlighting the efficacy of the tuning protocol.

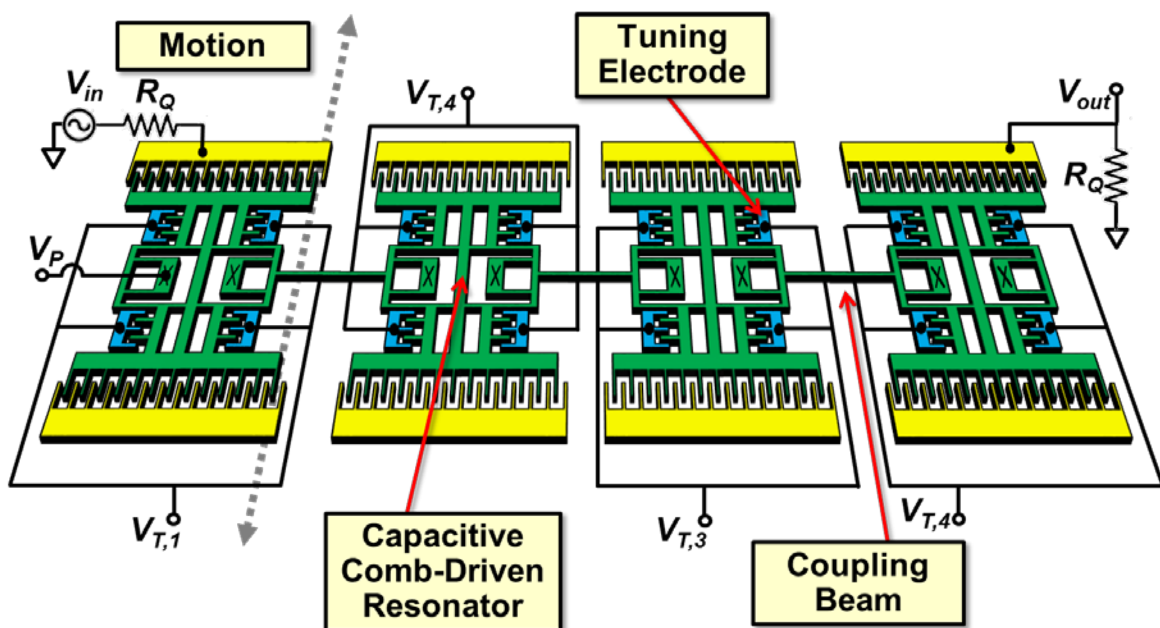

Figure 4.1: Top-view schematic of the 8-pole micromechanical filter in a single-ended drive and sense configuration and equipped with frequency tuning electrodes to allow for passband correction using an automated tuning protocol.

4.1 Filter Performance Metrics

To set the stage for the discussion of micromechanical filters, it is helpful to outline some of the important bandpass filter performance metrics. Figure 4.2 presents the simulated frequency spectrum of a 455-kHz micromechanical filter comprised of four coupled resonators with notable performance metrics overlaid. For communication applications the shape factor should be kept small (as close to unity as possible), the insertion loss should be minimized (typically less than 1 dB), and by design, passband ripple is often held under 1 dB [59]. In order to satisfy the demands of modern communication systems, multiple resonator tanks coupled in a ladder configuration are required [39].

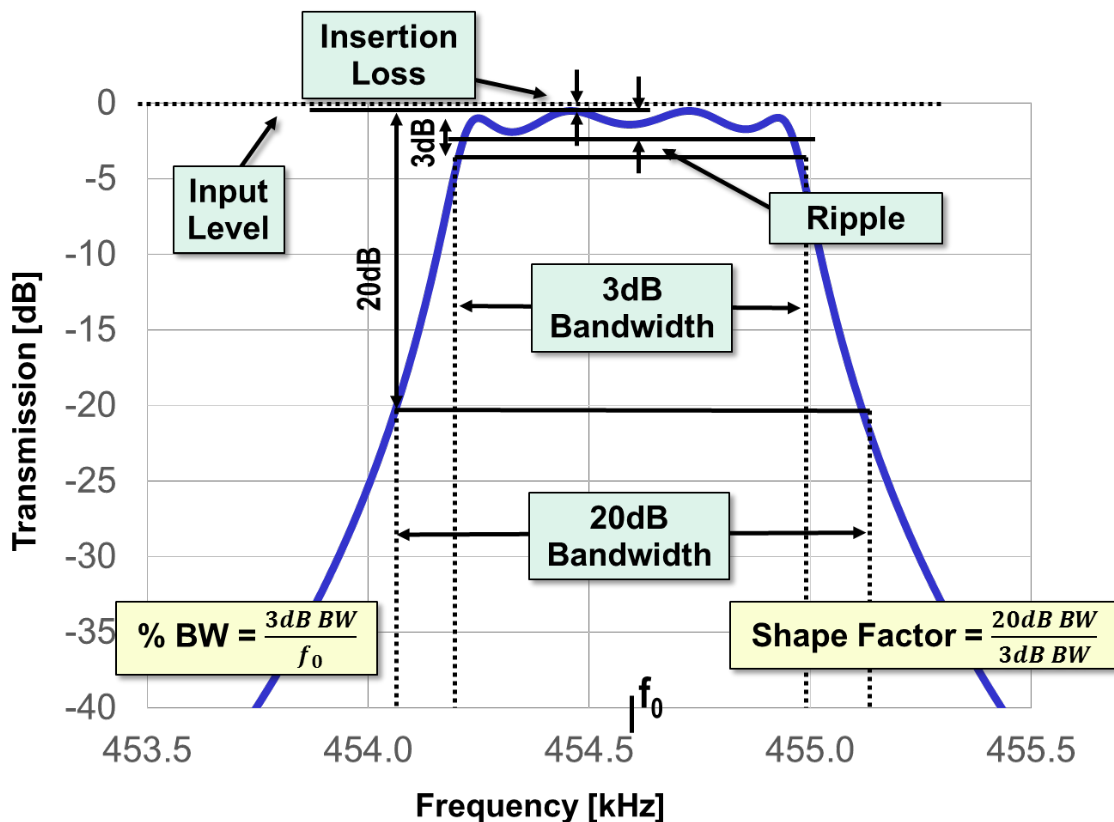

Figure 4.2: Sample bandpass filter spectrum with important performance metrics highlighted.

When discussing coupled resonator filters, the filter order is typically described as being equal to the number of resonators used in the network, and this convention will be used throughout this chapter. As illustrated in Figure 4.3, as more resonators are coupled and the filter order increases, the shape factor of filter tends to decrease. In general, better selectivity can be achieved by utilizing more resonators; however, this comes at the cost of increased size, tuning complexity, and in some cases insertion loss [47].

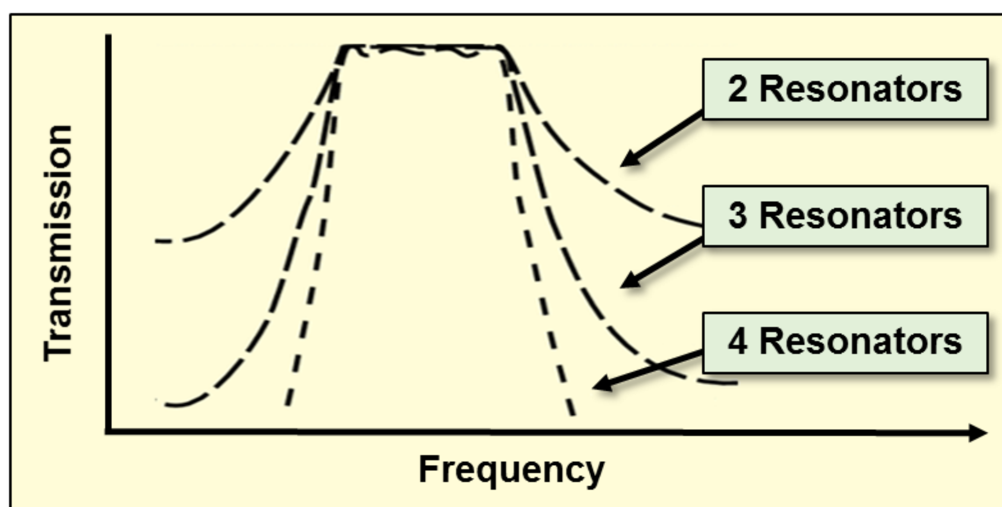

Figure 4.3: Filter Spectrum illustration highlighting the improvement in shape factor as the number of coupled resonator filters is increased.

4.2 Coupled Resonator Filter Operation

Before detailing the tuning protocol, it is instructive to first review the structure and operation of the filter-to-be-tuned, shown in top-view in Figure 4.1. Here, the demonstrated filter is similar to that of [1] in its use of capacitive comb-driven ratioed-folded-beam resonators coupled at low-velocity locations via flexural mode beams. In the preferred operation scheme, the combination of a dc-bias voltage V_P and AC input voltage v_i applied through a proper termination resistance across the electrode-to-resonator comb of the left-hand-side end resonator generates a force at the frequency of v_i amplified by the magnitude of V_P. This force, in turn, produces an input vibration (i.e., a mechanical signal) on the left-hand-side resonator that traverses the filter transfer function, being shaped in the process into a corresponding output vibration at the right-hand-side end resonator. Vibration of the right-hand-side end resonator effectively realizes a dc-biased time-varying capacitor that converts the mechanical velocity signal to an electrical output current $i_o = V_P(dC/dt)$. This current feeds into the output load, generating a corresponding voltage output. In effect, this filter takes an input voltage, converts it to a mechanical signal, processes the signal in the mechanical domain, then converts the signal back to an electrical signal to be forwarded to the next block in the system.

Reference [12] already presents a full description of the design and modelling of this type of filter, so rather than cover all of the fine design details, this chapter primarily focuses on filter passband correction via tuning of each constituent resonator. In particular, in this design the resonance frequency of each constituent resonator is tunable via voltage-controlled electrical springs [30] generated by the parallel-plate electrodes indicated in the zoom-in of Figure 4.4, which presents the perspective-view schematic of one of the constituent resonators. The overall filter described here uses more resonators than that of [12], so it achieves a better shape factor. From a simplistic perspective, the first four lateral vibration modes of this 4-resonator system, shown in Figure 4.6, generate the 4th order, 8-pole passband shown. To flatten

the mode peaks of Figure 4.6 into the more familiar flat passband normally seen (*cf.* Figure 4.2)) termination impedances R_Q, shown in Figure 4.1, are incorporated into the test circuit.

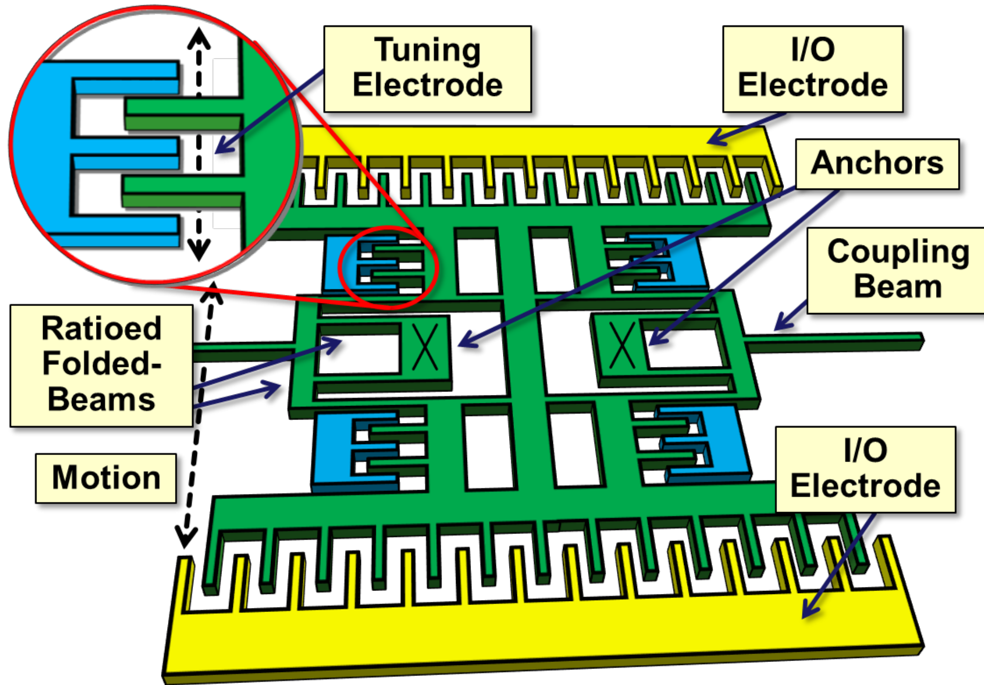

Figure 4.4: Perspective-view illustration showing details of the capacitive comb-driven folded-beam resonator used in the multi-resonator filter.

4.2.1 Simplified Design Procedure

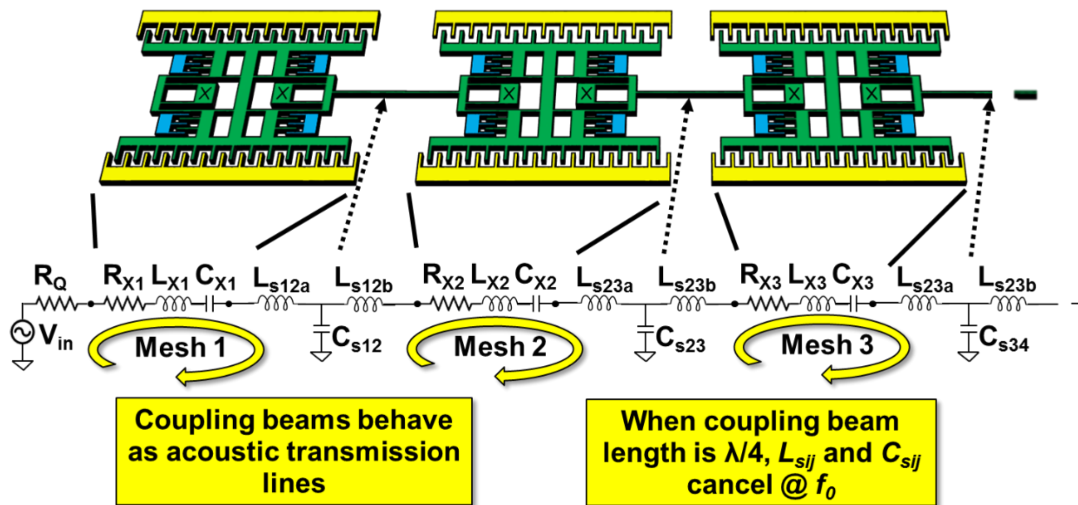

Figure 4.5: Perspective-view and equivalent circuit of a section of three coupled resonators in a micromechanical filter configuration.

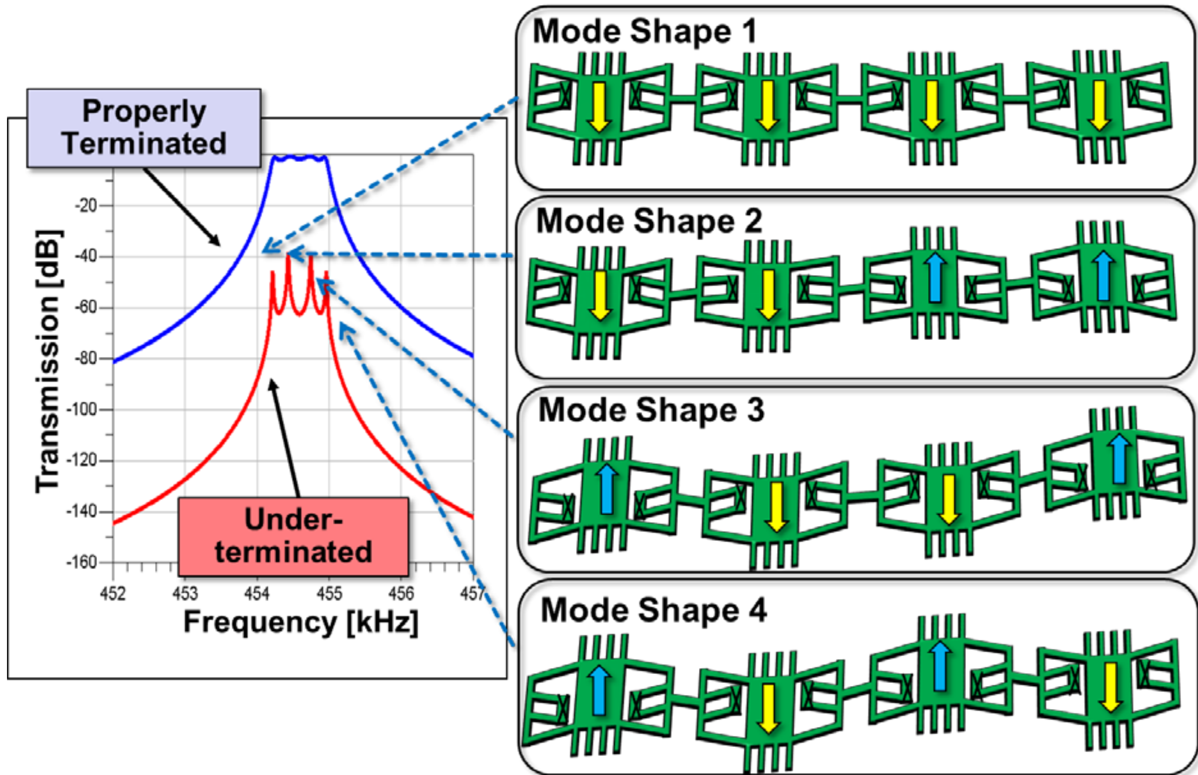

Figure 4.6: Simulated terminated and unterminated four-resonator filter passband alongside the system's vibrational mode shapes.

All resonators in Figure 4.1 are designed to have identical stand-alone frequencies, as emphasized in Figure 4.5, while the springs that couple them serve to split their frequencies apart to form the multiple-mode passband. Figure 4.6 illustrates the four distinct resonant mode shapes present in a 4th order filter. As shown, the lowest frequency mode occurs when all four resonators vibrate in phase, and the highest frequency mode occurs when each coupled resonator vibrates 180° out of phase with respect to its neighboring resonator. The frequency placements of these vibration peaks is determined by the stiffnesses of the coupling beams k_{sij}, as dictated from beam theory, and their constituent resonators at the coupling location k_r. For a filter with a bandwidth BW and center frequency f_0, the following expression must be satisfied

$$BW = \left(\frac{f_0}{kij}\right)\left(\frac{k_{sij}}{k_{rc}}\right) \tag{4.1}$$

where k_{ij} represents the normalized coupling coefficient as specified by a filter cookbook [39]. As seen in equation (4.1), the filter bandwidth is not a function of absolute resonator and coupling beam stiffnesses, but rather their ratio k_{sij}/k_{rc}. This allows for the general design

procedure of reference [12], summarized as follows:

1) Fix coupling beam widths to the minimum value as dictated by lithographic resolution;

2) Set all coupling beam lengths to the effective quarter-waveflength of the filter's center frequency, and evalute the correseponding coupling beam stiffness k_{ij};

3) Design all resonators to have the same resonant frequency, while simultaneously presenting the necessary stiffness at the coupling locations k_{rc} as dictated by equation (4.1);

4) Terminate and tune the filter as needed.

Note that in the above procedure, the stiffnesses presented at coupling locations are modified to satisfy the demands outlined by the normalized filter coupling coefficients. In the filter topology depicted in Figure 4.1, the resonators are coupled at the truss, so there exists a demand on the individual resonator topology to have a designable truss stiffness. Unfortunately, this is not the case for generalized resonator topology outlined in Chapter 2, however full control over truss stiffness can be achieved by introducing the concept of ratioed folded beams.

4.2.2 Ratioed Folded-Beams

As depicted in Figure 4.7, the folded-beams of the comb driven resonator can be designed in a way such that the lengths of the inner and outer beams, denoted by L_{bi} and L_{bo} respectively, are not necessarily the same. With the addition of differing beam lengths to the topology design, the stiffness at the resonator truss k_{rc} can be specified as [12]:

$$\boldsymbol{k_{rc} = 4Eh(1+\beta^3)\left(\frac{W}{L_{bi}}\right)^3} \tag{4.2}$$

where E is Young's modulus; h is the resonator thickness and β is the ratio of the folded-beam lengths given by

$$\boldsymbol{\beta = \frac{L_{b0}}{L_{bi}}} \tag{4.3}$$

the expression for resonance frequency can also be modified to incorporate ratioed beams. The resultant expression as derived in [12] is given by

$$\boldsymbol{\omega_0 = \sqrt{\frac{4Eh\left(\frac{W}{L_{bi}}\right)^3}{(1+\beta^3)m_r}}} \tag{4.4}$$

Where m_r is the effective mass of the resonator given by equation (2.20). The utilization of equations (4.2) and (4.4) now allow for a resonator topology that presents a designable truss stiffness for a given resonator frequency, enabling the use of the simplified design procedure as described in section 4.2.1.

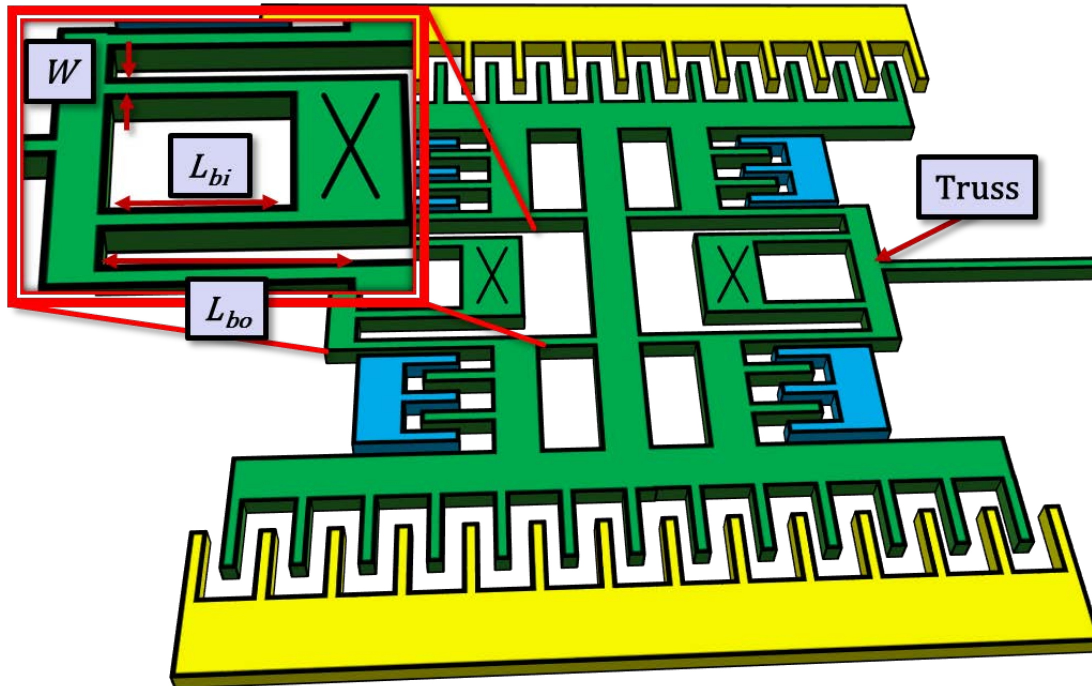

Figure 4.7: Perspective-view of a single resonator highlighting its ratioed folded-beams.

4.2.3 Resonator Asymmetry

For coupled resonator filters designed in the Chebyshev or Butterworth families, the normalized coupling coefficients are specified to be unique at the various coupling locations throughout the resonator. This, in turn, requires individual resonators to present a different stiffness to the coupling beams connected to its trusses. This is accomplished through an asymmetric resonator design in which the folded beam ratio is not consistent within the resonator. This effect is depicted by the mask layout of a single resonator making up a section of a 4th order filter, shown in Figure 4.8. Here the top section has a β value of 1.54, while the bottom section has a β of 1.63. In order to balance the lateral motion of the resonator, the effective truss masses were compensated (the lower truss was made wider in this case) such that the total effective truss and beam masses presented from the anchor points to the shuttle is identical from top to bottom.

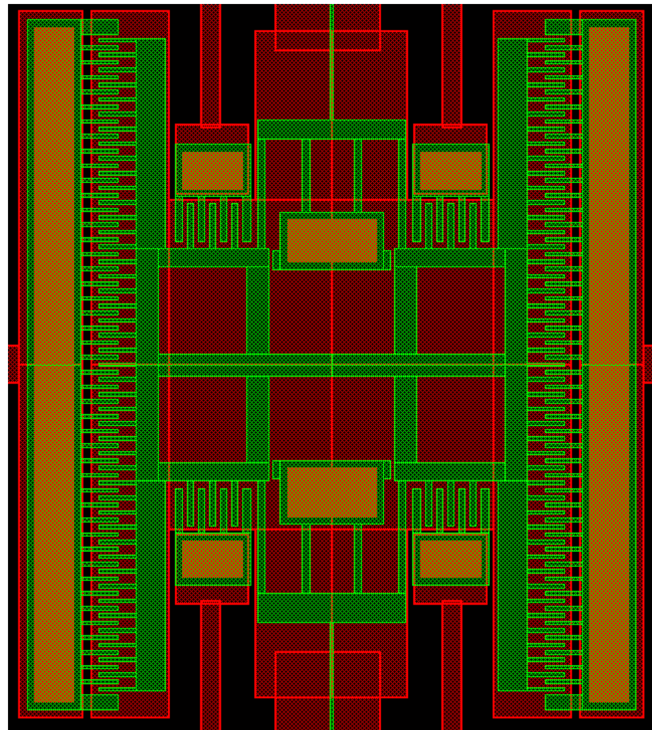

Figure 4.8: Mask layout of a single coupled resonator. The lower truss is designed to more mass to compensate for the necessary asymmetric ratioed folded beams.

4.2.4 Fourth Order Filter Layout

With the design procedure summarized in Section 4.2.1 and the considerations of Section 4.2.3, mask layout was generated for the fabrication process flow of Section 2.5. The mask layout for the 4th order filter to be highlighted in the remainder of this Chapter is shown in Figure 4.9.

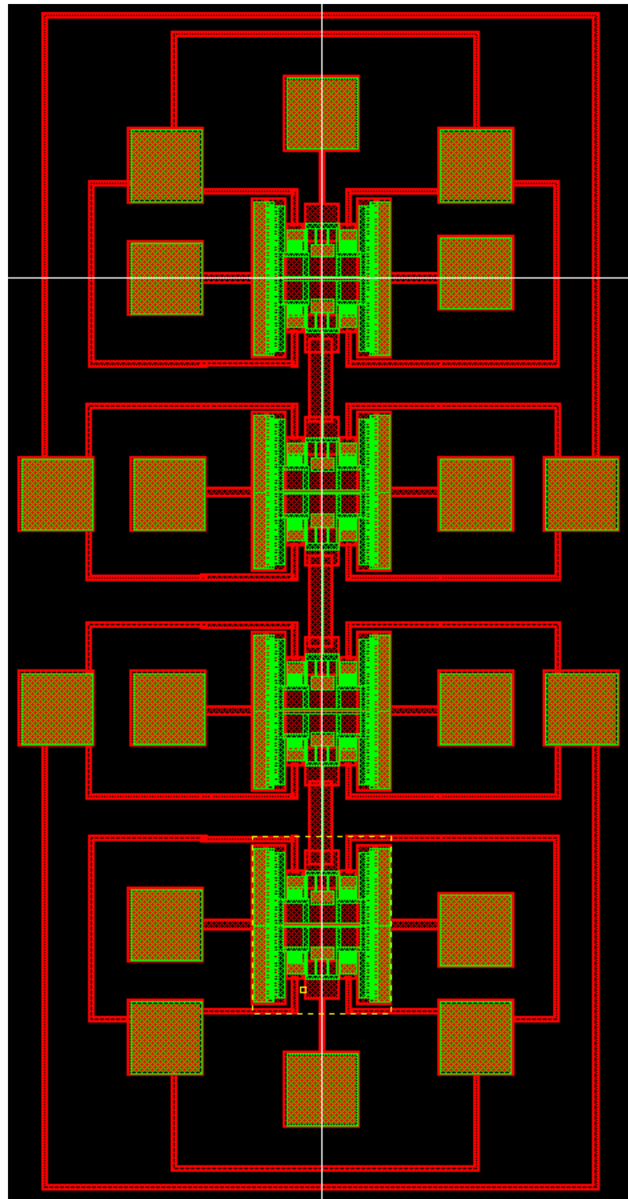

Figure 4.9: Mask layout of a micromechanical filter comprised of four coupled resonators

4.3 Filter Passband Correction

It is important to note that the better matched the resonator frequencies, the more correct the passband. On the other hand, the smaller the bandwidth of the filter, the higher the degree of resonator matching needed to avoid passband distortion.

Figure 4.10 illustrates how a wide 3% bandwidth filter response is relatively immune to resonator mismatches on the order of 1000 ppm, but the passband of a small 0.1% percent bandwidth filter is quite sensitive to even small mismatches down to 250 ppm, which is on the order of what is measured for disk resonators fabricated in a university microfabrication

laboratory [33]. Clearly, the 0.1% bandwidth filters demanded by RF channel-selection require matching better than so far demonstrated in fabrication, i.e., matching that would be difficult to achieve without trimming or tuning.

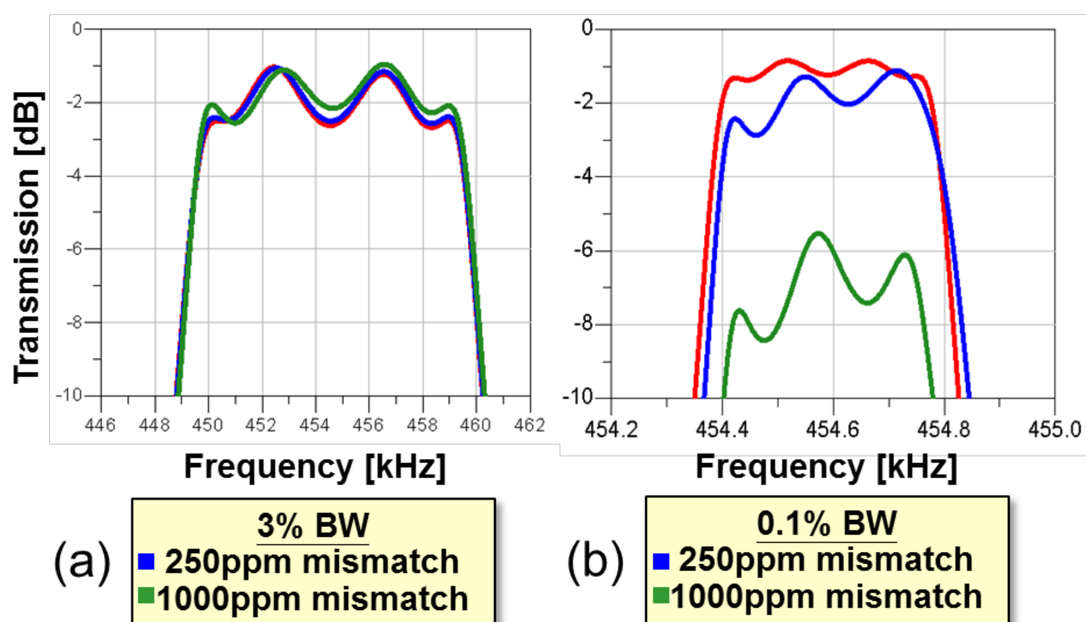

Figure 4.10: Simulations illustrating the effects of mismatching of a single resonator in a 4-resonator filter with percent-bandwidths of (a) 3% and (b) 0.1%. Here, the passband distorting effect of frequency mismatch is much larger for smaller percent-bandwidth.

4.3.1 Tuning Protocol

If tuning is required, then arguably voltage-controlled tuning is most desired, since it is more convenient than laser trimming or other methods, and it can be done in real-time, anytime. The tuning process should also be fast and efficient, and if possible, automated. Indeed, although "eye-balling" the spectrum on a network analyzer while hand-tuning was sufficient for the 2nd and 3rd order filters of [12], such a procedure is not desirable for higher order ones, especially if needed in high volume production. Rather, an iterative, easily programmable, automated tuning methodology is desired.

The automated tuning protocol used here seeks to maximize the energy in the filter response by maximizing the integrated area under the response spectrum. Specifically, the protocol for tuning is as follows:

1) Apply a white input signal, i.e., with constant power density at all frequencies around the passband, to the filter input and measure the total energy passed. This energy will be the total integrated energy under the filter frequency response spectrum.

2) Increment a single resonator's tuning voltage $V_{T,i}$ by a small amount in one direction, then measure the total integrated energy under the frequency characteristic.

3) If the energy decreased, then change the direction of the next increment for that same resonator. If it increased, then make the next increment in the same direction.

4) Continue adjusting $V_{T,i}$ and measuring energy output in steps until the energy output is maximized. At this point, the (integrated) area under the frequency characteristic is maximized.

5) Repeat steps 2 through 4 for each tuning voltage on each resonator and iterate the entire process as needed.

The above procedure assumes a convenient method for measuring the energy output, which can be done easily using diode-based circuitry. Alternatively, for the purposes of studying the progression of this tuning approach with the number of tuning increments, a network analyzer might be used to plot out and track the filter frequency characteristic while also integrating the total area under the curve to determine the direction of next tune. This, in fact, is what is done to verify this approach in Section 4.4.

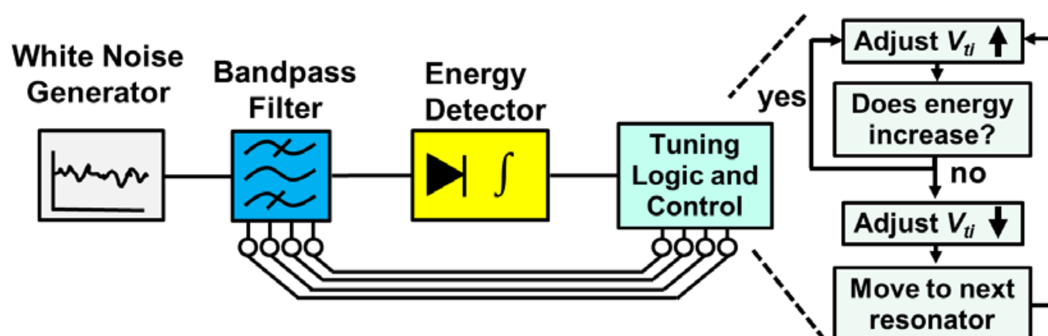

Figure 4.11: Block diagram of the proposed tuning protocol

4.3.2 Rationale Behind the Protocol

That the area under the frequency characteristic is maximized when the filter response is as designed is simply a consequence of the filter design procedure. After all, minimizing passband loss, i.e., maximizing passband energy, is one of the aims of filter design. That mere tuning of the constituent resonator frequencies can effectively correct the passband of a filter follows readily from mesh analysis of the filter's lumped equivalent circuit model shown in Figure 4.12. Here the use of $\lambda/4$ coupling beams, as prescribed in [39], cancels the reactance of the coupling links to either side of a given resonator mesh, leaving only the effective *LCR* of the resonator itself in any given mesh. Since each such mesh must resonate at the geometric center frequency of the filter, this means that the core resonator in a mesh, i.e., the comb-transduced folded-beam resonator itself, must resonate at this frequency. Thus, tuning each of the resonators making up a filter so that all resonate at its geometric center frequency will correct a misshapen passband.

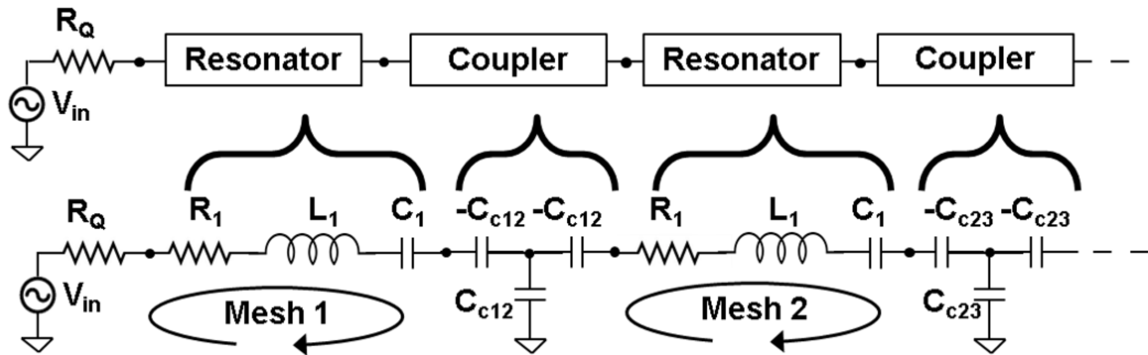

Figure 4.12: Equivalent lumped element model for an *n*-th order coupled resonator filter indicating the meshes that must resonate at the geometric center frequency.

If the tuning protocol, however, required that individual resonator resonances be measured, this would make for a tedious tuning procedure. Fortunately, one need not monitor each resonator's frequency; rather, only the total energy passed by the filter with a white input signal need be measured—something easily done using a diode-based energy detection circuit. This works, since again, the area under the frequency characteristic is maximized when all meshes resonate at the geometric center frequency of the filter.

That a given tune step is in the right direction if it increases the filter output response to a white input obviously also follows from the above arguments. To further illustrate, Figure 4.13, demonstrates the simulated effect on filter spectrum as a single resonator's resonance frequency is adjusted. By observing the filter spectrum as a frequency deviation is incurred, it becomes apparent that the integrated energy under the spectrum is maximised under the condition of perfect resonator-to-resonator frequency matching. Figure 4.14 presents a plot of integrated energy passed by a 4-resonator Chebyshev filter as a function of the frequency deviation of one mismatched resonator from the filter's geometric center frequency, with all other resonators matched correctly. Here, the energy curve peaks only when the resonator's frequency matches the geometric center frequency.

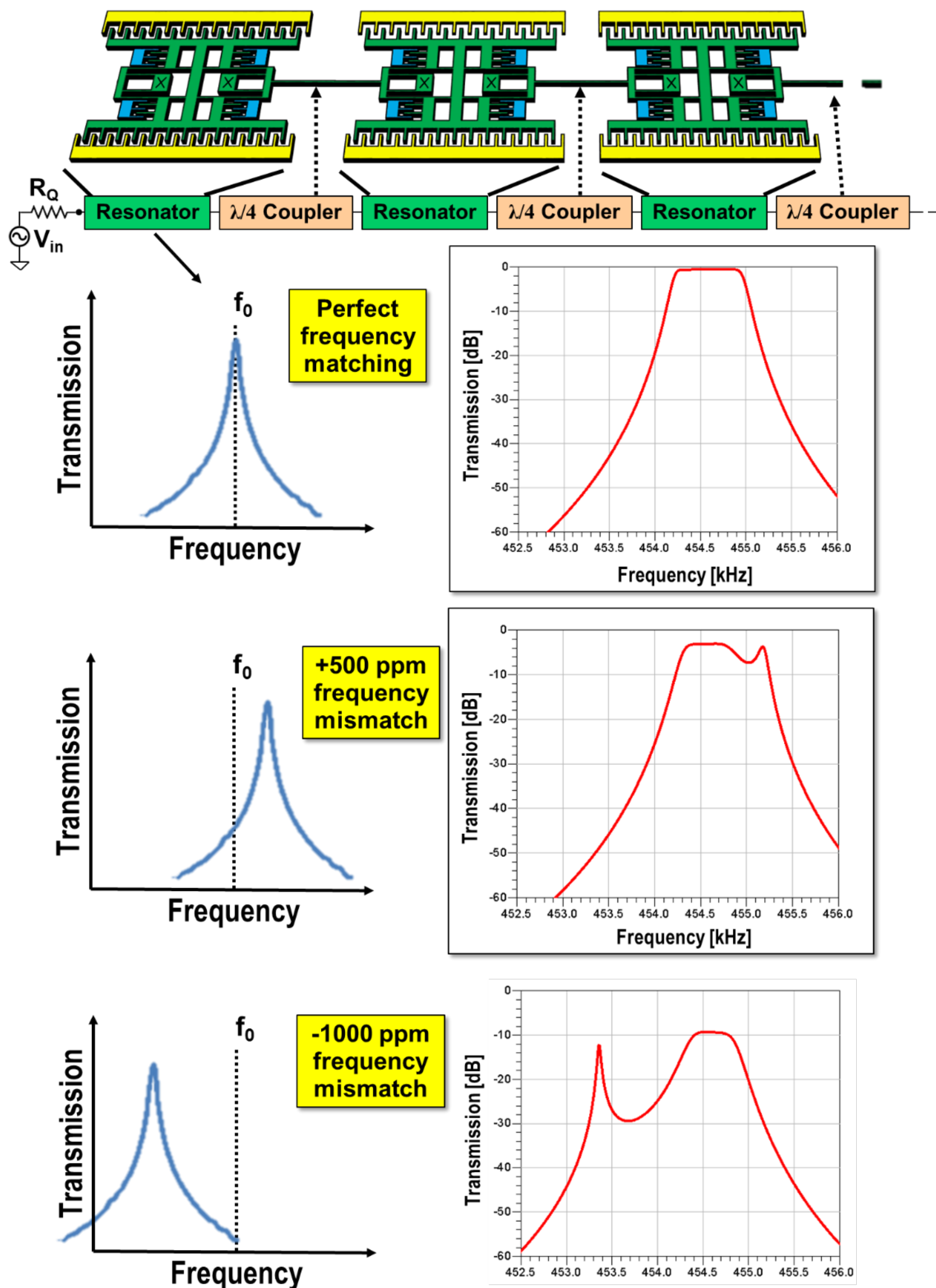

Figure 4.13: Simulated effects of passband distortion due to frequency variation of a single coupled resonator

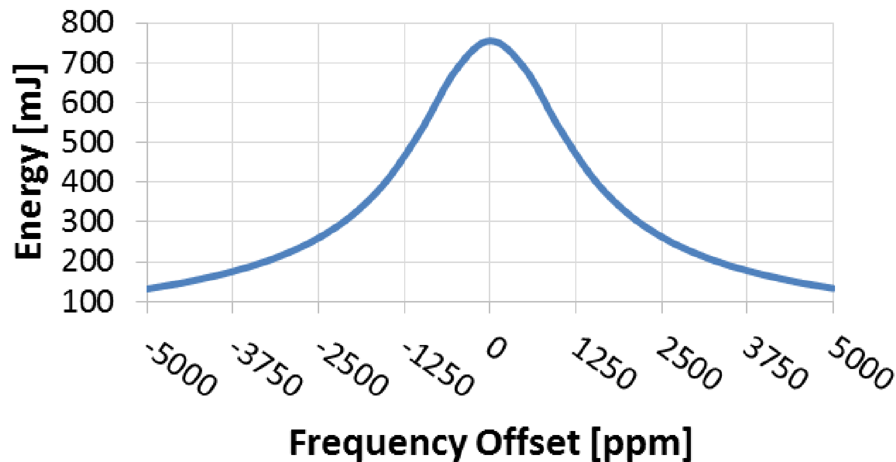

Figure 4.14: Simulated 4-resonator filter output energy plotted against the frequency offset of a single one of its constituent resonators, assuming all other resonators are spot on.

4.3.3 Simulated Passband Correction

Analytical verification of this energy maximization-based protocol is perhaps best done via brute force simulation. To this end, Figure 4.15 plots the integrated energy under a 400 Hz-bandwidth 455kHz 4-resonator bandpass filter characteristic over a 5-kHz window around the filter center frequency as tuning increments are applied. Here, at the start, each resonator in the filter takes on a random mass error deviating between 200-4000 ppm away from the designed value resulting in a severely distorted passband. As seen in Figure 4.15, tuning voltage steps applied individually to each resonator following the protocol of Section 4.3.1 generate a change in the energy in the 5-kHz band, and this energy increases as each resonator is tuned in sequence. After iterating the tuning protocol through each of the four resonators, the filter response spectrum transforms from a practically unusable response to that of a near-perfect 4th order Chebyshev filter. The completion of four tuning iterations required a mere 49 individual voltage steps, which could be applied in rapid succession with a digital control system yielding almost instantaneous passband correction.

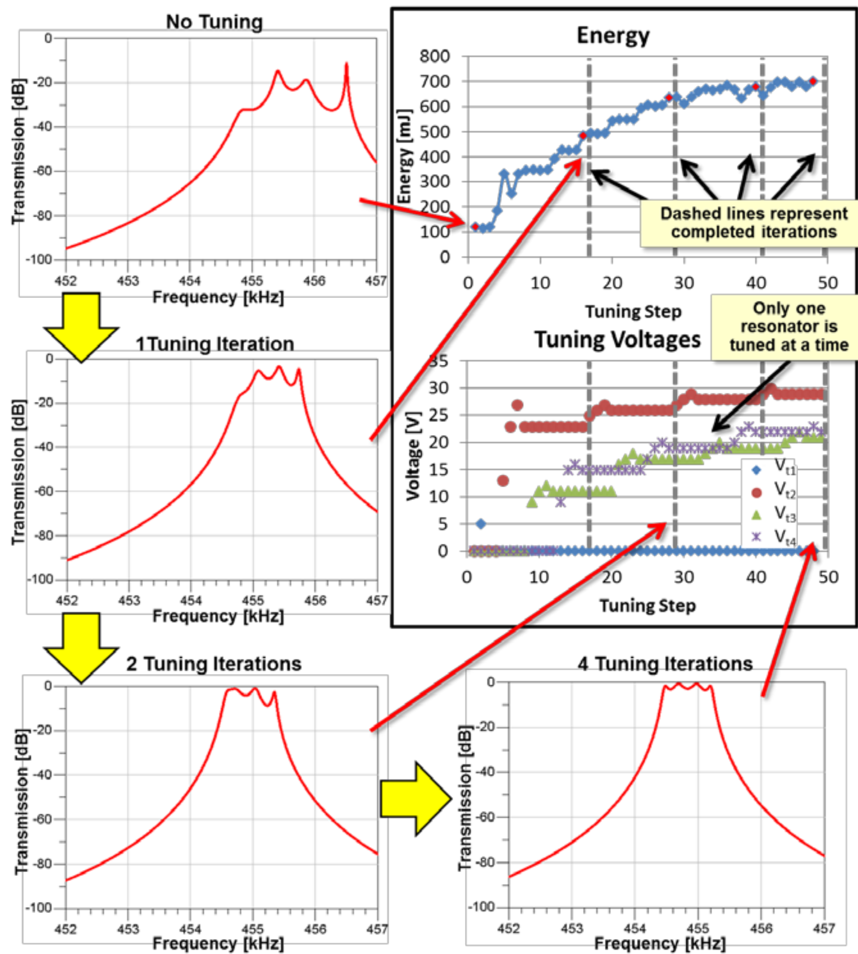

Figure 4.15: Simulation demonstrating the method and efficacy of the energy maximizing tuning protocol.

4.4 Experimental Confirmation

Pursuant to demonstrating the described passband tuning protocol, 4-resonator filters using the topology of Figure 4.1 were designed and fabricated using a three-mask polysilicon surface-micromachining process similar to that of [44]. Figure 4.16 presents the SEM of one such filter, this one centered at 523.5 kHz with a 532 Hz bandwidth, which is 0.1%.

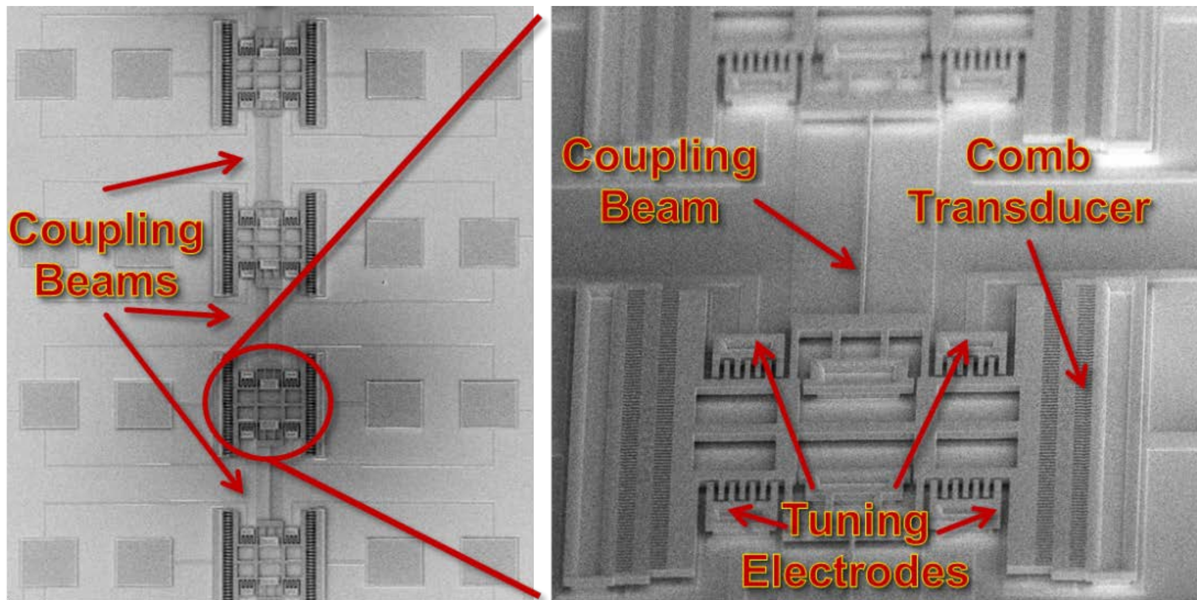

Figure 4.16: SEM images of a micromechanical filter comprised of 4 coupled resonators alongside an enlarged view of one of its constituent capacitive comb-transduced resonators.

Figure 4.17 presents a photo of the test apparatus used to evaluate the tuning protocol of Section 4.3.1, which included a custom-built glass vacuum chamber to provide a 10 μTorr environment during measurement while also facilitating electrical connection to outside instrumentation via bias and signal feedthroughs. Since the intent of measurement was to study the progression of the filter frequency response as tuning was applied according to the protocol, an Agilent 8751A network analyzer, rather than an energy-sensing diode circuit, was used to collect data.

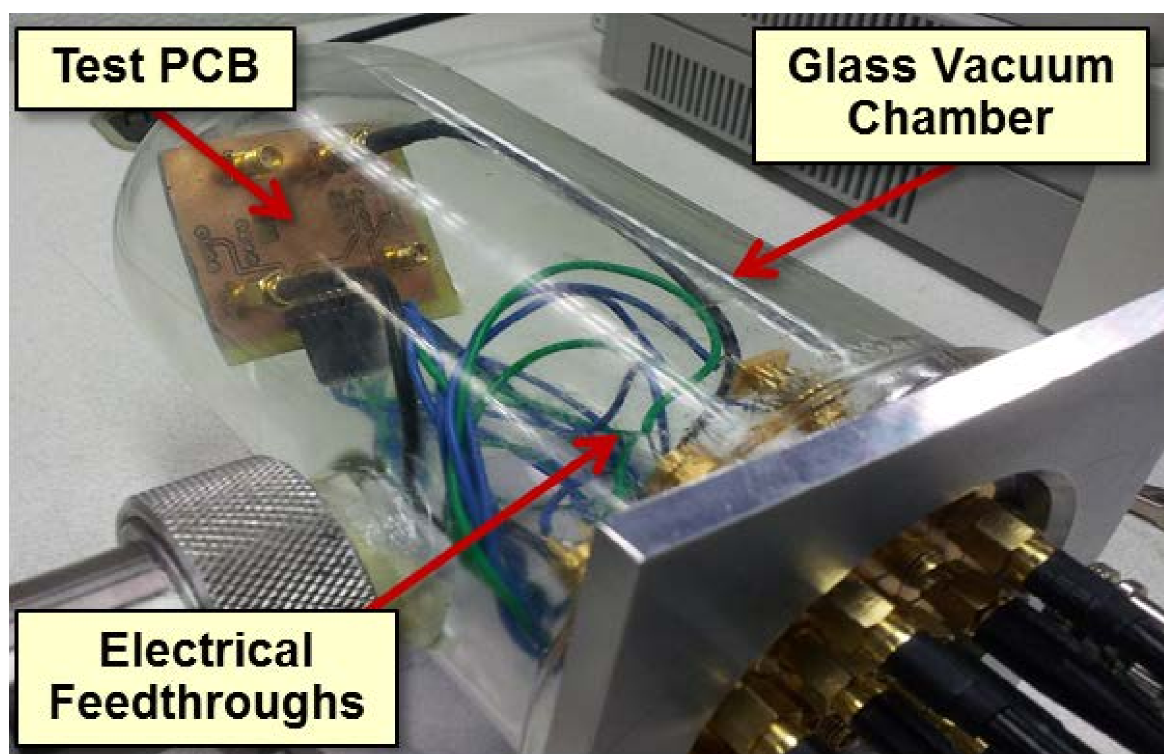

Figure 4.17: Custom-made glass vacuum chamber used to test the filter tuning protocol of this work

Figure 4.18 presents three filter response spectra measured while tuning a fabricated 4-resonator 523.5-kHz filter. The response in (a), taken before any tuning, is clearly distorted, looking nothing like the desired passband response. After tuning resonator 1 via the described protocol, the spectrum of (b) results, which now looks much more like a bandpass filter response, except with considerable passband distortion. Finally, (c) presents the filter response after tuning is finished (i.e., after all resonators are tuned to maximize the integrated output energy), showing the desired 0.1% bandwidth response with a 20-dB shape factor of just 1.59 (enabled by the use of four resonators) and an insertion loss of only 1.27dB, which is impressive for this small a percent bandwidth. Again, it is tuning, together with high constituent resonator *Q*'s on the order of 25,000 (*cf*. Figure 4.19), that makes possible this performance. Given that the filter response immediately after fabrication in Figure 4.18(a) is quite bad, tuning in fact appears instrumental to achieving reasonable performance with this small a percent bandwidth.

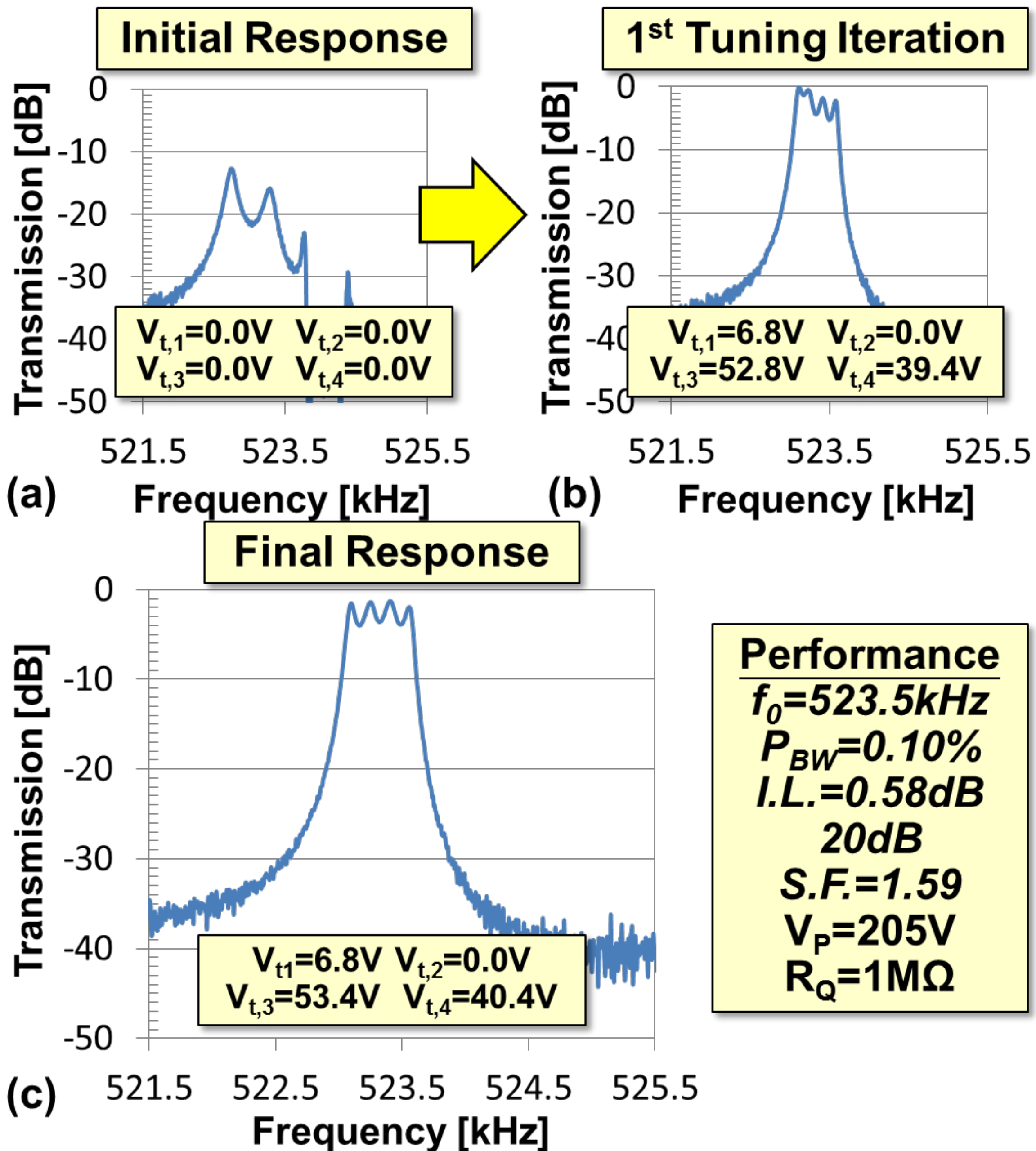

Figure 4.18: Measured 4-resonator filter characteristic with (a) no tuning applied, i.e., straight out of the fab, (b) tuning voltages governed by one procedural iteration (through one of the constituent resonators), and (c) the final tuned response after two iterations.

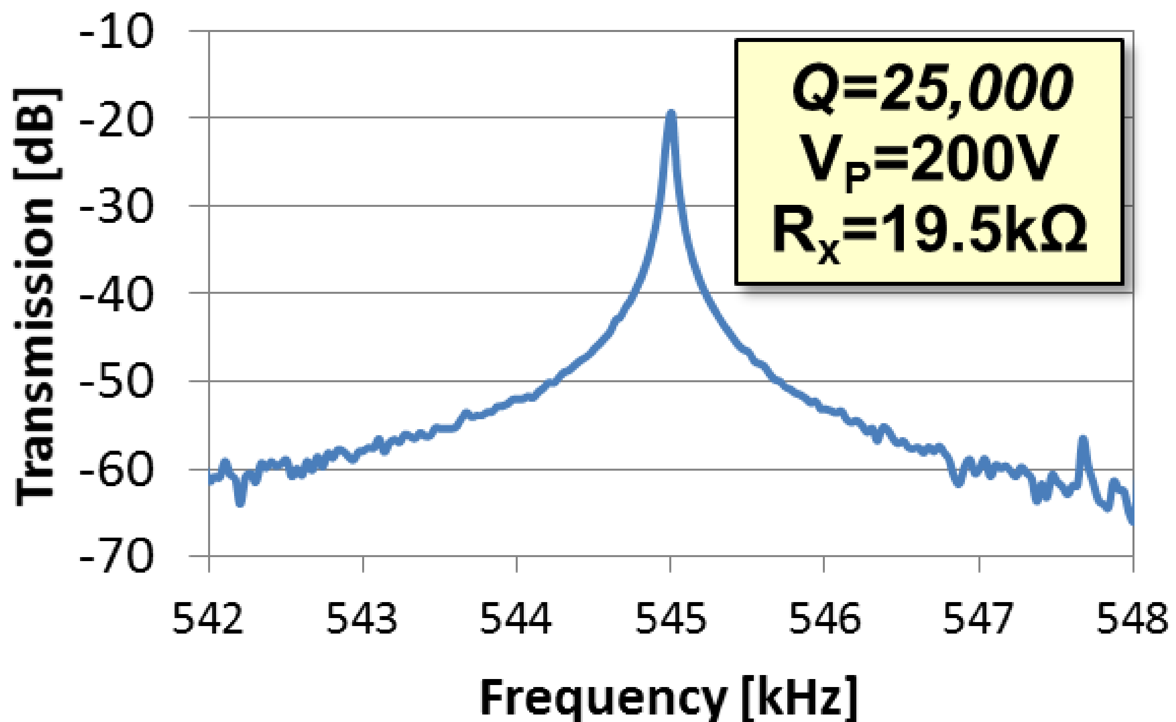

Figure 4.19: Measured transconductance spectra for a single capacitive comb-transduced resonator

It should be noted that the filter passband, although nice and uniform, exhibits about 3.4dB of ripple, which is 2.9dB more than the expected 0.5dB from design. This ripple is not a deficiency of the tuning protocol, but rather a consequence of insufficient electromechanical coupling, where the (C_x/C_o) of 6.3% for the measured filter is smaller than the 9.4% needed to attain a response with the designed ripple. The corrected passband in Figure 4.18(c) is in fact as it should be with this consideration.

4.5 Conclusions

The demonstration of tuned passband correction capable of attaining a near perfect frequency response for a 523.5-kHz 0.1%-bandwidth 4-resonator micromechanical filter with only 0.58 dB of insertion loss, a shape factor of 1.59, and passband ripple less than 3.5 dB, confirms the energy maximization-based tuning protocol described herein. It should be noted that the tuning procedure demonstrated here utilizes a purely mathematical optimization and can therefore be driven entirely by computer. Although this work demonstrated tuning via voltage-controlled electrical stiffness, any method for tuning or trimming is usable, including laser trimming [60] and localized anneal based methods [29]. The protocol is not limited to comb driven resonator based filters, but rather practically any filter using tunable or trimmable resonators, including high-frequency disk resonators, which are next on the bucket list.

5. CONCLUSION

Vibrating mechanical tank components, such as quartz crystals and SAW resonators, are leveraged as the frequency-setting elements in the majority of clock oscillators and narrowband RF filters today. These devices greatly outperform traditional LC tanks implemented using transistor technologies because they possess orders of magnitude higher Q values. Unfortunately, these crystals and SAW resonators are large, off-chip components that constitute a bottleneck in system miniaturization. While attempts have been made to shrink the physical dimensions of these devices to meet the ever-increasing demand for small form-factor electronic applications, these attempts have come at the expense of increased fabrication costs and worsened performance.

This dissertation serves to shed light on the potential benefits of harnessing MEMS resonators as the high-Q tank elements in critical timing and frequency filtering applications. A generalized frequency tunable capacitive-comb driven resonator topology was presented that realizes significant performance enhancements as device dimensions are diminished. This topology was then utilized to demonstrate two practical applications: (1) a tiny, ultra-low power 32.768-kHz real-time clock oscillator and (2) a 4th order 0.1% bandwidth coupled-resonator filter with an impressive shape factor and minimal insertion loss.

5.1 MEMS-Based Real-Time Clock Oscillator

First, a capacitive-comb transduced micromechanical resonator using aggressive lithography to occupy only 0.0154-mm^2 of die area was combined via bond-wiring with a custom ASIC sustaining amplifier and a supply voltage of only 1.65V to realize a 32.768-kHz real-time clock oscillator. The resonator occupied an area more than 100× smaller by area than miniaturized quartz crystal implementations and at least 4× smaller than other MEMS-based approaches, including those using piezoelectric material. The key to achieving such large reductions in size is the enormous rate at which scaling improves the performance of capacitive-comb transduced folded-beam micromechanical resonators, for which scaling of lateral dimensions by a factor S provides an S^2× reduction in both motional resistance and footprint for a given resonance frequency. This is a very strong dependency that raises eyebrows, since the size of the frequency-setting tank element may soon become the most important attribute governing cost in a potential MEMS-based or otherwise batch-fabricated 32.768-kHz timing oscillator market. In addition, unlike quartz counterparts, the size reduction demonstrated here actually reduces power consumption, allowing this oscillator to operate with only 2.1μW of DC power.

Because of their extensive scaling benefits, capacitive-transduced MEMS resonators seem well positioned to offer the smallest real-time clock oscillators provided that the repeatability issues associated with scaling can be mitigated. While the frequency tuning-

electrodes in this work provide an effective solution for alleviating center frequency variations exacerbated by aggressive scaling, there is some concern that the large tuning range can give rise to instability if the variables controlling the tuning are themselves not sufficiently stable. For this reason, design improvements that reduce device-to-device mismatch are always desirable and should be the subject of future work.

5.2 High Order Micromechanical Filters

Next, a systematic protocol for filter passband correction, together with voltage-controlled frequency tuning provided by capacitive-gap transducers, has made possible a 4-resonator micro-mechanical filter with a 0.1% bandwidth commensurate with the needs of channel-selection and an impressive 20-dB shape factor of 1.59. Indeed, a filter with this small a percent bandwidth would yield very poorly without this tuning mechanism and correction protocol, since typical finite fabrication mismatch tolerances on the order of 300 ppm do not permit an undistorted filter passband without post-fabrication tuning. Although demonstrated at a medium frequency (MF) of only 523.5 kHz, this filter passband correction protocol is directly applicable to higher frequency small percent bandwidth filters targeted for ultra-low power RF channel-selecting communication front-ends. An automated computer-controllable passband tuning protocol like that demonstrated here is among the more important ingredients needed to realize an RF channel-selecting filter bank. The demonstration of tuned passband correction capable of attaining a near perfect frequency response for a 523.5-kHz 0.1%-bandwidth 4-resonator micromechanical filter with only 0.58 dB of insertion loss, a shape factor of 1.59, and passband ripple less than 3.5 dB, confirms the energy maximization-based tuning protocol described herein.

It should be noted that the demonstrated tuning procedure utilizes a purely mathematical optimization and can therefore be driven entirely by computer. Although this work demonstrated tuning via voltage-controlled electrical stiffness, any method for tuning or trimming is usable, including laser trimming and localized anneal based methods. The protocol is not limited to comb-driven resonator based filters, but rather practically any filter using tunable or trimmable resonators, including high-frequency disk resonators. The application of this tuning protocol on higher frequency filters stands as an exciting avenue for future research exploration.

5.3 Future Research Directions

The devices demonstrated in this work appear to be well suited for assisting in the proliferation of low-power sensor nodes fit for the Internet of Things. However, before they can become practically applied, several technical concerns must first be addressed.

One such issue revolves around the effects of frequency instability incurred through environmental temperature changes. Certainly, oven-control could be employed to maintain a stable temperature and alleviate this concern. Unfortunately, this solution comes at the expense of significant power consumption. Utilizing the voltage controlled tuning electrodes highlighted throughout this work to compensate for temperature changes appears to be a logical

solution, however before this solution can be applied, extensive temperature related characterization must be performed, and an effective method for outfitting devices with integrated temperature sensors and feedback circuitry must be researched.

Another concern that must be addressed stems from the difficulty in implementing a suitable device package. The resonant structures of this work must be operated in sub-mTorr vacuum environments in order to achieve high Q values. Presently the packages capable of maintaining this level of pressure are significantly more expensive than traditional IC packages. In addition, package-induced stresses have been known to result in unpredictable resonance frequency shifts. Research aimed at developing a stress-free vacuum package holds significant importance.

5.4 Concluding Remarks

In conclusion, this dissertation explored methods by which voltage-controlled frequency tuning of capacitively-transduced micromechanical resonators made possible 1) an ultra-compact, low-power 32.768-kHz micromechanical clock oscillator; and 2) a high-order, small percent bandwidth coupled-resonator filter with minimal passband distortion. With future research and development, these devices show much promise for one day enabling the proliferation of low power, inexpensive, wireless sensor nodes.

REFERENCES

[1] J. Bryzek, “Emergence of a $ Trillion MEMS Sensor Market,” in *SensorCon*, 2012, pp. 1–22.
[2] R. A. Lawes, “Manufacturing costs for microsystems/MEMS using high aspect ratio microfabrication techniques,” *Microsyst. Technol.*, vol. 13, no. 1, pp. 85–95, Oct. 2006.
[3] J. Bouchaud, “Apple dictates the ranking of top 10 MEMS manufacturers in 2014,” *IHS Technology*, 2015. [Online]. Available: https://technology.ihs.com/527700/apple-dictates-the-ranking-of-top-10-mems-manufacturers-in-2014. [Accessed: 01-Jan-2015].
[4] D. James, D. Yang, and P. Gamache, “Inside the iPhone 6s,” *Chipworks*, 2015. [Online]. Available: http://www.chipworks.com/about-chipworks/overview/blog/inside-the-iphone-6s. [Accessed: 01-Jan-2015].
[5] “Did you know that the Nokia 1100 is the world’s best-selling handset?,” *PhoneArena*, 2015. [Online]. Available: http://www.phonearena.com/news/Did-you-know-that-the-Nokia-1100-is-the-worlds-best-selling-handset_id74364. [Accessed: 01-Jan-2015].
[6] L. Coetzee and J. Eksteen, “The Internet of Things – Promise for the Future ? An Introduction,” *IST-Africa Conf. Proc.*, pp. 1–9, 2011.
[7] D. Miorandi, S. Sicari, F. De Pellegrini, and I. Chlamtac, “Internet of things: Vision, applications and research challenges,” *Ad Hoc Networks*, vol. 10, no. 7, pp. 1497–1516, Sep. 2012.
[8] C. Nguyen, “MEMS technology for timing and frequency control,” *IEEE Trans. Ultrason. Ferroelectr. Freq. Control*, vol. 54, no. 2, pp. 251–270, 2007.
[9] W. C.-K. Tang, “Electrostatic Comb Drive for Resonant Sensor and Actuator Applications,” 1990.
[10] C. T.-C. Nguyen, “Micromechanical Signal Processors,” *PhD Thesis, Electr. Eng. Comput. Sci. Univ. California, Berkeley*, 1994.
[11] C. T.-C. Nguyen, “Micromechanical resonators for oscillators and filters,” in *1995 IEEE Ultrasonics Symposium. Proceedings. An International Symposium*, 1995, vol. 1, pp. 489–499.
[12] K. Wang and C. T. C. Nguyen, “High-order medium frequency micromechanical electronic filters,” *J. Microelectromechanical Syst.*, vol. 8, no. 4, pp. 534–557, 1999.
[13] D. E. Serrano, R. Tabrizian, and F. Ayazi, “Tunable piezoelectric MEMS resonators for real-time clock,” *Freq. Control Eur. Freq. Time Forum (FCS), 2011 Jt. Conf. IEEE Int.*, pp. 1–4, 2011.
[14] S. L. S. Lee and C. T.-C. Nguyen, “Mechanically-coupled micromechanical resonator arrays for improved phase noise,” *Proc. 2004 IEEE Int. Freq. Control Symp. Expo. 2004.*, vol. 00, no. c, pp. 280–286, 2004.
[15] G. Piazza, P. J. Stephanou, and A. P. Al Pisano, “Piezoelectric Aluminum Nitride Vibrating Contour Mode MEMS Resonators,” *J. micorelectromechanical Syst.*, vol. 15, no. 6, pp. 1406–1418, 2006.
[16] Jing Wang, J. E. Butler, T. Feygelson, and C. T.-C. Nguyen, “1.51-GHz nanocrystalline diamond micromechanical disk resonator with material-mismatched isolating support,” in *17th IEEE International Conference on Micro Electro Mechanical Systems. Maastricht MEMS 2004 Technical Digest*, 2004, pp. 641–644.
[17] G. Piazza, P. J. Stephanou, J. P. Black, R. M. White, and A. P. Pisano, “Single-chip multiple-frequency RF microresonators based on aluminum nitride contour-mode and

FBAR technologies," *2005 IEEE Ultrason. Symp. Sept. 18, 2005 - Sept. 21, 2005*, vol. 2, no. c, pp. 1187–1190, 2005.

[18] "Tuning Fork Crystal Units (Cylinder Type) - CFS2016," *Citizen Micro*, 2015. [Online]. Available: http://cfm.citizen.co.jp/english/product/pdf/CFS-CFV.pdf. [Accessed: 01-Jan-2015].

[19] "Tuning Fork Crystal Unit (SMD Ceramic Package) - CM315," *Citizen Micro*, 2015. [Online]. Available: http://cfm.citizen.co.jp/english/product/pdf/CM315.pdf. [Accessed: 01-Jan-2015].

[20] "32.768kHz SMD Low Profile Crystal," *Abracon LLC*, 2015. [Online]. Available: http://www.abracon.com/Resonators/ABS05.pdf. [Accessed: 01-Jan-2015].

[21] J. H. Staudte, "Subminiature Quartz Tuning Fork Resonator," in *27th Annual Symposium on Frequency Control*, 1973, pp. 50–54.

[22] "DSC11xx Performance PureSilicon Oscillators," *Micrel*, 2014. [Online]. Available: http://www.micrel.com/_PDF/Prod_Brief/DSC11xx_PB.pdf. [Accessed: 01-Jan-2015].

[23] "SiT1532 Smallest Footprint (1.2mm2) CSP," *SiTime Corporation*, 2014. [Online]. Available: http://www.sitime.com/products/datasheets/sit1532/SiT1532-datasheet.pdf. [Accessed: 01-Jan-2015].

[24] S. Kanbayashi, S. Okano, K. Hirama, and T. Kudama, "Analysis of Tuning Fork Crystal Units and Application Into Electronic Wrist Watches," in *30th Annual Symposium on Frequency Control*, 1976, vol. 2, no. 1, pp. 167–174.

[25] R. A. Johnson, *Mechanical Filters in Electronics*. New York: John Wiley and Sons, Inc., 1983.

[26] M. A. Abdelmoneum, M. M. Demirci, Y.-W. L. Y.-W. Lin, and C. T.-C. Nguyen, "Location-dependent frequency tuning of vibrating micromechanical resonators via laser trimming," *Proc. 2004 IEEE Int. Freq. Control Symp. Expo. 2004.*, vol. 00, no. c, pp. 272–279, 2004.

[27] W.-T. Hsu and A. R. Brown, "Frequency Trimming for MEMS Resonator Oscillators," *2007 IEEE Int. Freq. Control Symp.*, vol. 1–4, pp. 1088–1091, 2007.

[28] X. Huang, J. MacDonald, and W. T. Hsu, "Method and Apparatus for Frequency Tuning of a Micro-Mechanical Resonator." Google Patents, 2007.

[29] Kun Wang, Ark-Chew Wong, Wan-Thai Hsu, and C. T.-C. Nguyen, "Frequency trimming and Q-factor enhancement of micromechanical resonators via localized filament annealing," in *Proceedings of International Solid State Sensors and Actuators Conference (Transducers '97)*, 1997, vol. 1, pp. 109–112.

[30] H. C. Nathanson, W. E. Newell, R. A. Wickstrom, and J. R. Davis, "The resonant gate transistor," *IEEE Trans. Electron Devices*, vol. 14, no. 3, pp. 117–133, Mar. 1967.

[31] S. S. Li, Y. W. Lin, Z. Ren, and C. T. C. Nguyen, "An MSI micromechanical differential disk-array filter," *TRANSDUCERS EUROSENSORS '07 - 4th Int. Conf. Solid-State Sensors, Actuators Microsystems*, pp. 307–311, 2007.

[32] H. G. Barrow and C. T.-C. Nguyen, "A protocol for automated passband correction of high-order microelectromechanical filters," in *2014 IEEE International Frequency Control Symposium (FCS)*, 2014, pp. 1–5.

[33] Y. Lin, W. C. Li, B. Kim, Y. W. Lin, Z. Ren, and C. T. C. Nguyen, "Enhancement of micromechanical resonator manufacturing precision via mechanically-coupled arraying," *2009 IEEE Int. Freq. Control Symp. Jt. with 22nd Eur. Freq. Time Forum*, vol. 1, no. c, pp. 58–63, 2009.

[34] H. Yang, C. Wang, P. Zheng, and W. Wang, "On-Chip High- Q Inductor Using Wafer-Level Chip-Scale Package Technology," pp. 3–6.

[35] M. Wojnowski, V. Issakov, G. Knoblinger, K. Pressel, G. Sommer, and R. Weigel, "High-Q inductors embedded in the fan-out area of an eWLB," *IEEE Trans.*

Components, Packag. Manuf. Technol., vol. 2, no. 8, pp. 1280–1292, 2012.
[36] T. Owaki and T. Morita, “Excellent frequency stability and high-Q and small SH-type quartz SAW resonators,” in *IEEE Ultrasonics Symposium, 2005.*, 2005, vol. 4, no. c, pp. 1888–1891.
[37] L.-W. Hung and C. T.-C. Nguyen, “Capacitive-piezoelectric AlN resonators with Q,” *2011 IEEE 24th Int. Conf. Micro Electro Mech. Syst.*, pp. 173–176, 2011.
[38] L. Wu, M. Akgul, Z. Ren, Y. Lin, W.-C. Li, and C. T.-C. Nguyen, “Hollow stems for higher micromechanical disk resonator quality factor,” in *2011 IEEE International Ultrasonics Symposium*, 2011, pp. 1964–1967.
[39] A. I. Zverev, *Handbook of Filter Synthesis*. New York: John Wiley and Sons, Inc., 1967.
[40] S. D. Senturia, *Microsystem Design*. New York: Springer, 2004.
[41] W.-C. Li, Y. Jiang, R. A. Schneider, H. G. Barrow, L. Lin, and C. T.-C. Nguyen, “Polysilicon-filled carbon nanotube grass structural material for micromechanical resonators,” in *2011 IEEE 24th International Conference on Micro Electro Mechanical Systems*, 2011, pp. 477–480.
[42] M. Akgul, R. Schneider, Z. Ren, G. Chandler, V. Yeh, and C. T.-C. Nguyen, “Hot filament CVD conductive microcrystalline diamond for high Q, high acoustic velocity micromechanical resonators,” in *2011 Joint Conference of the IEEE International Frequency Control and the European Frequency and Time Forum (FCS) Proceedings*, 2011, pp. 1–6.
[43] W. C. Tang, T.-C. H. Nguyen, M. W. Judy, and R. T. Howe, “Electrostatic-comb drive of lateral polysilicon resonators,” *Sensors Actuators A Phys.*, vol. 21, no. 1–3, pp. 328–331, 1990.
[44] H. G. Barrow, T. L. Naing, R. A. Schneider, T. O. Rocheleau, V. Yeh, Z. Ren, and C. T.-C. Nguyen, “A real-time 32.768-kHz clock oscillator using a 0.0154-mm2 micromechanical resonator frequency-setting element,” in *2012 IEEE International Frequency Control Symposium Proceedings*, 2012, pp. 1–6.
[45] H. A. C. Tilmans, “Equivalent circuit representation of electromechanical transducers: I. Lumped-parameter systems,” *J. Micromechanics Microengineering*, vol. 6, no. 1, pp. 157–176, Mar. 1996.
[46] C. T.-C. Nguyen and R. T. Howe, “CMOS micromechanical resonator oscillator,” in *Proceedings of IEEE International Electron Devices Meeting*, 1993, pp. 199–202.
[47] K. Wang, “Microelectromechanical Resonators and Filters for Cummunications Applications,” The University of Michigan, 1999.
[48] “ASML DUV Stepper Model 5500/300.” [Online]. Available: https://nanolab.berkeley.edu/labmanual/chap4/4.19asml300.pdf.
[49] W. C. Tang, T.-C. H. Nguyen, and R. T. Howe, “Laterally driven polysilicon resonant microstructures,” *IEEE Micro Electro Mech. Syst. , Proceedings, 'An Investig. Micro Struct. Sensors, Actuators, Mach. Robot.*, vol. 20, pp. 25–32, 1989.
[50] C. T. C. Nguyen and R. T. Howe, “Integrated CMOS micromechanical resonator high-Q oscillator,” *IEEE J. Solid-State Circuits*, vol. 34, no. 4, pp. 440–455, 1999.
[51] D. Z. Pan, L. Liebmann, B. Yu, X. Xu, and Y. Lin, “Pushing multiple patterning in sub-10nm,” in *Proceedings of the 52nd Annual Design Automation Conference on - DAC '15*, 2015, pp. 1–6.
[52] “Statek CX9VSM Crystal,” *Statek Corporation*, 2015. [Online]. Available: http://www.statek.com/products/pdf/CX9 10157 Rev D.pdf. [Accessed: 01-Jan-2015].
[53] C.-J. Kim, J. Y. Kim, and B. Sridharan, “Comparative evaluation of drying techniques for surface micromachining,” *Sensors Actuators A Phys.*, vol. 64, no. 1, pp. 17–26, Jan. 1998.
[54] Y. W. Lin, S. Lee, S. S. Li, Y. Xie, Z. Ren, and C. T. C. Nguyen, “Series-resonant VHF

micromechanical resonator reference oscillators," *IEEE J. Solid-State Circuits*, vol. 39, no. 12, pp. 2477–2491, 2004.

[55] T. L. Naing, T. O. Rocheleau, Z. Ren, E. Alon, and C. T. C. Nguyen, "Vibration-insensitive 61-MHz micromechanical disk reference oscillator," *2012 IEEE Int. Freq. Control Symp. IFCS 2012, Proc.*, pp. 271–276, 2012.

[56] B. Razavi, *Design of Analog CMOS Integrated Circuits*. Boston: McGraw-Hill Education, 2000.

[57] "32.768kHz Ceramic SMD LVCMOS Crystal Oscillator," *Abracon LLC*, 2015. [Online]. Available: http://www.abracon.com/Oscillators/ASAK.pdf. [Accessed: 01-Jan-2015].

[58] K. R. Cioffi and W. Hsu, "32KHz MEMS-Based Oscillator for Low-Power Applications," pp. 551–558, 2005.

[59] S. Haykin, *Communication Systems*, 4th ed. Hoboken: John Wiley and Sons, Inc., 2001.

[60] M. A. Abdelmoneum, M. M. Demirci, S.-S. L. S.-S. Li, and C. T. C. Nguyen, "Post-fabrication laser trimming of micromechanical filters," *IEDM Tech. Dig. IEEE Int. Electron Devices Meet. 2004.*, pp. 39–42, 2004.

[61] "SG-3030CM Crystal Oscillator," *Seiko Epson Corporation*. [Online]. Available: https://support.epson.biz/td/api/doc_check.php?dl=brief_SG-3030CM&lang=en. [Accessed: 01-Jan-2015].

[62] S. Zaliasl, J. C. Salvia, G. C. Hill, L. W. Chen, K. Joo, R. Palwai, N. Arumugam, M. Phadke, S. Mukherjee, H. Lee, C. Grosjean, P. M. Hagelin, S. Pamarti, T. S. Fiez, K. A. A. Makinwa, A. Partridge, and V. Menon, "A 3 ppm 1.5x0.8mm 1.0uA 32.768kHz MEMS-Based Oscillator," *IEEE J. Solid-State Circuits*, vol. 50, no. 1, pp. 291–302, 2015.